

DISSERTATION

Homogeneity of melt-grown bulk superconductors

ausgeführt zum Zwecke der Erlangung des akademischen Grades eines Doktors der
Technischen Wissenschaften

betreut von

Univ. Prof. Dr. Dr. h. c. H. W. Weber
Atominstitut der Österreichischen Universitäten (E141)
Technische Universität Wien

eingereicht an der Technischen Universität Wien
Fakultät für Physik

von

Dipl. Ing. Silvia Haindl
Matrikelnummer: 9525790
Hofmannsthalgasse 10/5/3
1030 Wien



Wien, 17. Jänner 2005

KURZFASSUNG

In der vorliegenden Arbeit wird die Homogenität von schmelztexturierten Hochtemperatursupraleitern untersucht. Mittelpunkt in experimenteller Hinsicht bilden Messungen der remanenten Feldverteilung mittels Hallsonden und der neu entwickelte Magnetoscan. Hierbei wird die Probenoberfläche mit einem kleinen Permanentmagnet abgerastert, wobei die Antwort der Probe simultan mit einer Hallsonde schon während des Rasterns aufgenommen wird. Der Begriff „Homogenität“ bezieht sich nun in erster Linie auf die Ergebnisse der beiden experimentellen Methoden, die remanente Feldverteilung und die Stärke der Abschirmströme in einer Oberflächenschicht des Supraleiters. Mit den Ergebnissen direkt im Zusammenhang stehen die positionsabhängigen supraleitenden Parameter, insbesondere die kritische Stromdichte. Ein Unterschied zwischen den Wachstumssektoren tritt klar hervor, und Inhomogenitäten wie z.B. Korngrenzen und Risse im supraleitenden Massivmaterial werden mit Hilfe des vorgestellten experimentellen Zugangs abgebildet. Dies liefert gerade den Herstellern wertvolle Information über die Qualität der Supraleiter. Der Vorteil der experimentellen Methoden liegt auf der Hand, da es sich hierbei in erster Linie um zerstörungsfreie Techniken handelt. Nicht zerstörungsfrei sind beispielsweise eine vertikale Analyse, in welcher die Probenoberfläche sukzessive abgeschliffen wird, oder magnetische Messungen an kleinen Referenzproben, die an unterschiedlichen Positionen des Massivsupraleiters entnommen wurden. In Kombination mit dem Magnetoscan und den Messungen der remanenten Feldverteilung erhält man ein dreidimensionales Ergebnis.

TABLE OF CONTENTS

Acknowledgments	iii
Introduction	1
Motivation and Material Processing	
Experimental approach to the homogeneity of bulk superconductors	
Neutron irradiation	
Position dependence of superconducting parameters	
Growth induced inhomogeneities	
Vertical assessment of a bulk monolith	
Novel processing methods	
1 Processing: Melt-processed YBCO	9
1.1 Top-seeded-melt-growth (TSMG) process	9
1.1.1 Peritectic solidification	
1.1.2 Seeding method	
1.1.3 Growth Morphology	
1.2 Additives	13
1.2.1 Refinement of the Y-211 phase	
1.2.2 Platinum additions	
1.2.3 Cerium additions	
1.3 Doping of $\text{YBa}_2\text{Cu}_3\text{O}_{7-\delta}$	16
1.3.1 The effect of lithium doping	
2 Microstructure	19
2.1 Phases in melt-grown samples	20
2.2 Grain boundaries and cracks in melt-grown samples	30
2.3 Grain boundaries in MSMG samples	33
3 Samples	40
3.1 Samples from IFW Dresden	41
3.1.1 Bulk samples	
3.1.2 Reference samples	
3.2 Samples from IPHT Jena	44
3.3 Samples from NEXANS	46
3.4 Sample from ZfW Göttingen	48

3.5 Samples from IRC Cambridge	50
3.5.1 Multi-seeded-melt-grown samples	
3.6 Samples from ICMAB Barcelona	53
4 Experimental Methods	54
4.1 Hall probe measurements	54
4.1.1 Principles	
4.1.2 Experimental arrangement	
4.1.3 Experimental parameters for trapped field measurements	
4.1.4 Bean model and radial assessment of bulk superconductors	
4.2 Magnetoscan	59
4.2.1 Principles	
4.2.2 Magnetoscan Setup	
4.2.3 Experimental parameters for the magnetoscan	
4.2.4 More tests of the new technique	
4.3 VSM measurements	65
4.4 Microstructural investigation:	66
XRD of powders, scanning Electron Microscopy, optical Microscopy	
5 Neutron Irradiation	67
5.1 Calculation of the activity	67
5.2 Neutron irradiation of $\text{YBa}_2\text{Cu}_3\text{O}_{7-\delta}$ bulk samples	68
5.3 Neutron irradiation of Li-doped $\text{YBa}_2\text{Cu}_3\text{O}_{7-\delta}$	68
5.4 Neutron irradiated samples of this work	69
6 Discussion	70
6.1 Radial homogeneity of TSMG bulk superconductors	70
6.1.1 Mapping of the growth sectors	
6.1.2 Mapping of subgrain free regions	
6.1.3 Flux penetration into $\text{YBa}_2\text{Cu}_3\text{O}_{7-\delta}$ bulk superconductors <i>Np-6</i> and <i>Np-11</i>	
6.1.4 Flux penetration into Li-doped $\text{YBa}_2\text{Cu}_3\text{O}_{7-\delta}$ bulk superconductors	
6.2 Vertical homogeneity of TSMG bulk superconductors	88
6.3 Results of neutron irradiation	94
6.3.1 Neutron irradiation of $\text{YBa}_2\text{Cu}_3\text{O}_{7-\delta}$ bulk: <i>Np-11</i>	
6.4 Results on MSMG superconductors	98
6.4.1 Grain Boundaries in <i>MS-1</i> , <i>MS-2</i> , <i>MS-3</i> and <i>MS-4</i>	
6.4.2 Characterization of <i>R1</i>	
7 Outlook	104
Summary	107
References	108
List of Publications	113
Curriculum Vitae	116

ACKNOWLEDGMENTS

I would like to thank the following persons (in alphabetical order):

Max BICHLER, *ATI/TU Vienna*
Brigitta BUCHBERGER, *secretary at ATI/TU Vienna*
David CARDWELL, *IRC Cambridge*
Eva CECH-HABERL, *secretary at ATI/TU Vienna*
Friederike CERNY, *secretary at ATI/TU Vienna*
Barbara FERTL, *technical assistant at ATI/TU Vienna*
Raquel GONZÁLEZ ARRABAL, *now at Universidad Autónoma de Madrid*
Xavier GRANADOS, *ICMAB Barcelona*
Helmut HAINDL, *chaos researcher, Vienna*
Maria Luise HAINDL, *hotel manageress, Vienna*
Sibylla HAINDL, *family member, Vienna*
Herbert HARTMANN, *technical assistant at ATI/TU Vienna*
Norbert HÖRHAGER, *student at ATI/TU Vienna*
Alicia P. KELLEHER, *secretary at IRC Cambridge*
Ernst KLAPFER, *reactor ATI/TU Vienna*
Gernot KRABBES, *IFW Dresden*
Doris LITZKENDORF, *IPHT Jena*
Martin MÜLLER, *TU Vienna*
Regina MÜLLER, *student at ATI/TU Vienna*
Hari Babu NADENDLA, *IRC Cambridge*
Maria PAUKOVITS, *secretary at ATI/TU Vienna*
Georg PÜHRINGER, *ATI/TU Vienna*
Hans SCHACHNER, *reactor ATI/TU Vienna*
Larissa SHLYK, *IFW Dresden*
Hua Y. SHY, *IRC Cambridge*
Udo STARZACHER, *TU Vienna*
Christoph VOUSINAS, *student at ATI/TU Vienna*
Heribert WALTER, *NEXANS Superconductors GmbH*
Harald W. WEBER, *ATI/TU Vienna*
Gilbert WILDOM, *ATI/TU Vienna*
Tomasz WOJCIK, *student at ATI/TU Vienna*

INTRODUCTION

Motivation and Material Processing

Since more than ten years, bulk superconductors of the $\text{YBa}_2\text{Cu}_3\text{O}_{7-\delta}$ (Y-123) compound have been investigated and developed for the fabrication of large scale applications, where they serve as permanent magnets, motor components or flywheel energy storage systems, for which high trapped fields are required. For a high temperature superconductor in its remnant state, and assuming that the critical current density J_C flows unimpeded and field-independent throughout the whole volume of a cylindrical bulk sample with radius R and thickness h , the magnetic induction at the center of its top surface is given by

$$B_0 = \frac{\mu_0 H^*}{2} \frac{h}{R} \ln \frac{R + \sqrt{R^2 + h^2}}{h} \quad (1)$$

with $H^* = J_C \cdot R$. With $J_C(B) = \text{const.}$, we have adopted Bean's model of the critical state [1, 2]. For comparison, the magnetic induction of a homogeneous cylindrical permanent magnet with a remanent induction B_r is (also in the center on the surface of the magnet)

$$B_0 = \frac{B_r}{2} \frac{h}{\sqrt{R^2 + h^2}} \quad (2)$$

Scaling $B_r = \mu_0 H^* = 2$ and introducing the thickness-to-diameter ratio as a dimensionless variable $x = h/R$, the advantage of high temperature superconductors is obvious, as illustrated in Fig. 1. The thickness-to-diameter ratio of the samples investigated in this work is around $x = 0.82 \pm 0.18$.

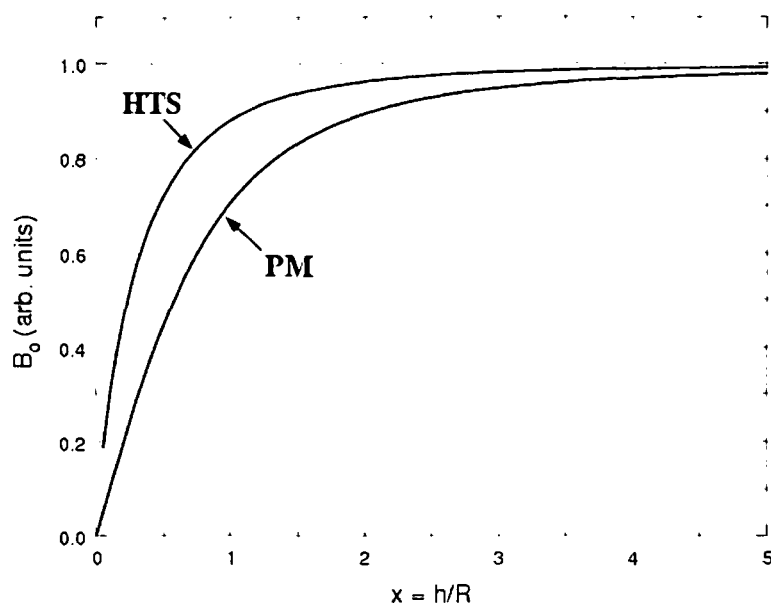


Fig. 1: Comparison of the magnetic inductions in the center between a permanent magnet (PM) and a high temperature bulk superconductor (HTS).

Large trapped fields at temperatures of $T = 77$ K and below were reported in the last years [3, 4, 5, 6]. In high temperature superconducting bulk material the trapped field is determined by the magnitude of the critical current density J_C and the volume, where the currents are circulating. Therefore, to avoid possible limitations of the current, a high degree of homogeneity is required in bulk materials. In this work the term “homogeneity” is used primarily with respect to the critical current flow, the penetration of the magnetic flux into the sample and the shielding current behavior.

Melt processing techniques involving the seeding method turned out to be a standard fabrication process for large single grain monoliths [7, 8]. In sintered samples, which consist of randomly oriented grains, the critical current density is limited by *i*) grain boundaries (inter-grain current) and *ii*) by the small size of the grains (intra-grain current). Applying melt processing techniques, so called “monodomain” samples of large diameters (normally 2-5 cm) and well oriented grains (i.e. without large angle grain boundaries) can be grown, and therefore large critical currents are obtained.

Initially, research focused mainly on the control of the process conditions of bulk superconductors, i. e. the development of the seeding technique, excess yttrium by Y_2O_3 or Y_2BaCuO_5 addition, refinement of the Y_2BaCuO_5 -phase (Y-211) by adding small amounts of CeO_2 or Pt, etc. A short survey of the processing of top-seeded-melt-grown (TSMG) bulk superconductors can be found in *Chapter 1*. There, also the effect of doping is discussed, especially the case of Li-doping. Over the years, fabrication processes were quite successful with optimizing the bulk materials with respect to their homogeneity and mechanical stability,

cf. the one concerning the homogeneity of the high temperature superconducting material and its relation to the microstructure. Topics such as crack formation in bulk materials, the distribution of the Y-211 inclusions, etc. were often investigated.

The microstructure of bulk monoliths and microstructural inhomogeneities (defects) are summarized in *Chapter 2*. The main attention is paid *i)* to the different phases which are present in the melt grown superconductors and *ii)* to grain boundaries. It should be mentioned that the presence of the Y-211 phase plays also a role in the crack formation within the Y-123 matrix. Optical and scanning electron micrographs of the investigated samples are shown. Finally microstructural features of multi-seeded-melt-grown (MSMG) superconductors are discussed.

In *Chapter 3* all sample relevant data is collected. For sample *H186*, manufactured at ZfW Göttingen, the exact processing parameters were not available. This sample, an ordinary top-seeded-melt-grown $\text{YBa}_2\text{Cu}_3\text{O}_{7.8}$ bulk, was principally used for the first demonstration of the magnetoscan. In order to clarify the process parameters and the possible compositions, publications of the ZfW-group are quoted. The same holds for the Ag-joined $\text{YBa}_2\text{Cu}_3\text{O}_{7.8}$ materials, which were used as test samples for the magnetoscan technique.

Experimental approach to the homogeneity of bulk superconductors

The spatial homogeneity of bulk superconductors is often deduced from measurements of the flux density distribution, i.e. the trapped field profiles. Hall scans in the saturated state of the monolith provide initial information on the "quality" of the sample [9]. Severe inhomogeneities which hinder the current flow inside the bulk, like cracks, can easily be detected by conventional mapping of the trapped field (see Fig 2). However, smaller or even growth induced inhomogeneities can hardly be observed in the trapped field profile in the fully activated state, when the superconductor exhibits a saturated magnetic flux distribution. It is known that the achievement of saturation depends on the activation mode (see Fig. 3). Based on Bean's model, a minimum field of $2H^*$ is required to obtain saturation for an activation in the zero field cooled mode (zfc), whereas in the field cooled mode (fc) a minimum field of only H^* is needed. Under pulsed field activation higher fields than $2H^*$ may be required to obtain saturation. Anyway, the magnetization under pulsed fields is much more complex due to dynamical considerations which involve heat generation inside the sample and will not be discussed in this work. It will be shown, however, that measurements of the trapped field after an activation in fields below $2H^*$ in zfc mode show many details of the

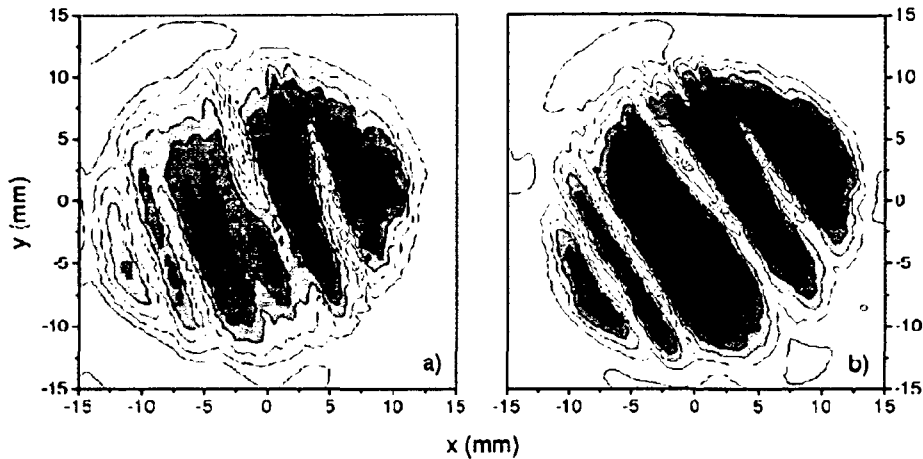


Fig. 2: Severe inhomogeneities in a bulk superconductor detected by Hall scans of the trapped field. Contour plots of a) the top side and b) after having removed 1.4 mm from the top side of the sample [9].

flux penetration into the superconductor, are, and therefore, suitable to detect spatial inhomogeneities in the bulk monolith. According to Bean's model of the critical state, the stepwise flux penetration into the sample allows a more detailed investigation of the homogeneity of the bulk in radial direction.

A completely new technique, called magnetoscan, consists of scanning the sample surface with a small permanent magnet and detecting simultaneously the response of the superconductor by a Hall probe. The principles and results were first published by Eisterer et al. in 2003 [10]. Up to now the technique was reproduced by Zeisberger et al [11] and by Kono [12]. With this technique, local shielding currents in the surface of the sample are mapped with a high spatial resolution. The experimental methods used in this work are introduced in *Chapter 4*.

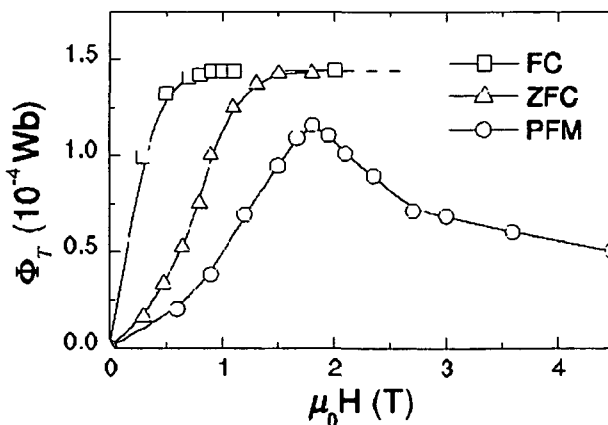


Fig. 3: Dependence of the trapped flux inside the superconducting sample and the applied magnetic field ($H = H^*$) for various activation modes: field cooled (FC), zero field cooled (ZFC) and pulsed field magnetization (PFM). Fig. taken from Ref. [21].

A brief summary of the experimental methods and results was presented at the International Symposium on Superconductivity 2004 [13].

Neutron Irradiation

The radiation induced enhancement of the trapped field was investigated for one $\text{YBa}_2\text{Cu}_3\text{O}_{7.8}$ bulk sample. Pinning can be improved by the introduction of defects into the material. One way to create pinning centers is neutron irradiation of the superconductor. The defects due to radiation are so-called defect cascades, which are homogeneously distributed in the material and are responsible for the enhancement of the trapped field. The diameter of these cascades, including their strain field, is a few nanometers, which matches the size of the coherence length in high temperature superconductors. The average defect density was found to be linearly dependent on the fast neutron fluence. Fig 4. shows these defects. However, the transmission electron microscope (TEM) images were taken from a $\text{Bi}_2\text{Sr}_2\text{CaCu}_2\text{O}_8$ single crystal after irradiation to a fast neutron fluence of $8 \cdot 10^{21} \text{ m}^{-2}$. This does not matter, since the radiation induced defects in $\text{YBa}_2\text{Cu}_3\text{O}_{7.8}$ are very similar. *Chapter 5* contains relevant information on neutron irradiation of $\text{YBa}_2\text{Cu}_3\text{O}_{7.8}$ bulk superconductors. The results are given in *Chapter 6*. The superconducting samples containing lithium could not yet be measured. During neutron irradiation, tritium was produced which diffuses out of the sample. The usual experimental investigation of the irradiated samples would have to take place outside an extractor hood which is not acceptable for safety reasons [14].

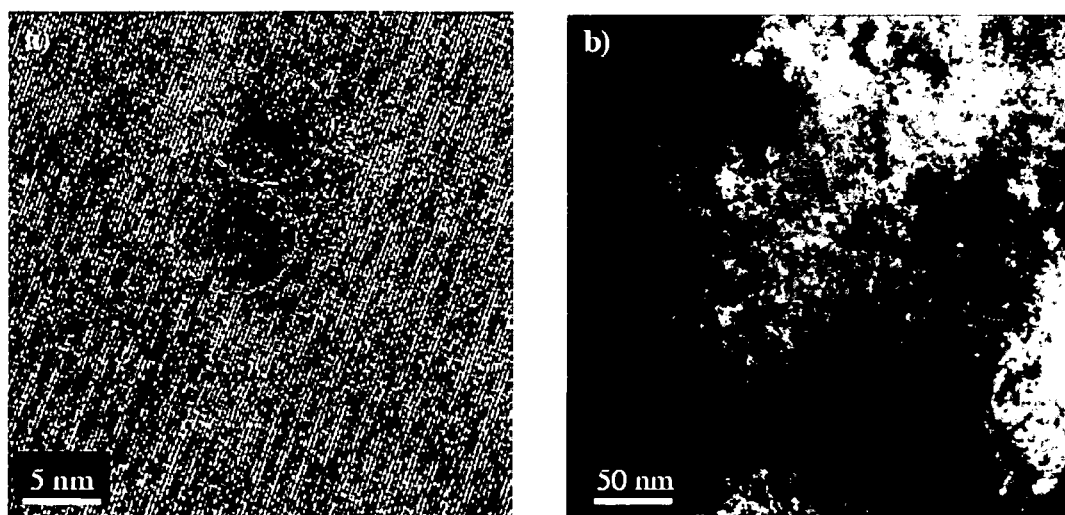


Fig. 4: a) High resolution image of neutron induced defect cascades identified by the dark contrast (inside the circles). b) Radiation induced collision cascades. Black dots indicate the strain fields of the defects. The TEM images are taken from [15].

Position dependence of superconducting parameters

The usual methods to determine experimentally the position dependence of the superconducting parameters inside a bulk monolith involve destructive procedures, e.g. cutting the bulk sample into small specimens or into slices (“reference samples”). Subsequently, the small reference samples are analyzed individually to find correlations between the superconducting parameters and the microstructure. This approach is often reported in the literature.

Dewhurst et al. [16] investigated experimentally the variation of the superconducting properties in a Sm-123 seeded $\text{YBa}_2\text{Cu}_3\text{O}_{7-\delta}$ bulk monolith. To do so, the sample was cut into 27 small cubic specimens (top = T, middle = M, bottom = B), as shown schematically in Fig. 5a. The measurements of the magnetic moment and of the transition temperature were carried out in a vibrating sample magnetometer (VSM) and an ac-susceptometer, respectively. The data were presented in a contour plot (Fig. 5b and 5c). A strong suppression of the transition temperature T_C was found in the vicinity of the seed. This result is explained by the Sm-contamination of the Y-123 matrix in this region, since T_C strongly depends on compositional variations. Focussing on the J_C variation, a region of reduced J_C was found in the vicinity of the seed and increased J_C 's were found symmetrically away from the seed. The increase in J_C is explained by an observed increase of Y-211 volume density. An interesting result is also the high J_C inside the a -growth sectors at the edges of the sample (compare specimens T1 or M9 in Fig 5c).

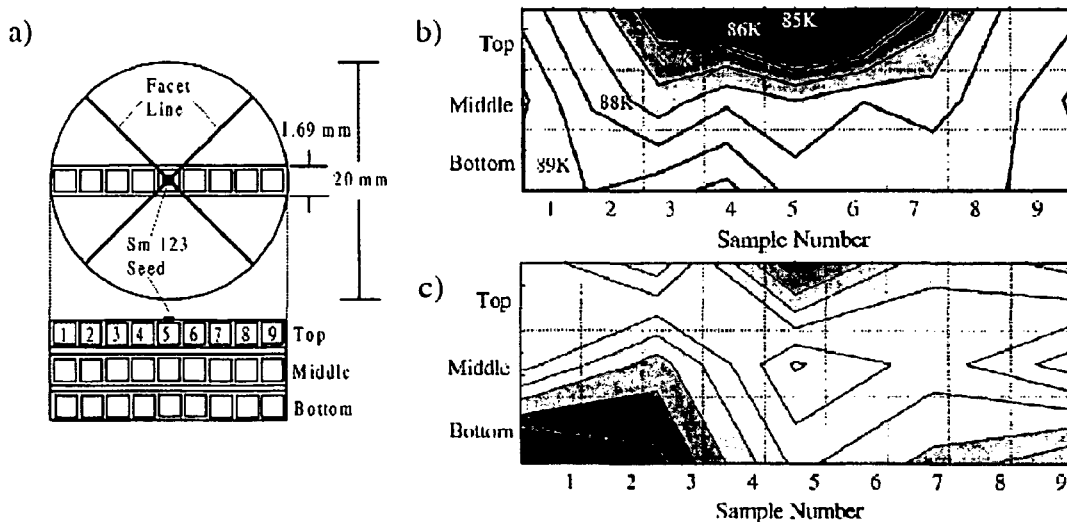


Fig. 5: a) Schematic diagram of the 27 cubic samples cut from the bulk. b) Variation of T_C and c) Variation of J_C at $T = 65$ K (lighter shades indicate higher J_C values). [16]

Similar investigations were performed by other groups [17, 18, 19, 20]. In comparison with these results and in order to correlate them with the results of the magnetoscan, measurements on small specimens cut from a Li-doped $\text{YBa}_2\text{Cu}_3\text{O}_{7.8}$ monolith were investigated by our own VSM. The results are also discussed in *Chapter 6*.

Growth induced inhomogeneities

A main part of this work is dedicated to a comparison between the growth induced microstructure and the superconducting properties. The measurement of the trapped field distribution as a non-destructive method was used to locate inhomogeneities in the bulk material. A growth related structure of the trapped field profile was found at IPHT Jena, however by pulsed field activation [21, 22]. With increasing activation field, the maxima of the trapped field pattern move towards the a - a -growth sector boundaries (a - a -GSBs), as can be seen in Fig. 6a. A $\text{YBa}_2\text{Cu}_3\text{O}_{7.8}$ bulk sample ($\varnothing = 30$ mm, $h = 20$ mm) was activated at a field of 3 T (pulsed field) at a temperature of 77 K. This shows that the GSBs are nearly free of weak links. Fig 6b shows a polarized optical micrograph of the a - a -GSB. In this case, the sample was cut perpendicular to the a - a -GSB plane. A subgrain free zone of approximately 1 mm thickness around the a - a -GSB can be seen under polarized light, i. e. the weak links in high temperature bulk superconductors are mainly related to subgrainboundaries in these materials. This result was confirmed in our work by trapped field measurements (in zfc mode) upon increasing the activation fields, as well as by magnetoscans. A detailed discussion together with an analysis of the microstructure can be found in *Chapter 6*.



Fig. 6: a) Trapped field profile at $T = 77$ K activated under 3 T in a pulsed field mode. b) Polarized optical micrograph of a - a -GSB with subgrain free zone. The figures are taken from [21].

Vertical assessment of a bulk monolith

A generally new idea is a characterization of the homogeneity of a bulk monolith in vertical direction. This is achieved by grinding the sample layer by layer followed by experimental methods, such as Hall scans of the trapped field, magnetoscans and microstructural analysis. Although this method is destructive – the sample thickness is reduced with each grinding step – characteristics of growth related features along the *c*-axis (growth sectors (GSs) of the monolith, cracks, grains and subgrains) can be mapped either by Hall scans or by the magnetoscan. In the scope of this work, results of three different samples are presented in *Chapter 6*. Investigations on multi-seeded-melt-grown (MSMG) superconductors complete the results on grain boundaries.

Novel processing methods

An addition of specific metallic oxides to the precursor composition leads to the new and interesting “cyclic grown superconductors”. They consist of a periodic structure of a Y-211 free matrix and thin bands containing the metal oxide phase. They are described in *Chapter 7*, where a brief outlook, especially a challenge of the magnetoscan technique is presented.

1. PROCESSING:

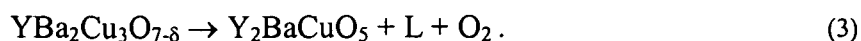
MELT-PROCESSED YBCO

1.1 Top-seeded-melt-growth (TSMG) process

The requirement of large superconducting grains, so called “single domains” or “mono-domains”, was already pointed out in the *Introduction*. Well aligned, large grains, which form the $\text{YBa}_2\text{Cu}_3\text{O}_{7.8}$ matrix (Y-123), can be obtained by the top-seeded-melt-grown process. This melt-processing technique *i)* is based on the peritectic solidification reaction and *ii)* uses a seed crystal. The product of this technique is a monolithic sample, which contains Y_2BaCuO_5 (Y-211) and other phases inside an $\text{YBa}_2\text{Cu}_3\text{O}_{7.8}$ matrix.

1.1.1 Peritectic solidification

The fundamental process for the melt processing techniques is the peritectic reaction (here written as a decomposition) occurring at the peritectic temperature $T_p = 1020\text{ }^\circ\text{C}$ (for 0.21 bar oxygen partial pressure):



Y_2BaCuO_5 occurs as a solid phase, and the liquidus L contains Ba, Cu and O. $\text{YBa}_2\text{Cu}_3\text{O}_{7.8}$ is formed again during cooling, i.e. when the temperature is lowered below T_p . Usually, the system is cooled down to $30\text{ }^\circ\text{C}$ below T_p , which creates an undercooling effect increasing the growth rate. Early experiments showed that the liquid is not only oxygen deficient, but

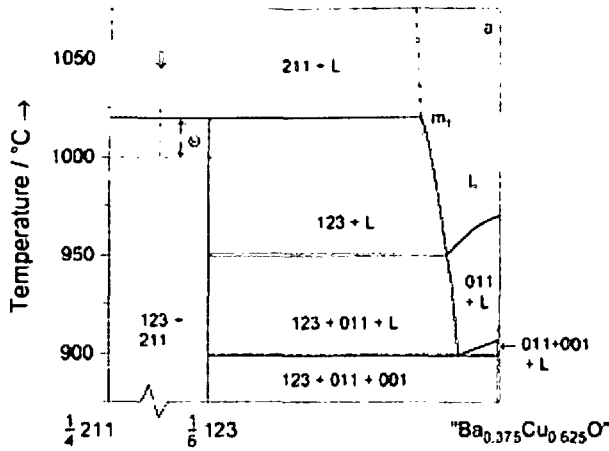


Fig. 7: Polythermal section of $(1/4)Y_2BaCuO_5 - (1/6)YBa_2Cu_3O_{7.8} - "Ba_{0.375}Cu_{0.625}O"$ at $p(O_2) = 0.21$ bar [23].

also yttrium deficient. Therefore, an additional Y_2BaCuO_5 admixture in the starting powder supports the yttrium balance during melt growth. As a quaternary compound, $YBa_2Cu_3O_{7.8}$ has a very complex phase diagram, which is better accessible via polythermal sections. A polythermal section used for an "Y-123 + Y-211" precursor is shown in Fig. 7.

In the so called modified melt crystallization process (MMCP), Y_2O_3 instead of Y_2BaCuO_5 is used as an admixture to the starting powder [23]. The appropriate polythermal section is shown in Fig. 8. The advantage of this process is a decreased processing temperature and a larger temperature range ("process window").

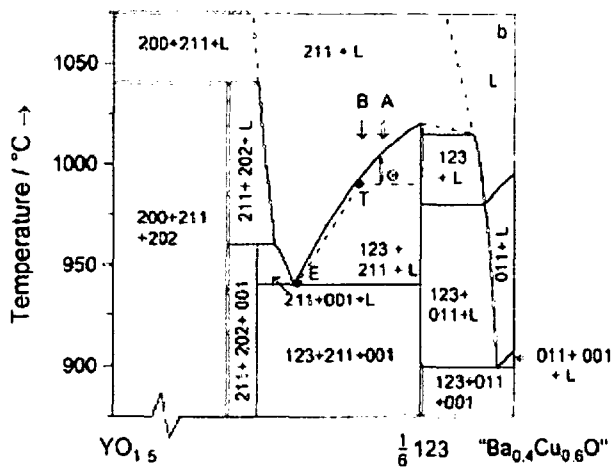


Fig. 8: Polythermal section of $(1/2)Y_2O_3 - (1/6)YBa_2Cu_3O_{7.8} - "Ba_{0.4}Cu_{0.6}O"$ at $p(O_2) = 0.21$ bar [23].

1.1.2 Seeding Method

The melt-growth process alone, however, did not lead to the desired result of large well aligned grains. The presence of many nucleation centers caused the formation of “natural” grain boundaries. Growth control could be obtained by employing a seed crystal. This process is called top-seeded-melt-growth. Due to the conditions of the melt process, the seed crystal requires similar lattice constants and a higher peritectic melting point than the growing phase. Usually, Sm-123, Nd-123 or MgO seed crystals are used. They have similar lattice parameters and do not melt during the heating cycle because of their higher melting points. In the cooling phase, the growth of the Y-123 follows the crystallographic orientation of the seed.

As a consequence of the seeding, a solid solution $(\text{Sm}_x\text{Y}_{1-x})\text{Ba}_2\text{Cu}_3\text{O}_{7-\delta}$ in the vicinity of the seed (“interdiffusion zone”) is formed, resulting in a local suppression of the critical temperature T_C . It is also possible, that the seed melts partially. The solidification with seeds is described by three steps [24]: *i*) Sympathetic nucleation on the five $\{001\}$ surfaces except the (001) surface on the top. The (Y-211 + L)-mixture is in contact with the bottom, (001), the surface and the (100)/(010) surfaces of the seed, and five growth sectors (domains) start to develop. Anyhow, the exact nucleation process is very complex and not yet investigated in detail. *ii*) Facet development followed by *iii*) continuous growth of the Y-123 phase. Fig 9 shows a schematic illustration of the seed induced growth control. Cooling of the system can be performed either by a thermal gradient or by an isothermally undercooled melt. Cooling with a thermal gradient generally inhibits secondary nucleation when the area below the seed is held at lower temperatures than the rest of the precursor. The growth from an isothermally undercooled melt yields more homogeneous superconductors, but of smaller size.

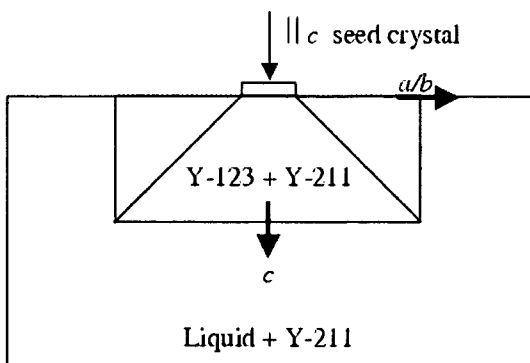


Fig. 9: Illustration of the top seeded melt growth process.

1.1.3 Growth Morphology

Assuming that the seed crystal on the top of the precursor is oriented with its crystallographic c -axis normal to the surface of the pressed pellet, the grown bulk monolith exhibits the usual five domains, according to the crystallographic orientation of the seed: one c -growth sector (c -GS), where the growth front proceeds in c -direction, and four a -growth sectors (a -GS), where the growth front proceeds in a - and b -direction. The boundaries between the growth sectors are denoted by a - a - or a - c growth sector boundaries (GSBs). Fig. 10 illustrates the GSs and the GSBs.

The situation becomes more difficult, when two or more seeds are used, because the different growth sectors generate more growth sector boundaries. This is the case in MSMG samples. Actually in two of the investigated MSMG samples, the crystallographic orientation of the seed was unconventional, because the c -axis was tilted to the normal of the surface of the precursor pellet.

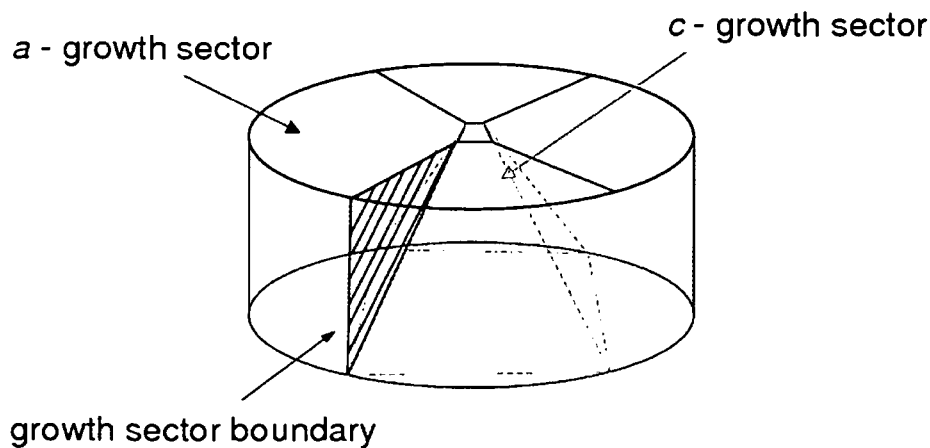


Fig.10: GSs and GSBs in a TSMG bulk.

1.2 Additives

1.2.1 Refinement of the Y-211 phase

Pinning centers in a superconductor are formed by introducing defects into the material. It is well known, that, in addition to the uniform distribution of these defects, the pinning capability is optimized when the defect size is comparable to the coherence length ξ in the superconducting material, which is a few nanometers for $\text{YBa}_2\text{Cu}_3\text{O}_{7-\delta}$. It is also widely accepted that the non-superconducting Y_2BaCuO_5 phase (Y-211), which is embedded in the Y-123 matrix, plays an important role in the pinning behavior of melt-grown superconductors. This is supported by the fact that the critical current density of the bulk sample can be correlated to the size of the Y-211 inclusions and their distribution, as is shown in Fig. 11. The quantity V_{211}/d_{211} can be interpreted as the effective surface area of the Y-211/Y-123 interface per unit volume. Based on the proportionality between J_C and V_{211}/d_{211} in Fig. 11, a fine dispersion of the Y-211 particles is needed inside the Y-123 matrix to enhance J_C . The size d_{211} and the volume fraction V_{211} of the Y-211 particles can be influenced in principle by the following processing conditions: heat treatment profile, excess yttrium and additives in the starting powder composition. Many kinds of additive were investigated in the literature, among them also SnO_2 , ZrO_2 , BaZrO_3 , but most commonly are Pt, PtO_2 and CeO_2 .

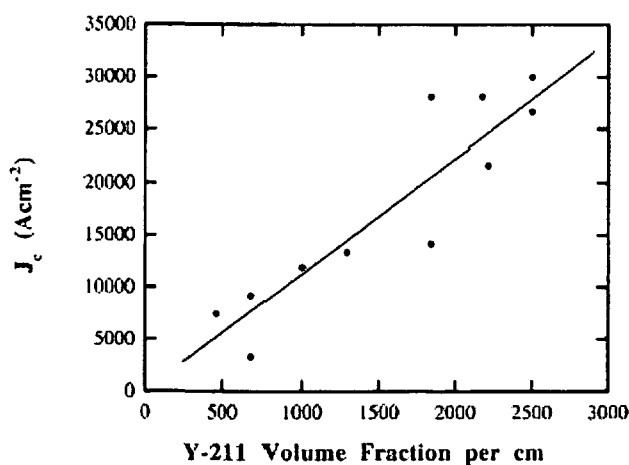


Fig. 11: Critical current density in melt-grown superconductors as a function of Y-211 particle size [25].

1.2.2 Platinum additions

Platinum additions (Pt, PtO₂) are effective in refining the size of the Y-211 inclusions. This was first suggested by Ogawa et al. [26, 27] and rapidly confirmed by other groups [28, 29, 30]. It was also confirmed in the last years, that Pt additions cause an enhancement of the critical current densities in melt grown YBa₂Cu₃O₇₋₈ bulks due to the smaller size of the Y-211 particles. Furthermore, Pt additions limit the coarsening of the Y-211 particles. One effect of the Pt addition is a modification of the interfacial energy between the Y-211 phase and the liquid. In a simple model [31], the size of the Y-211 particle (radius r) is estimated to be

$$r \propto (D_L \cdot \Gamma \cdot t)^{1/3}, \quad (4)$$

where D_L is the diffusivity of yttrium in the liquid, Γ is the Gibbs-Thomson coefficient and t is the holding time. The Pt addition, therefore, influences the product $D_L \cdot \Gamma$.

1.2.3 Cerium additions

Like other additives, CeO₂ additions were found to be of significant interest. A first detailed study of CeO₂ doping of YBa₂Cu₃O₇₋₈ showed an improvement of the critical current density [32]. Delamare et al. could identify the Ce-containing phase as BaCeO₃, which appeared in the Y-123 matrix with cubic shape and forming square grains with a size of 1-2 μm . More recently, (but not citing the work of Delamare et al.) the behavior of ZrO₂ additions was



Fig. 12: BaCeO₃ phase identified by TEM, taken from [35].

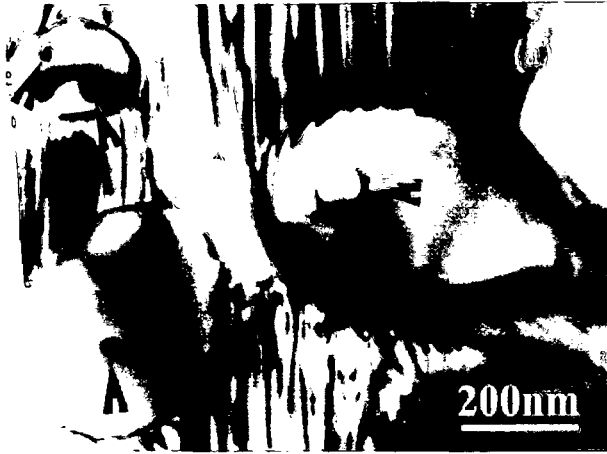


Fig. 13: TEM image of Y-211 particles with Y₂O₃ core (markers) inside [35].

analyzed. Nonuniformly distributed inclusions were found in the YBa₂Cu₃O_{7-δ} matrix. They were identified as BaZrO₃ phases. Moreover, the small inclusions of the BaCeO₃ phase tend to be more effective as pinning centers than the Y-211 inclusions [33].

The role of Ce additives on the refining mechanism of Y-211 was widely discussed. Like Pt, Ce is responsible for the change of the interfacial energy between the Y-211 particles and the liquid. Other mechanisms were proposed that are more likely for Ce than for Pt, e.g. a heterogeneous nucleation mechanism [34]. The Y-211 phase nucleates around nanometer sized Y₂O₃ particles, which are formed by the following reaction



Experimentally, small Y₂O₃ cores of nanometer size were found inside Y-211 particles by transmission electron microscopy. Fig. 12 and 13 show TEM images [35].

1.3 Doping of $\text{YBa}_2\text{Cu}_3\text{O}_{7-\delta}$

Doping denotes chemical substitution of elements in the unit cell and, therefore, modifications due to impurities. The aim of doping is *i)* to use the dopant as a probe for a better characterization of the superconducting mechanism in the cuprates in general, and *ii)* the improvement of the physical characteristics of the material in view of a technical merit. A survey of the various doping possibilities is given by Skakle [36]. In the scope of this work, Cu-substitutions in $\text{YBa}_2\text{Cu}_3\text{O}_{7-\delta}$ by metal ions are of interest. A series of publications showed that the critical temperature T_C decreases generally when Cu is substituted by a metal ion. Even a non-magnetic impurity strongly decreases T_C , and it turned out that non-magnetic ions, such as Zn^{2+} or Li^+ , result in a stronger suppression of superconductivity than magnetic ions such as Ni^{2+} [37]. On the other hand the introduced defects seem to be responsible for an enhancement of the critical current density J_C .

1.3.1 The effect of lithium doping

As shown in Fig. 14, two Cu-sites exist: Cu(1) is the site within the Cu-O chains, while Cu(2) is the site within the CuO_2 planes. Cu-substitutions occupy preferentially one of the two sites. In the case of Li-doping, the majority of the impurities is located at the Cu(2) sites. Neutron powder diffraction showed that in Li-doped $\text{YBa}_2\text{Cu}_3\text{O}_{7-\delta}$ samples synthesized in oxygen, the nonmagnetic Li^+ -ion substitutes for the magnetic Cu^{2+} -ion in the CuO_2 planes. If the samples are synthesized in air, a fraction of 20% of the Li impurities can also be found at Cu(1) sites [38].

The literature on Zn-doped $\text{YBa}_2\text{Cu}_3\text{O}_{7-\delta}$ turned out to be extremely useful for understanding the Li-doped systems, because Li^+ and Zn^{2+} , both non-magnetic but different in valence, affect the local magnetic structure of the CuO_2 planes in the same way. Bobroff et al. [39] found that the influence of Li and Zn on the magnetic properties as well as on T_C can be ascribed to magnetic correlations caused by a spinless perturbation.

In the last years the research group at IFW Dresden worked extensively on Zn- and Li-doped $\text{YBa}_2\text{Cu}_3\text{O}_{7-\delta}$. They found a linear decrease of T_C with increasing impurity concentration (Fig. 15). The reported rates of the decrease are -6 K/at.% for Li doping and -9 K/at.% for Zn-doping [40]. The impurity concentration is related to the chemical formula

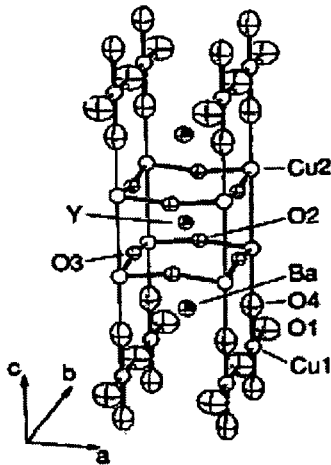


Fig. 14: Unit cell of $\text{YBa}_2\text{Cu}_3\text{O}_{7.8}$. Taken from [41].

$\text{YBa}_2(\text{Cu}_{1-x}\text{M}_x)_3\text{O}_{7.8}$ with M denoting the impurity metal (Li or Zn) and x the concentration in at.%. More clearly: For a dopant concentration of 0.5 at.% Li the composition formula is $\text{YBa}_2(\text{Cu}_{0.95}\text{Li}_{0.05})_3\text{O}_{7.8}$.

The optimum concentration levels with regard to the maximum trapped fields were deduced from measurements of the pinning force density at a temperature of 77 K. The critical current J_C was determined from VSM measurements in fields up to 8 T. They found that the pinning force density $F_P = J_C \cdot B$ exhibits a maximum for dopant concentrations of 0.5-0.6 at.% Li. Compared to the optimal Zn-doped $\text{YBa}_2\text{Cu}_3\text{O}_{7.8}$ system, the optimal Li-doped $\text{YBa}_2\text{Cu}_3\text{O}_{7.8}$ material showed two times higher pinning force densities, and the critical temperature T_C for the optimal Li concentration was reduced to around 90 K. With increasing Li-concentration, F_P decreases again. Assuming that Li-doping creates point defects, the decrease of F_P may be attributed to an overlap of the individual pinning potentials.

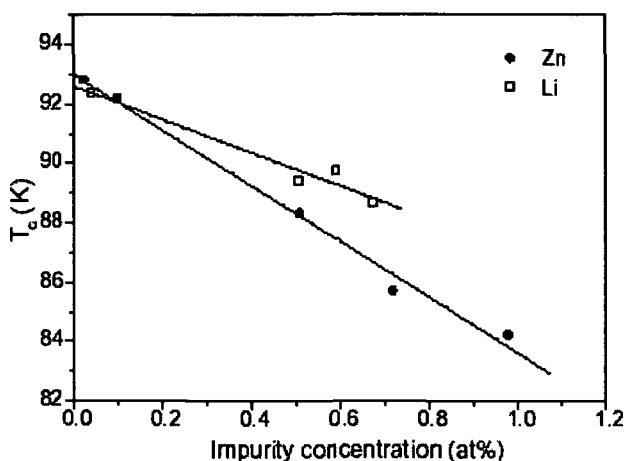


Fig. 15: The critical temperature as a function of impurity concentration for Zn and Li [40].

The effect of Li impurities on the upper critical field H_{C2} [37] shows a decrease to 112 T, compared to the undoped reference sample with $H_{C2} = 130$ T. The values of H_{C2} were determined according to Werthamer, Helfand and Hohenberg [42] from the formula

$$H_{C2}(0) = 0.7 \cdot T_C \cdot |\partial H_{C2} / \partial T| T_C. \quad (6)$$

The coherence lengths ξ_{ab} were obtained from the Ginzburg Landau relation

$$\mu_0 H_{C2} = \Phi_0 / 2\pi(\xi_{ab})^2. \quad (7)$$

The coherence lengths ξ_{ab} for the undoped reference sample and the Li-doped sample are 1.59 nm and 1.71 nm, respectively. Additional measurements [37] were carried out on post-annealed samples, but no difference to the as-grown samples was found.

2 MICROSTRUCTURE

Secondary phases and crystal defects associated with the growth process are always present in high temperature superconductors. They influence the homogeneity of the material and, therefore, the superconducting parameters. In this work, optical light microscopy, polarized light microscopy and scanning electron microscopy were used to investigate the microstructure of the samples. The resolution of an optical microscope is determined by Abbe's criterion. Structures down to 0.5 μm can be resolved. The resolution limit in a scanning electron microscope reaches the nm-range. Additionally, in a scanning electron microscope, the possibility of energy dispersive analysis with x-rays exists. The qualitative analysis of the chemical elements present in the bulk is, therefore, accessible. Both methods, optical and scanning electron microscopy can be used to complement each other for examining defects in melt-grown bulk superconductors. These are primarily grain boundaries (and the twin structure), secondary phases and cracks.

2.1 Phases in melt-grown samples

A lot of phases are present in the $\text{YBa}_2\text{Cu}_3\text{O}_{7.8}$ matrix, the most dominant is the Y_2BaCuO_5 phase. It is widely accepted, that the Y_2BaCuO_5 phase is responsible for pinning. Y_2BaCuO_5 has an orthorhombic crystal structure like $\text{YBa}_2\text{Cu}_3\text{O}_{7.8}$, but with different lattice parameters (see Table 1). While the $\text{YBa}_2\text{Cu}_3\text{O}_{7.8}$ matrix shows a preferred orientation in a TSMG bulk with only small perturbations, the orientation of Y_2BaCuO_5 is random [43].

A lot of progress on the Y_2BaCuO_5 phase (Y-211 particles) addresses its distribution, its refinement and its influence on the cracking behavior of the melt grown monolith [24, 44], cf. also a recent review article by R. Cloots et al. [45]. The segregation of the Y-211 particles is described by the so-called “pushing-trapping” model adopted by A. Endo to melt grown bulk $\text{YBa}_2\text{Cu}_3\text{O}_{7.8}$. A summary can be found in [31]. The model describes the behavior of spherical, inactive particles in front of a planar solid-liquid interface. Other assumptions are: an isothermal peritectic reaction, constant thermophysical properties and no interaction of Y-211 particles between each other. The melt, where the Y-211 particles are present, is mainly described by the viscosity η . The growth rate R of the solid is limited by the yttrium diffusion in the liquid, the Y-211 particle is, therefore, an active particle, contrary to the model assumption, because it supplies the system with yttrium. Fig 16a shows the two dominant forces acting on a Y-211 particle with radius r : *i*) F_d denotes a “drag force” due to viscous flow which is always conducive to trapping of the particle, *ii*) F_i denotes a force due to the interfacial energy $\Delta\sigma_0$, which is, in the case of $\Delta\sigma_0 > 0$, conducive to pushing the particle as shown in Fig 16a. In the case of $\Delta\sigma_0 < 0$, F_i is conducive to trapping. The interfacial energy consists of three contributing terms $\Delta\sigma_0 = \Delta\sigma_{sp} - \Delta\sigma_{lp} - \Delta\sigma_{sl}$, where the subscripts stand for solid (s), particle (p) and liquid (l). In the model the trapping probability for a Y-211 particle is now depending on the size (radius) of the

Table 1: Lattice parameters of the orthorhombic phases Y-123 and Y-211 [46].

	a	b	c	space group
$\text{YBa}_2\text{Cu}_3\text{O}_{6.9}$	0.3821 nm	0.3887 nm	1.1695 nm	<i>Pmmm</i>
Y_2BaCuO_5	1.2179 nm	0.5659 nm	0.7136 nm	<i>Pnma</i>

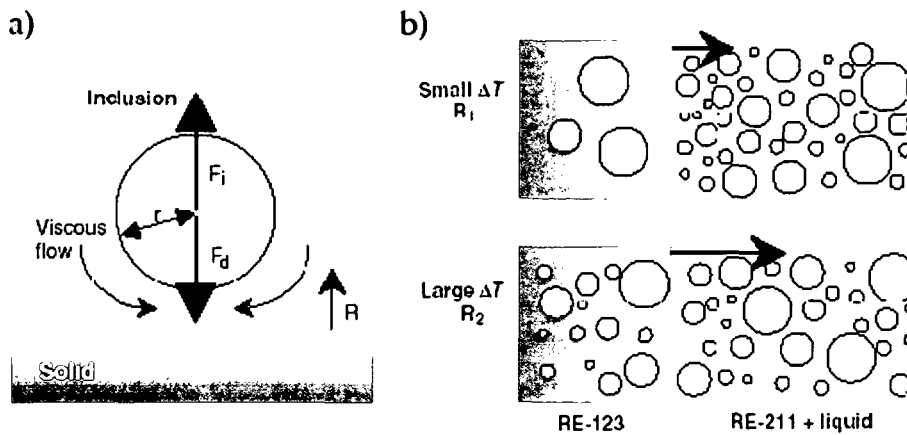


Fig. 16: Schematic presentation of the pushing-trapping model. Taken from [45].

particle itself. This suggests the existence of a “critical radius” r^* : At a given growth rate, only particles with $r > r^*$ are trapped, smaller particles are pushed. The basic equation relates the growth rate R to the critical radius r^* of the Y-211 particle:

$$R \propto \Delta\sigma_0 \cdot \eta^{-1} \cdot r^{*-1}.$$

This means, the higher the growth rate, the smaller the particles that can be trapped. From the standard classical nucleation model by Turnbull and Fisher [47], the growth rate R is proportional to the undercooling ΔT . As illustrated in Fig 16b, the growth rate increases, when the undercooling increases and, therefore, the critical radius of the trapped particles decreases. At the start of the solidification process at the seed, ΔT is low. Therefore, small Y-211 particles are pushed. With increasing distance from the seed, ΔT becomes larger and consequently more and smaller Y-211 particles are trapped. This can be observed in Fig 18, where a high concentration of small Y-211 particles appeared after having removed ~ 5 mm from the top surface of the sample, i.e. at increasing distance from the seed.

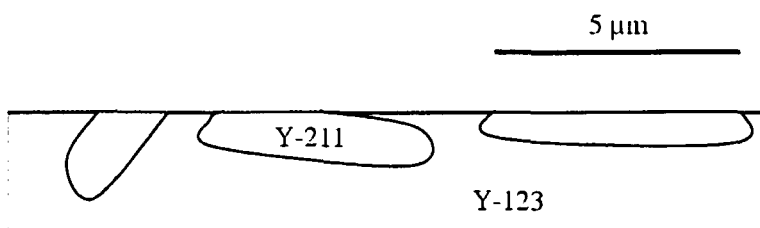


Fig. 17: Schematic illustration of the “size” of the Y-211 phase.

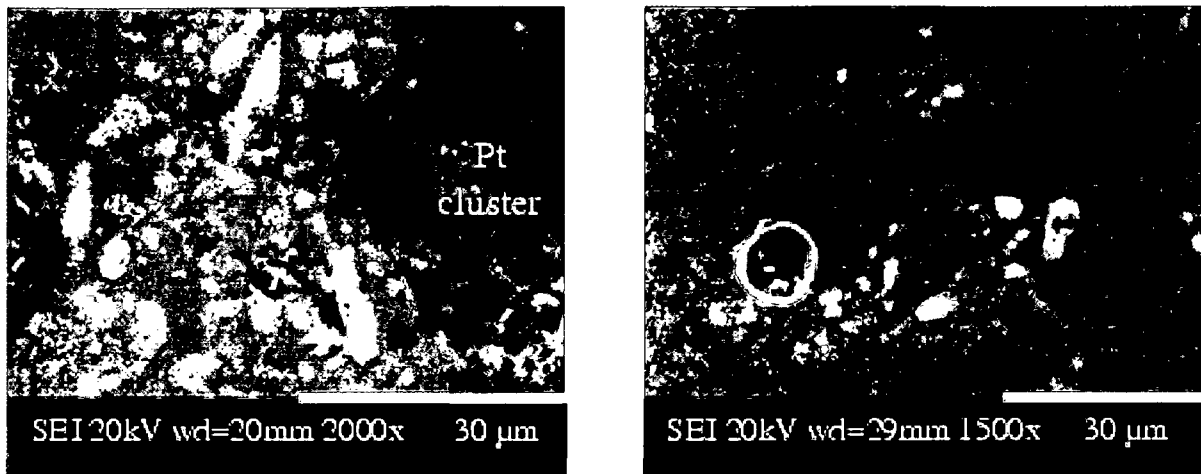


Fig. 18: Y-211 distribution at the surface of sample *R1* (left) and 4.95 mm below the original surface (right).

For the determination of the size of the Y-211 phase, the different orientations of the Y-211 particles with respect to the polished surface have to be taken into account. Therefore, small variations in the detected size depend on how the Y-211 particle was cut. Fig. 17 illustrates this problem. Because of the ellipsoidal shape, the cross sectional areas are smaller than the longitudinal ones.

The left image in Fig. 18 shows some large Y-211 particles near a Pt-cluster with sizes of up to 12 μm . Compared to the size of the Y-211 particles on the right hand side of Fig. 18, they look coarse. After a reduction of the sample thickness by 4.95 mm, a dense distribution of small Y-211 was observed. There the particle sizes are below 5 μm . The investigation of another sample (Li-doped YBCO) showed again, that the Y-211 particles have sizes below 5 μm (Fig. 19). In both samples, Pt additives were used to refine the Y-211 size.

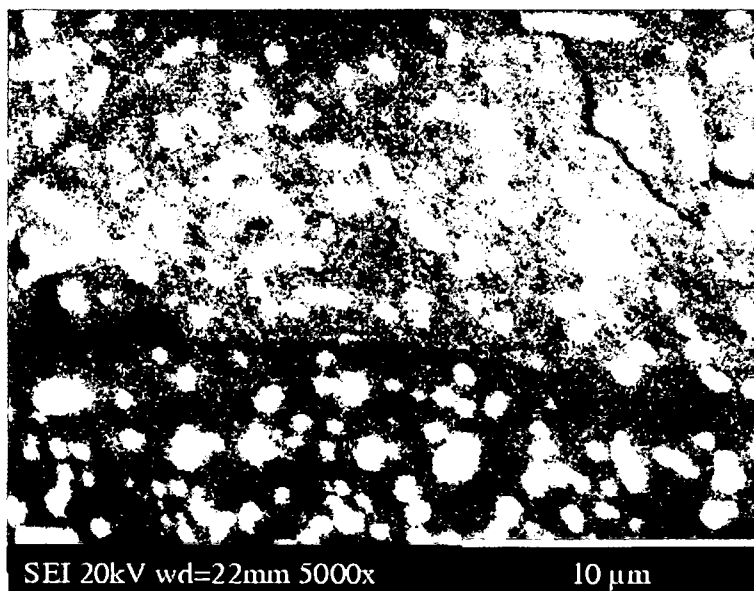


Fig. 19: Y-211 distribution at the surface of sample *Li0at5*.

Another aspect is the Y-211 particle distribution. Investigations particularly by optical microscopy have shown Y-211 rich and Y-211 poor areas. It is remarkable, that in twinned areas often a very low Y-211 concentration was observed, which is in accordance with [33]. In Fig. 20 two images of the same sample with different Y-211 concentration are shown. The images are taken with the same magnification.

Other phases (CuO and BaCuO₂) are often summarized by the term “residual liquid”, which contains Ba-Cu-O phases. CuO has a monoclinic unit cell ($a = 0.4684$ nm, $b = 0.3425$ nm, $c = 0.5129$ nm and $\beta = 99^\circ 28'$), and BaCuO₂ has a cubic unit cell. Other phases are due to additions of Pt and Ce.

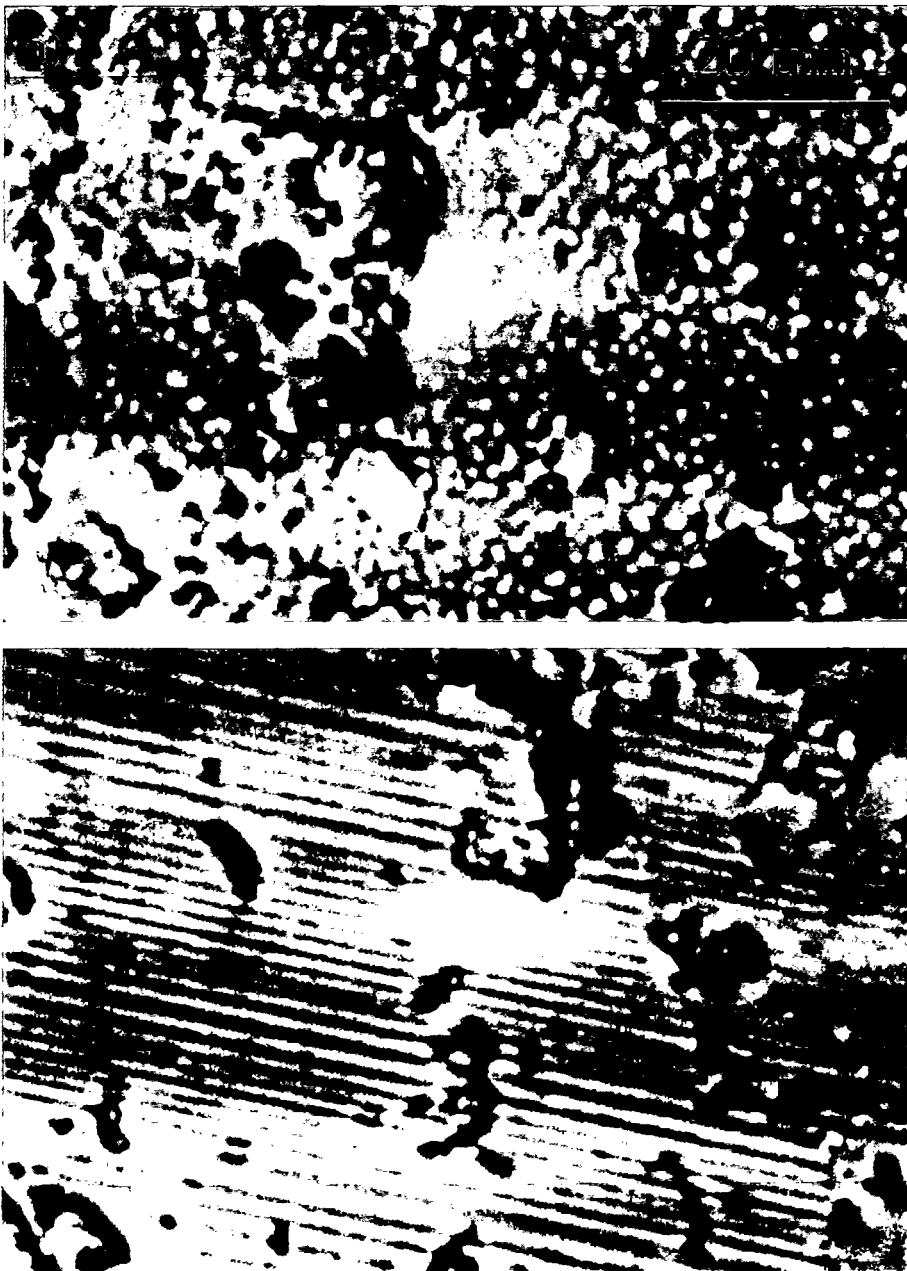


Fig. 20: a) High concentration and b) low concentration of Y-211 particles in sample *Np-11*.

Additives like Pt or Ce tend to form clusters of particles, as shown in Fig. 21, which can clearly be distinguished from Y-211 particles. The size of the clusters is approximately 100 μm , but the size of the individual particles inside the cluster is $10 \pm 5 \mu\text{m}$ and they are of square shape. In Fig. 21a, the polarized light micrograph indicates individual particles by different colors. Scanning electron microscopy confirmed, that the particles inside the cluster have slightly different contrasts. Local EDX showed, that the very bright particles contain a higher amount of Pt. The big white area in Fig. 21a and the black spot in Fig. 21b refer to pores.

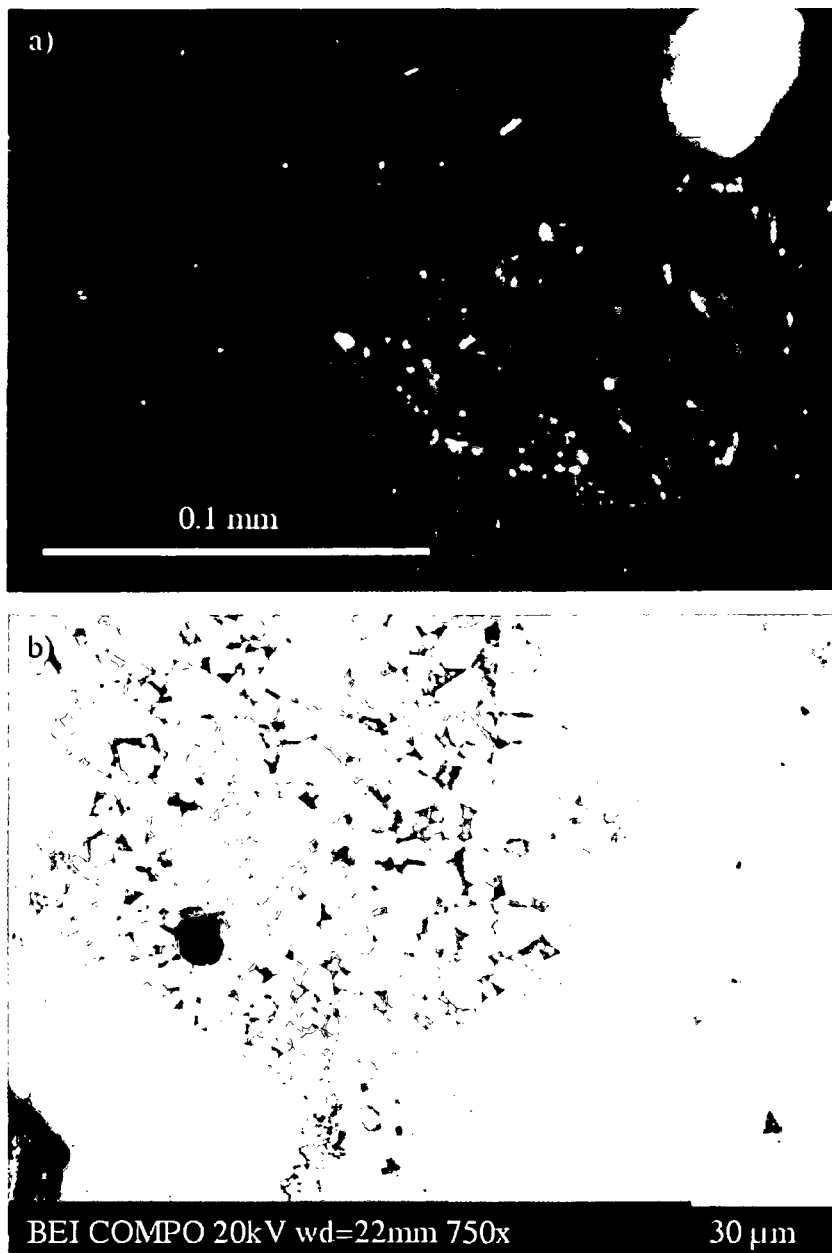


Fig. 21: Pt-rich clusters as found in sample *R1*. a) Polarized light micrograph. b) Backscattered electron image.

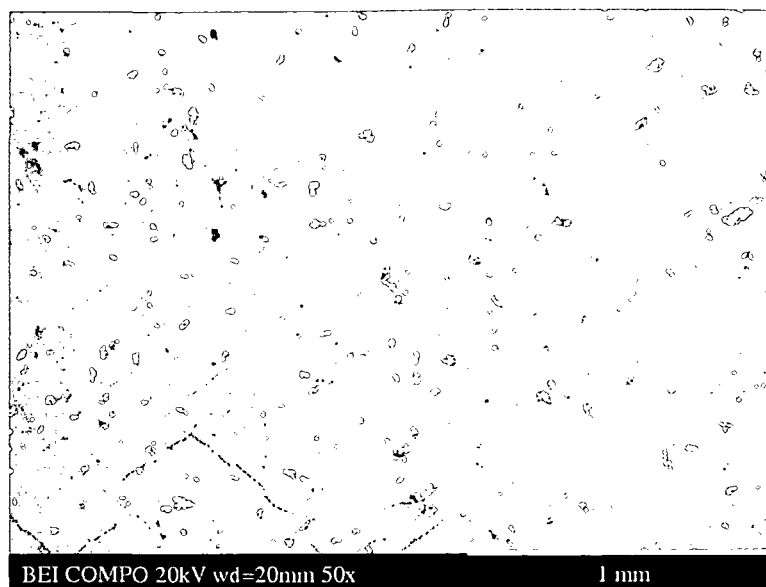


Fig. 22: Backscattering electron image of phases in sample *Li0at5*.

The investigation of the phases in the Li-doped YBCO samples showed (in addition to the Y-211 phase), a homogeneously distributed (white) phase, with dimensions of up to 80 μm and irregular morphology (Fig. 22). Initial EDX measurements indicated that this phase is Ba-enriched. A clear difference between this Ba-rich phase and the Y-211 particles can be seen in Fig. 23. In the secondary electron image on the left, regions with high and regions with low Y-211 content (marked by dotted circles) can be found. There are also some bigger phases, but not all of them are Y-211 particles. The phases can be distinguished in the backscattering electron image (on the right), where the bright white spots refer to the Ba-rich phase and the darker spots to the Y-211 phase.

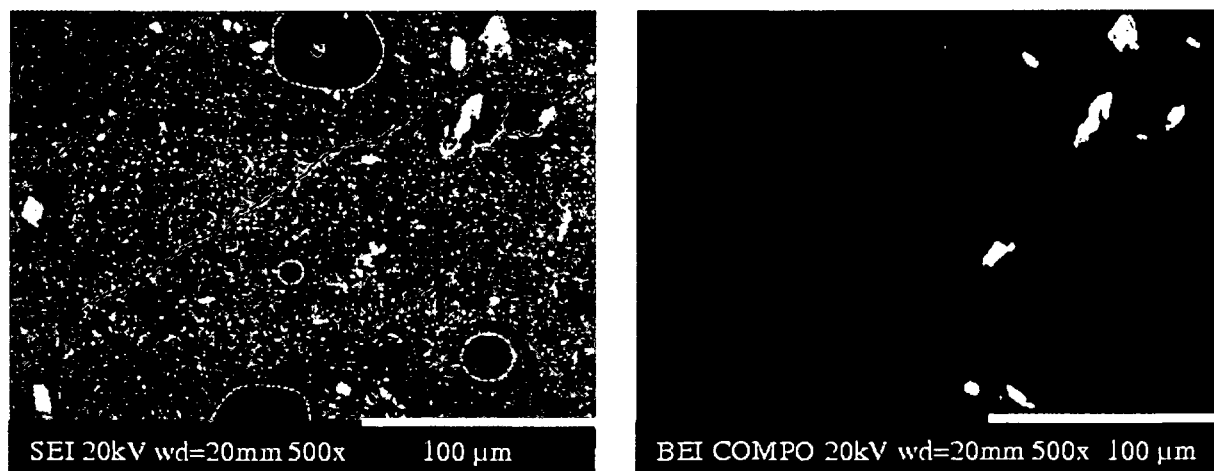


Fig. 23: Determination of phases in the secondary electron image (left) and backscattering electron image (right) in sample *Li0at5*.

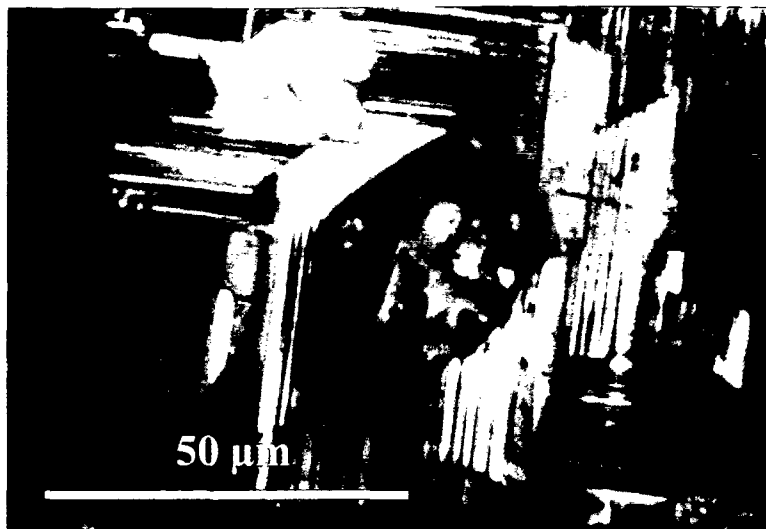


Fig. 24: Twin structure around a Ba-rich particle in sample $Li0at5$.

A polarized light micrograph of such a Ba-rich particle is shown in Fig. 24. The different spacings between the alternating dark and bright stripes are due to the non-uniform stress field caused by the particle. When the stress becomes larger, detwinning occurs and one twin domain becomes dominant. Small detwinned areas can be found at the particle-matrix interface, left above (white) and right above (orange), the particle where the stresses are largest.

Twinning in $YBa_2Cu_3O_{7-8}$ occurs in general at the transformation from the tetragonal (space group: $P4/mmm$) to the orthorhombic (space group: $Pmmm$) state. This phase transformation involves oxygen ordering and takes place during an oxygenation process after

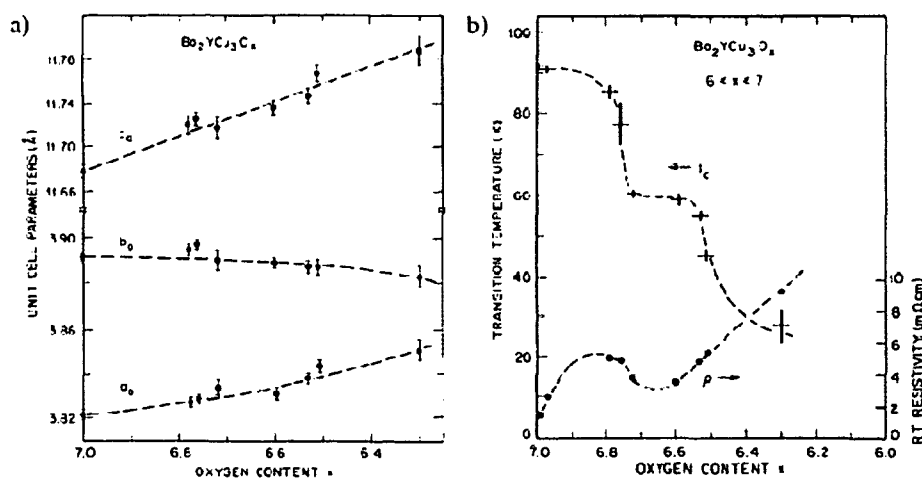


Fig. 25: a) Crystallographic parameters as a function of the oxygen content x . b) Dependence of the transition temperature on the oxygen content x in $YBa_2Cu_3O_x$ (left). Taken from [48].

the melt growth process. In Fig. 25, the lattice parameters from powder x-ray diffraction and T_C from resistive measurements are plotted as a function of the oxygen content $x = 7 - \delta$. With increasing oxygen deficiency δ , oxygen is removed from the CuO chains and a phase transition from the orthorhombic to the tetragonal phase occurs. Although the data in Fig. 25a do not reach so far, it can, however, be recognized that the difference between the lattice parameters a and b tends to vanish. This structural phase transition has a strong influence on the superconducting state, as can be seen from the variation of T_C with x , i.e. the transition temperature drops continuously with increasing oxygen deficiency.

Another example of a twin structure and detwinned areas is illustrated in Fig. 26. A big secondary phase of approximately $45 \mu\text{m} \times 25 \mu\text{m}$ in size and several smaller particles are found to have an influence on the spacing of the lamellae. Around each inclusion detwinned areas can be seen. This varying lamella structure is of course a structural inhomogeneity in the μm -range due to residual stresses, which may lead to fluctuations in the transition temperature [49,50]. The most likely composition of the big inclusion is BaCeO_3 , a phase which is formed in $\text{YBa}_2\text{Cu}_3\text{O}_{7-\delta}$ with an additional amount of CeO_2 or CuO . The smaller particles are possibly large Y-211 particles.

Similar results are shown in Fig. 27, where a polarized light micrograph is compared to a conventional optical light micrograph of the same sample. Again the big inclusions may have the composition BaCeO_3 or CuO . The picture was taken from the c -GS. At this magnification hardly any Y-211 particles are detectable. Moreover, the c -GS was

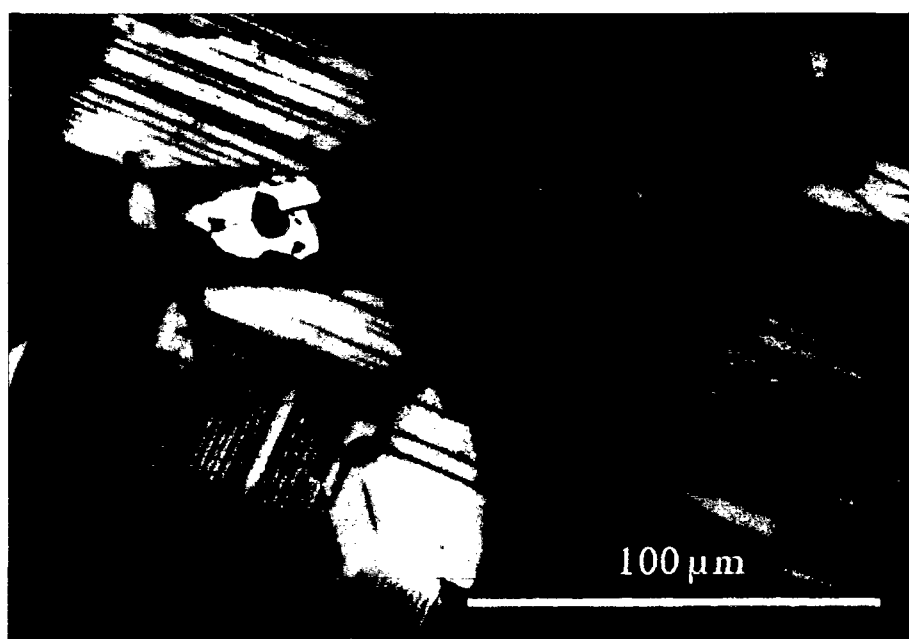


Fig. 26: Polarized light micrograph of a twinned and a detwinned area around an inclusion in sample *Np-11*.



Fig. 27: a) Optical light micrograph and b) polarized light micrograph of the same area in the *c*-GS of sample *Np-11*.

covered by a twin structure. A different picture was found in the *a*-GS of the sample. There, only a few twinned structures and much more Y-211 particles were found. Their average size in Fig. 28a is $\sim 3 \mu\text{m}$. An Y-211 poor region around an inclusion (CuO or Ce-containing phase) is marked by the dotted line.

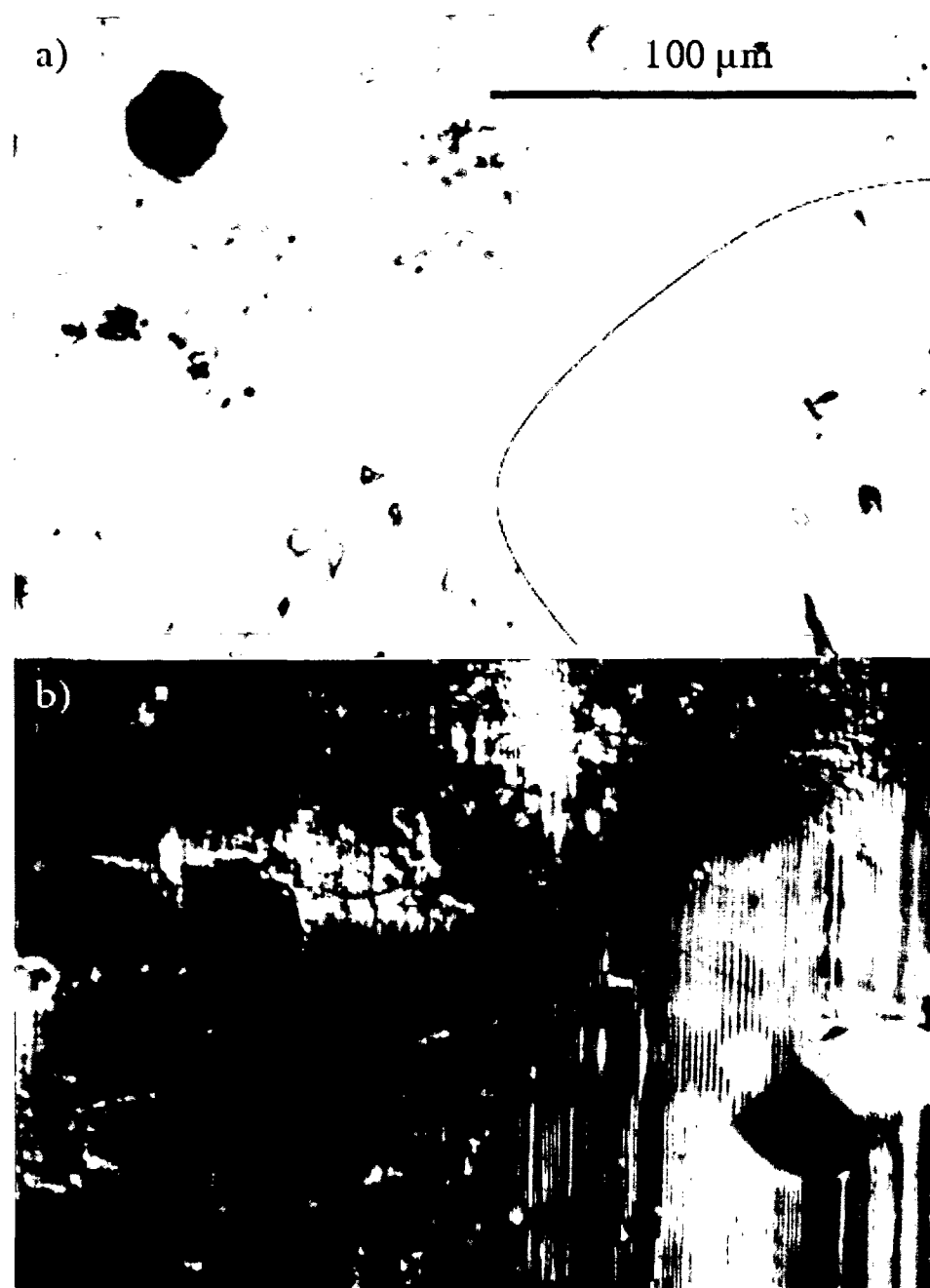


Fig. 28: a) Optical light micrograph and b) polarized light micrograph of the same area in the *a*-GS of sample *Np-11*.

2.2 Grain boundaries and cracks in melt-grown samples

Grain boundaries play an important role in melt grown bulk superconductors. They generally exhibit a weak link behavior and limit the critical current in the superconducting monolith. Grain boundaries can be classified according to the mismatch angle between adjacent grains. If the angle is smaller than 15° , the grain boundary is called a low angle grain boundary (LAGB). LAGBs can be described by an array of dislocations. High angle grain boundaries (HAGB) possess a high mismatch angle between the grains.

Regions in the superconducting monolith, which are separated by low angle grain boundaries, are often referred to as subgrains. In bulk superconductors, this growth related structure is formed by the arrangement of dislocations [51]. Dislocations in $\text{YBa}_2\text{Cu}_3\text{O}_{7-8}$ appear during crystal growth mainly due to the incorporation of the Y_2BaCuO_5 particles [52].

It is commonly observed, that the number of dislocations and, therefore, the number of grain boundaries increases with increasing distance from the seed. Fig. 29 shows a scanning electron micrograph of various high angle grain boundaries, some of them are marked by dotted lines. These highly misaligned grains were found at the edge of sample *Li0at5*.

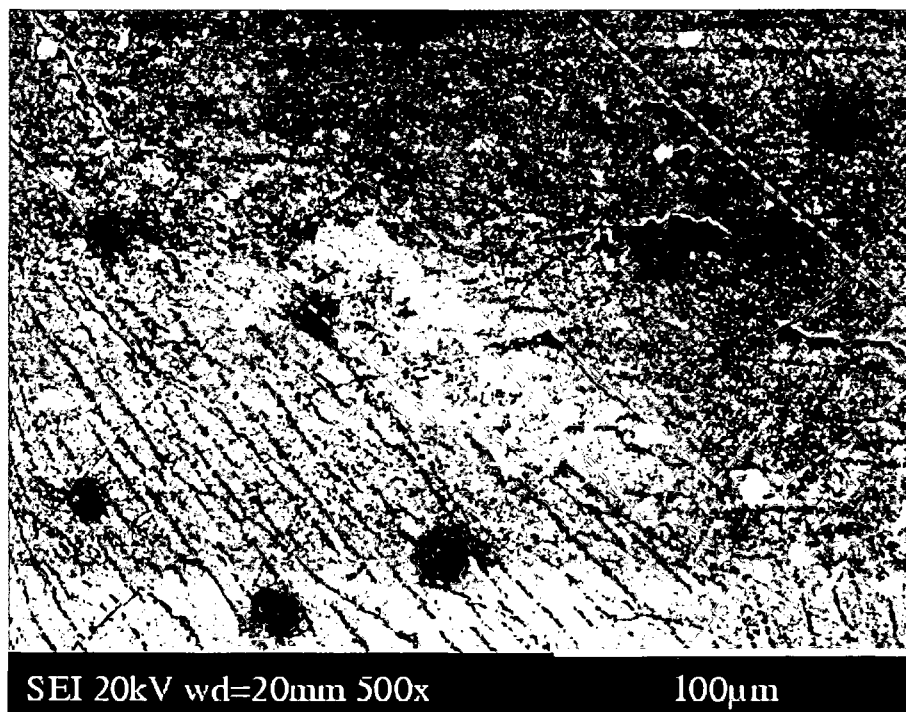


Fig. 29: Grain boundaries visible in the secondary electron image in sample *Li0at5*.

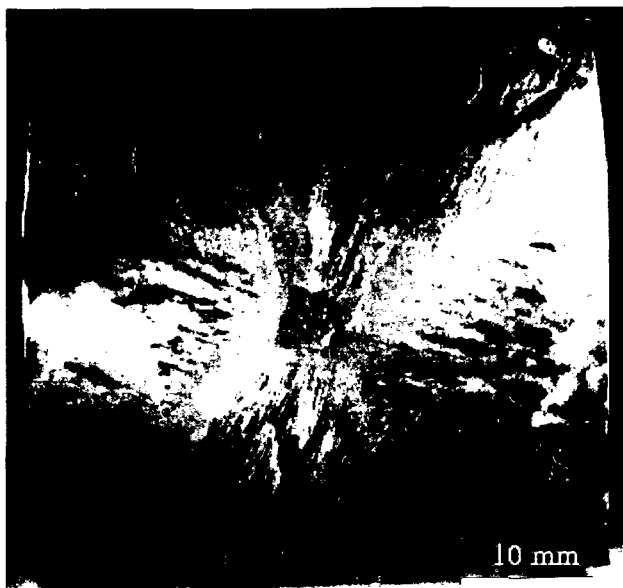


Fig. 30: Grains and subgrains in sample *SLY-14-38* after having reduced the thickness by 1.30 mm.

The number of grains and subgrains increases not only in radial, but also in vertical direction. Fig. 30 shows a photograph of sample *SLY-14-38* after having removed a surface layer of 1.30 mm. The different orientations can be readily observed because of the different contrasts. In this sample large dark grains appeared with increasing vertical distance from the seed. The four α -GSs, the formation of the subgrains and subgrain-free regions along the α - α -GSBs are observed as well. This common feature of melt grown monoliths (compare Fig. 31) is also observed in Hall scans of the trapped flux and in the pattern of the magnetoscan, which will

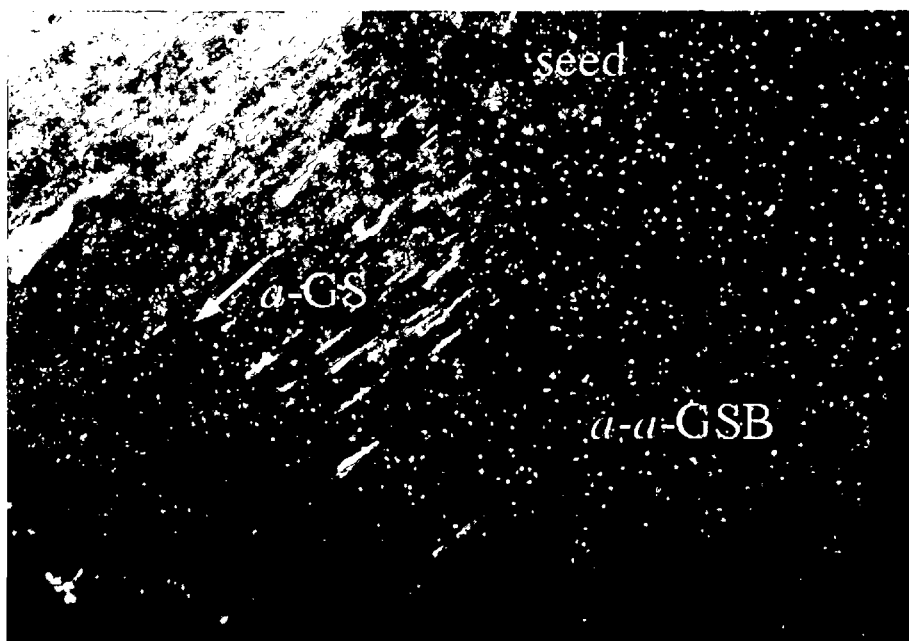


Fig. 31: Subgrains in the α -GS and subgrain free α - α -GSB in sample *Li0at5* after a thickness reduction of 2.90 mm.

be discussed in *Chapter 6*. Along the GSBs the grain growth is considered to take place perpendicularly to the main growth front. It was suggested, that the subgrain-free regions were formed during an incubation period of the growth, in which the dislocation density at the growth front is too small to form dislocation walls [52].

Another fabrication related phenomenon are cracks in high temperature superconducting monoliths. Cracks are formed by stresses, which have their origin *i)* in the different thermal expansion coefficients of $\text{YBa}_2\text{Cu}_3\text{O}_{7-\delta}$ and Y_2BaCuO_5 as well as *ii)* in the lattice parameter dependence on the oxygen stoichiometry. Different types of cracks are observed in a bulk superconductor: *a-b*-microcracks, *a-b*-macrocracks and *c*-macrocracks. Their formation was summarized in a review article by Diko [44]. Whereas the *a-b*-microcracks are caused by stresses around Y-211 particles, macrocracks originate from macroscopic inhomogeneities, e.g. the macroscopic variation of the Y-211 concentration inside the bulk monolith or they are introduced during the oxygenation process. Recent oxygenation experiments revealed the possibility of the formation of *c*-macrocrack networks on the sample surface [53]. On the one hand, these networks release residual macrostresses and prevent the bulk from cracking fatally. On the other hand, the macrocracks limit the effective current density and also the trapped field of the bulk superconductor. Fig. 32 shows a *c*-macrocrack network on the top surface of sample *Li0at5*. It should be noted, that the size of these cracks is larger in a region with high Y-211 concentration (right) compared to a region with low Y-211 concentration (left). *C*-macrocrack network will be discussed again in *Chapter 7*.

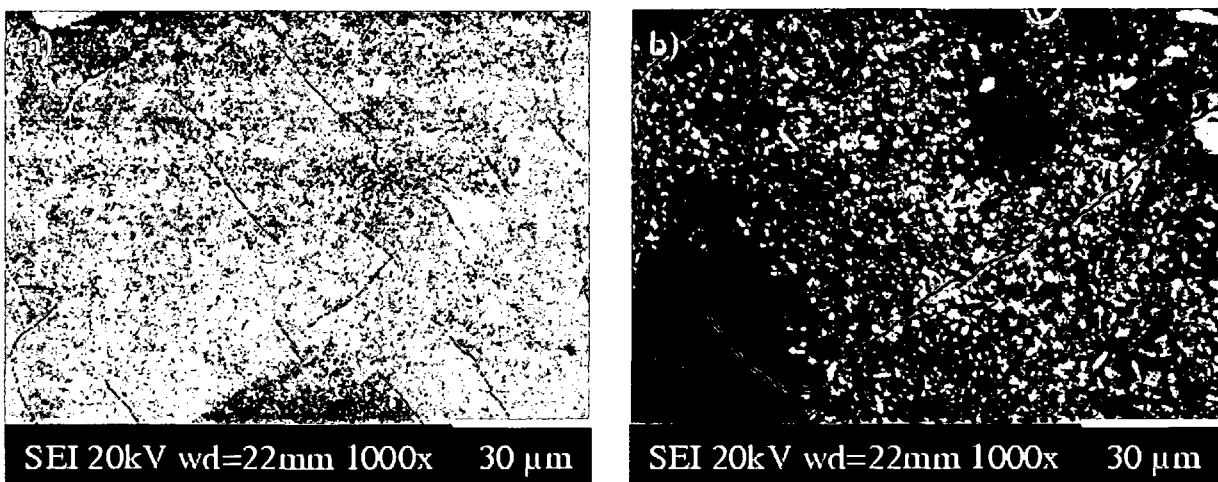


Fig. 32: Observation of a *c*-macrocrack network on the surface of sample *Li0at5*: a) region with low Y-211 concentration and smaller cracks b) region with high Y-211 concentration and longer cracks.

2.3 Grain boundaries in MSMG samples

Grain boundaries in multi-seeded-melt grown samples depend on a number of parameters, such as the number of seeds, the distance between them and their arrangement. Fig. 33 explains schematically the formation of a grain boundary between two adjacent grains grown by neighboring seeds. It was often confirmed that the GBs act as weak links resulting in a local depression of the trapped flux, since the current flow across these grain boundaries is generally sensitive to misorientations of the grains (and, therefore, dependent on the seed orientation), and to the normal phases accumulated there. Considering the growth of the bulk superconductor, the GB will first appear when the a -GSs of adjacent grains collide. A segregation of the pushed residual melts (excess Cu and Ba) and the Y-211 phase will occur there, as long as the growth fronts propagate in a -direction. According to Fig. 33, it can be expected, that after a certain progression in growth, the c -GSs will collide. Therefore, according to the change in the growth direction, the pushing should also change from a - into c -direction. Then the GB should reduce its lateral dimension, which results in a stronger coupling between the grains.

In order to obtain melt-free GBs, several attempts have been made to eliminate the melt at the GBs by varying the processing parameters [54-56]. In this work, the GBs of a MSMG bulk superconductor and their influence on the trapping behavior were investigated as a function of the distance from the seed. The idea was, that after a stepwise reduction of the thickness of the sample, an improvement in the connectivity between the grains should occur due to the reduction of the size of the GBs. A microstructural study of the GBs was carried out by scanning electron microscopy and optical light microscopy. Fig. 34 shows results of the microstructural investigations. Three channels were investigated by EDX: Y, Ba and Cu.

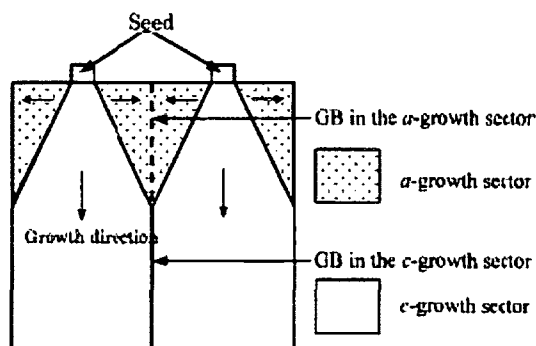


Fig. 33. Formation of a grain boundary between two seeds.

The illustration is taken from [57].

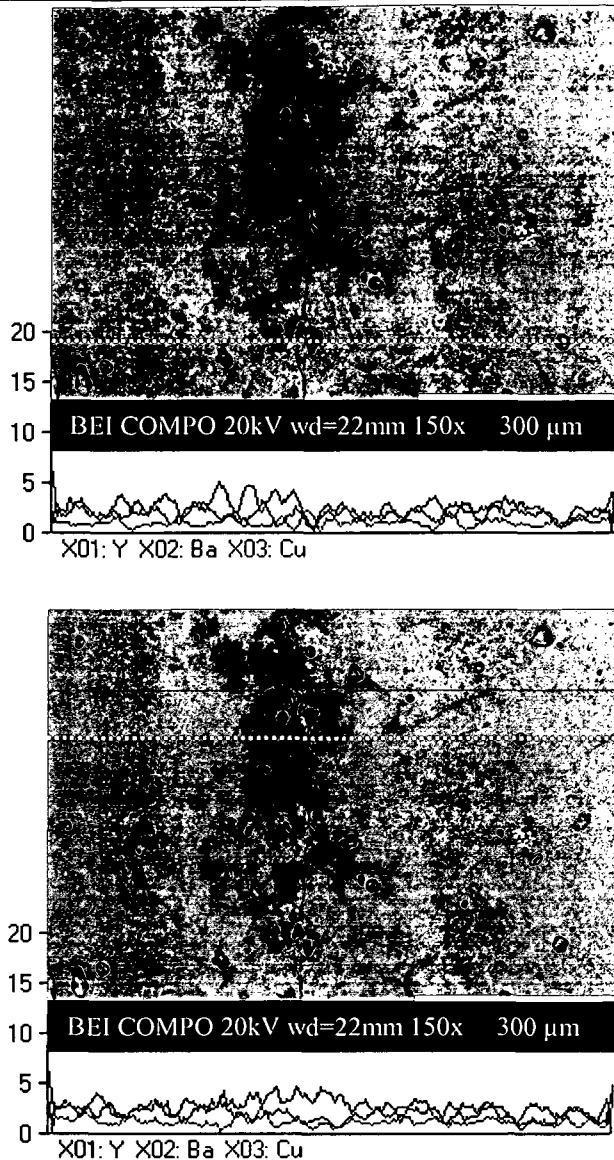


Fig. 34: EDX result of line scans across one GB of sample *R1* for the channels 1 = Y, 2 = Ba and 3 = Cu.

An enhancement of yttrium (Y-211) and copper (CuO) was found in line scans (dotted line) across the GB at two different positions. The higher Y-211 amount can also be recognized by a difference in contrast. Compared to the Y-123 matrix, Y-211 is lighter. On the other hand, the dark phase, which is more irregularly distributed around the GB, consists of excess-copper. Moreover it was found that the GBs contained a well visible crack. Their lateral extent at the top of the original sample was up to 400 μm . The white cluster in the Y-123 matrix in Fig. 34 contains a Pt-rich phase.

Fig. 35 shows a comparison between an optical micrograph of a GB of sample *R1* and a scanning electron micrograph of the same area with nearly equal magnification. The “green phase” is easily detected in the optical image, Fig. 35a. A comparison with the backscattering electron image, 35b, also shows high amount of residual melt – mainly excess Cu – around the GB. It can be observed too, that the lateral extension of the GB increases at the outer edge

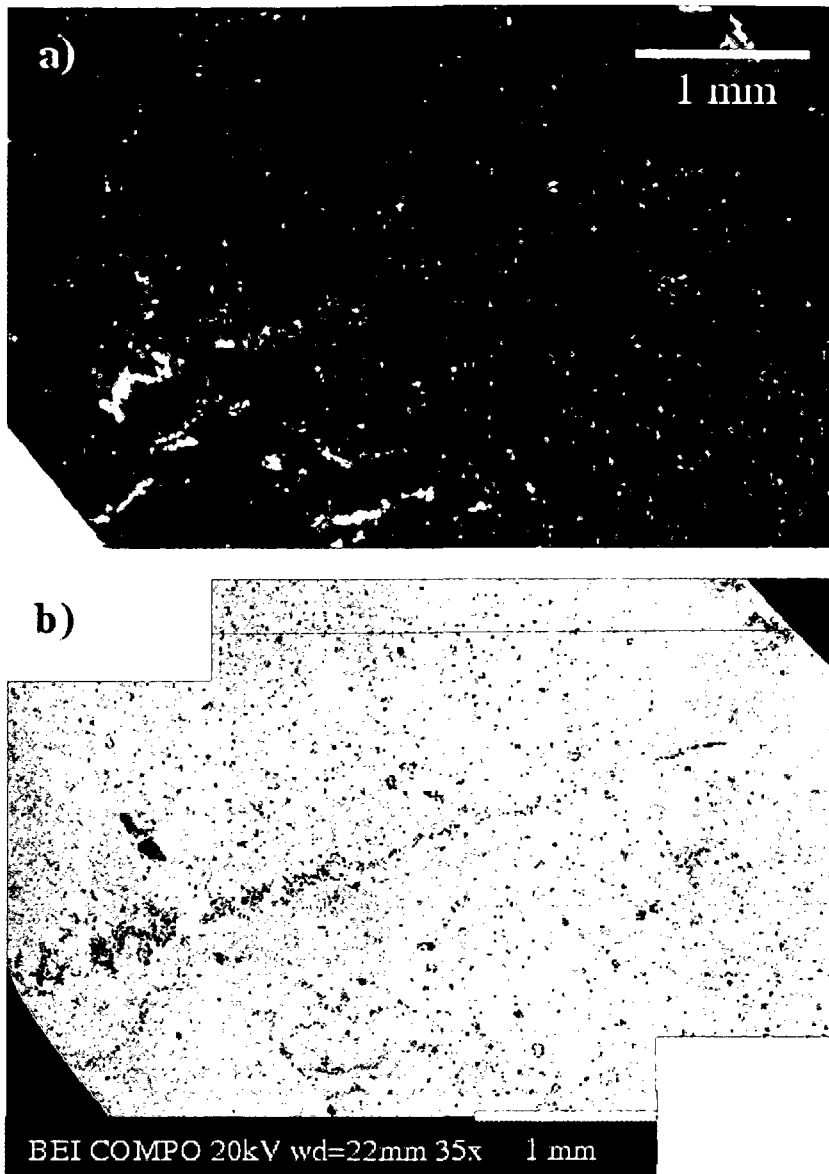


Fig. 35: Comparison between a) optical micrograph and b) scanning electron micrograph of a GB in sample *R1*.

of the sample. This is explained by the arrangement of the seeds on top of the annular sample and the resulting mismatch angle between the grains. From geometrical considerations it is clear, that the grains tend to collide first at the inner edge of the ring shaped sample. Therefore, the amount of residual melt and of normal phases is higher at the outer edge of the ring.

A higher magnification of the middle part of the GB in Fig. 35 is shown in Fig. 36. A secondary electron image of the GB confirms the accumulation of the Y-211 particles. The darker background refers again to residual melt with a higher Cu content. The size of the larger Y-211 particles is of 10 μm . The crack between the grains has a size of roughly 1 μm .

After having removed 4.95 mm from the top of the sample, the extension of the GB

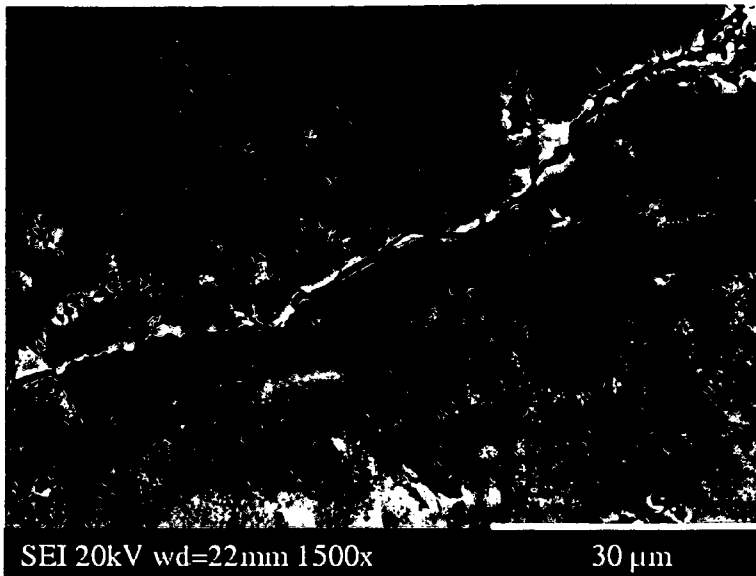


Fig. 36: Secondary electron image of a GB of sample *R1* showing Y-211 particle accumulation.

was reduced from 400 μm to around 50 μm , but there was still a higher amount of Y-211 particles and residual melt. No “clean” GB could be observed so far. Also the results from Hall scans of the trapped field and from the magnetoscan did not indicated any improvement in the grain connectivity. This is caused by the existence of a narrow crack at the GB itself, which suppresses the current flow between the grains. An interesting feature showed sample *MS-1*, which was grown with three seeds. The upper right seed was, however, oriented differently on the precursor compared to the other two seeds. The boundary was observed in a polarized light microscope (Fig. 38), which showed a high contrast between the adjacent

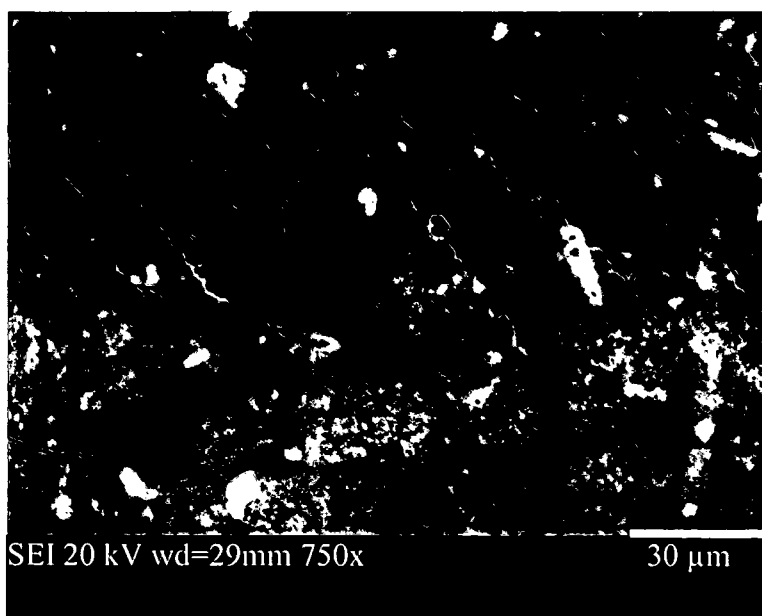


Fig. 37: GB in sample *R1* after having removed 4.95 mm from the original thickness of 11.90 mm.

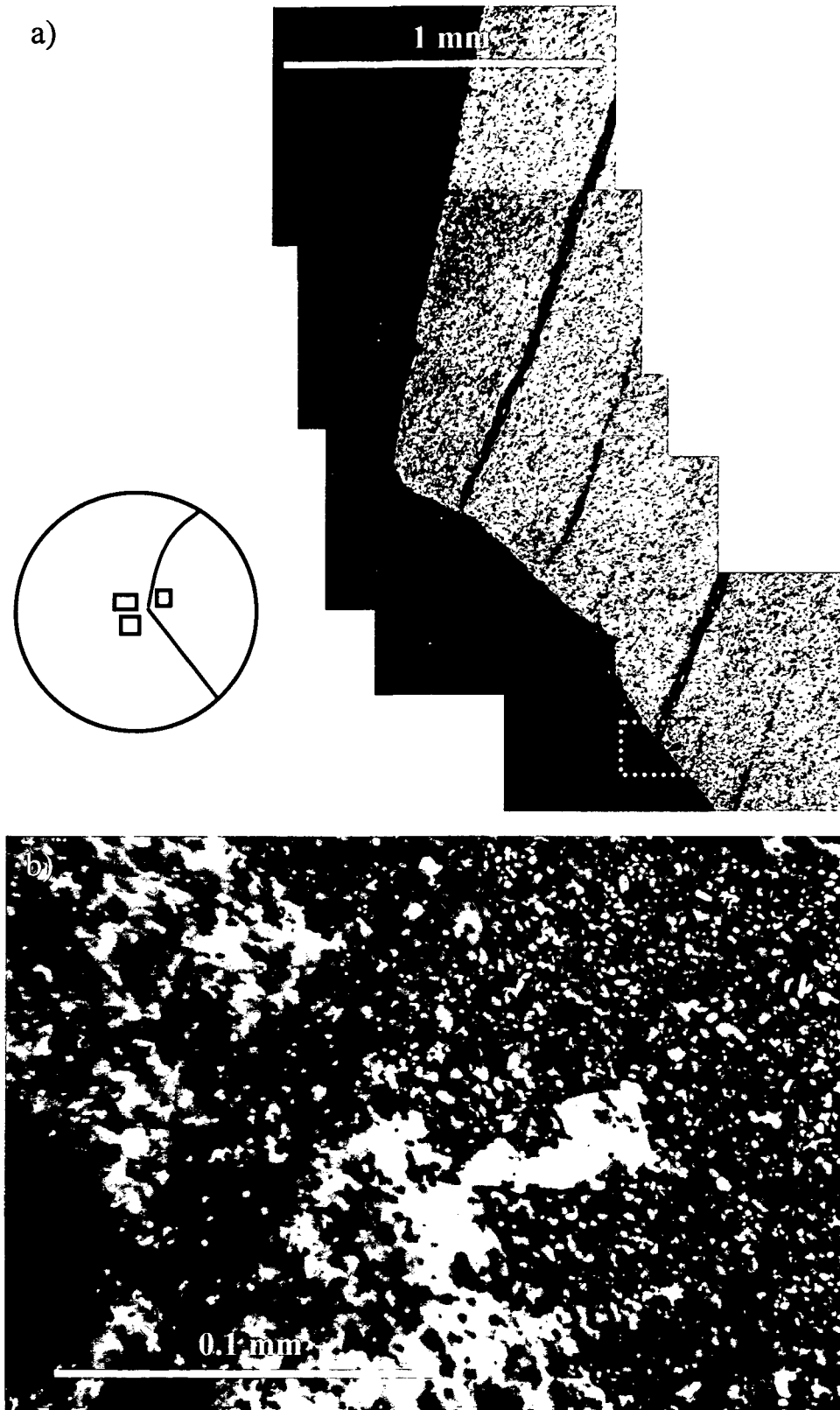


Fig. 38: Grain boundary in sample *MSI*. a) Polarized light micrograph of the GB illustrated on the left; b) magnification of the GB and Y-211 distribution.

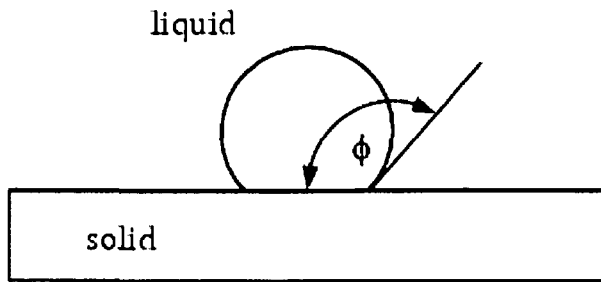


Fig. 39: Definition of the melt wetting angle.

grains.

Often, grain boundaries in MSMG samples show the formation of a melt channel. The presence of residual liquids can be responsible for the drop of the trapped field along the grain boundary. The amount of residual liquids at the boundaries is explained by the interfacial energy of the boundaries. This term influences the melt wetting angle ϕ , which is defined as the contact angle between the liquid and the solid phase (see Fig. 39). Clearly, the wetting tendency increases with decreasing melt wetting angle. The different morphological shapes of the residual melt at a grain boundary in MSMG can be explained by the melt wetting angle ϕ , indicated in Fig. 40.

Optical micrographs of the grain boundary between the two seeds of sample *MS-3* clearly show a melt channel. An important parameter is the melt composition. Therefore, a possible reason for the appearance of the melt channel is that the melt is off-stoichiometric, i. e. no more Y-123 phase can be formed. A second parameter that influences the melt wetting angle is the orientation of the seed crystals relative to each other, which defines the “type of the junction” [54]. In the case of sample *MS-3*, the junction was of the type (100)/(100).

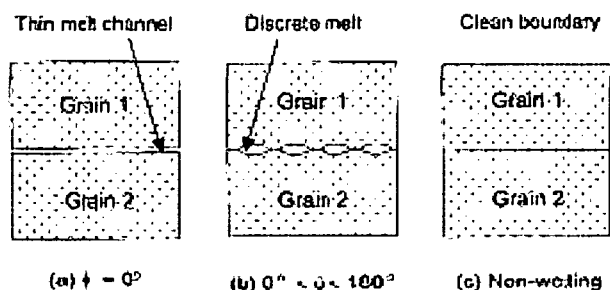


Fig. 40: Relationship between melt wetting angle ϕ and the shape of the melt at the boundaries [58].

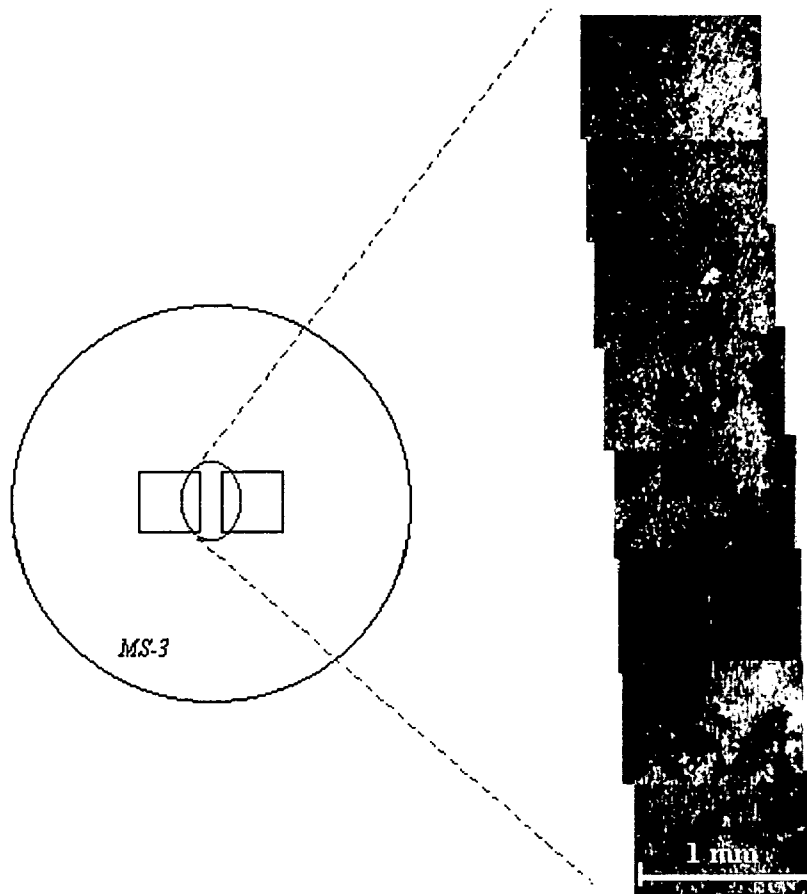


Fig. 41: Optical micrograph of the grain boundary between the seeds of sample *MS-3*.

SAMPLES

This section contains all relevant information on the samples investigated in this work. It is structured according to the manufacturers. Table 2 shows an overview of sample codes and manufacturers.

Table 2: Samples and manufacturers

sample code	description	precursor composition	manufacturer and contracts
<i>Li0at5</i>	<i>Li-doped YBCO</i>	$YBa_2Cu_3O_{7.8}$ Y_2O_3 Li_2CO_3 Pt	<i>IFW Dresden</i> <i>L. Shlyk, G. Krabbes</i>
<i>Li0at6</i>			
<i>Li0at6Nr2</i>			
<i>Lip1</i>			
<i>BK a,b,c,d,e,l</i>			
<i>Np-6</i>	<i>YBCO</i>	$Y_{1.5}Ba_2Cu_3O_{7.8}$ CeO_2	<i>IPHT Jena</i> <i>D. Litzkendorf</i>
<i>Np-11</i>			
<i>SLY-14-21</i>	<i>YBCO</i>	<i>unknown</i>	<i>NEXANS</i> <i>Superconductors GmbH</i> <i>H. Walter</i>
<i>SLY-14-32</i>			
<i>H186</i>	<i>YBCO</i>	$YBa_2Cu_3O_{7.8}, Y_2O_3, CeO_2$	<i>ZfW Göttingen</i>
<i>R1</i>	<i>YBCO</i>	$YBa_2Cu_3O_{7.8}$ Y_2BaCuO_5 Pt	<i>IRC Cambridge</i> <i>N. Hari Babu, D. Cardwell</i>
<i>MS-1</i>			
<i>MS-2</i>			
<i>MS-3</i>			
<i>MS-4</i>			
<i>SLY 65-22t</i>	<i>Ag-joined YBCO</i>	$YBa_2Cu_3O_{7.8}$ Y_2BaCuO_5, Ag	<i>ICMAB Barcelona</i> <i>X. Granados</i>
<i>SLY 14-14fd2t</i>			

3.1 Samples from IFW Dresden

3.1.1 Bulk samples

The samples from IFW Dresden, analyzed in this work, are Li-doped $\text{YBa}_2\text{Cu}_3\text{O}_{7-\delta}$ superconductors. The precursor powder for these samples consisted of commercial Y-123, Y_2O_3 and Li_2CO_3 . All powders had a purity of at least 99.99 %. Pt-addition (2 wt% Pt) was used. The bulk was grown in the modified melt crystallization process (MMCP) using a $\text{SmBa}_2\text{Cu}_3\text{O}_{7-\delta}$ seed crystal. Fig. 42 shows a schematic view of the heat treatment of the samples. After heating the pressed pellets to 1050 °C, the temperature was reduced to the growth temperature of 1020 °C. The samples were cooled down first slowly (0.5 °C/h) to 950 °C, then faster (50 °C/h) to 600 °C and finally to room temperature. The grown samples were annealed in flowing oxygen at a temperature of 380 °C for 300 h [37], alternatively at a temperature of 400 °C [59] also for 300 h or at a temperature of 380 °C for 350 h [40]. Details of the samples can be found in Table 3. Concentrations of 0.5 at % Li or 0.6 at% Li refer to the chemical formula $\text{YBa}_2(\text{Cu}_{0.95}\text{Li}_{0.05})_3\text{O}_{7-\delta}$, $\text{YBa}_2(\text{Cu}_{0.94}\text{Li}_{0.06})_3\text{O}_{7-\delta}$ respectively. For sample *Lip1*, the processing parameters were different (additional pressure). Sample *Li0at5* was characterized in vertical direction. Therefore, the thickness of this sample was reduced stepwise (see 6 Discussion). Samples *Li0at6* and *Li0at6Nr2* were neutron irradiated at ATI, sample *Lip1* was sent back to IFW

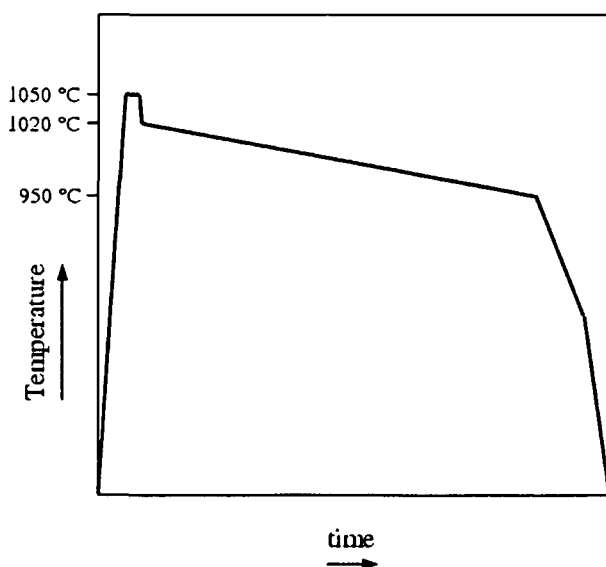
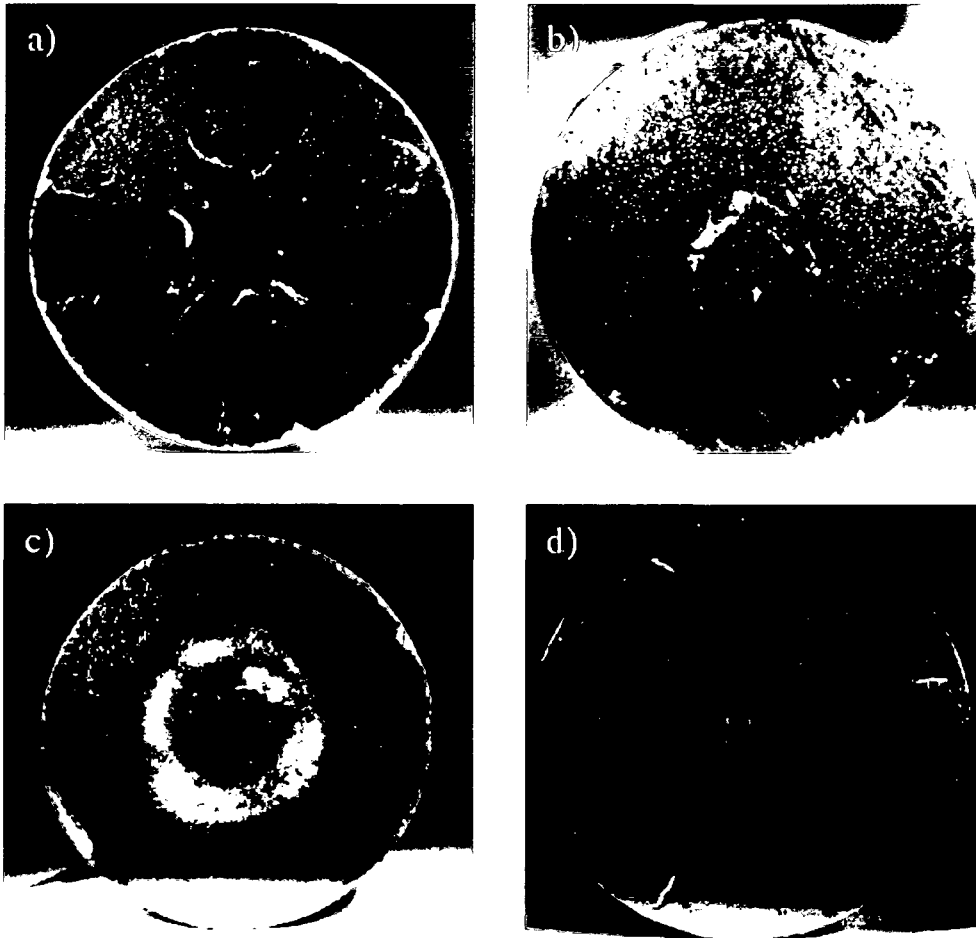


Fig. 42: Temperature profile of the MMCP.

Table 3: Li-doped $\text{YBa}_2\text{Cu}_3\text{O}_{7-\delta}$ bulk superconductors from IFW Dresden.

sample code	<i>Li0at5</i>	<i>Lip1</i>	<i>Li0at6</i>	<i>Li0at6Nr2</i>
composition	0.5 at% Li	0.5 at% Li	0.6 at% Li	0.6 at% Li
mass	29.75 g	29.17 g	27.16 g	32.84 g
thickness	9.00 mm	9.30 mm	8.20 mm	10.20 mm
diameter	26.42 ± 0.22 mm	26.30 ± 0.45 mm	26.54 mm	26.18 ± 0.08 mm
received on	14 04 2003	09 09 2003	29 09 2002	01 03 2004
status	unirr ATI Vienna	sent back to IFW Dresden	irr ($2 \cdot 10^{21} \text{ m}^{-2}$) ATI Vienna Chemistry Lab damaged	irr ($2 \cdot 10^{21} \text{ m}^{-2}$) ATI Vienna Chemistry Lab

Dresden after characterization. Photographs of all samples are shown in Fig. 43. The surface of the samples was polished before the measurements with SiC abrasive paper and diamond paste. Sample *Li0at6* had an original thickness of 9.9 mm. Due to a massive crack parallel to the *a-b* plane near the bottom, the thickness was reduced to 8.2 mm (see Table 3), in order to

Fig. 43: Top surfaces of a) *Li0at5* b) *Lip1* c) *Li0at6* and d) *Li0at6Nr2*

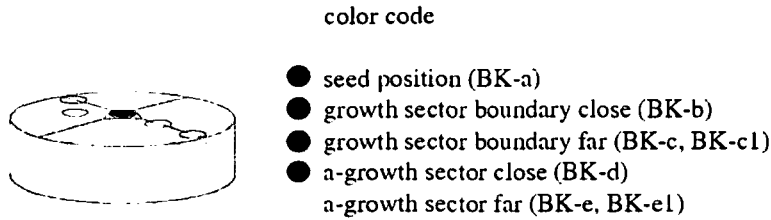


Fig. 44: Positions in the bulk monolith, from which small specimens were cut.

achieve a coplanar geometry.

3.1.2 Reference samples

In addition to the bulk samples, seven small cylindrical specimens, cut from different locations of a Li-doped $\text{YBa}_2\text{Cu}_3\text{O}_{7.8}$ monolith, were investigated by VSM measurements. The specimens were cut using an ultrasonic drilling machine [37]. Their diameter is 3 mm and the average thickness is 1.35 ± 0.65 mm. Fig. 44 shows the positions in the bulk monolith, from which the specimens were cut with an additional color code. Their lithium concentration is 0.5 - 0.6 at.% Li, which is comparable to the concentrations of the previous bulk samples.

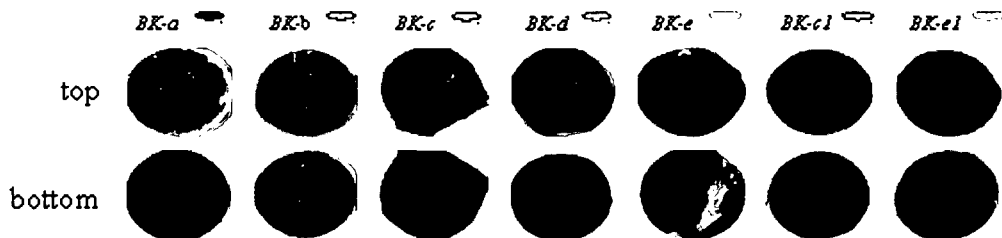


Fig. 45: Photographs of the top and the bottom surface of the reference samples.

3.2 Samples from IPHT Jena

Two YBCO bulk samples from IPHT Jena originating from the same batch were investigated. The nominal composition of the precursor is $Y_{1.5}Ba_2Cu_3O_{7.8} + 1 \text{ wt.}\% \text{ CeO}_2$. To achieve this composition, a commercial prereacted $YBa_2Cu_3O_{7.8}$ powder with an excess of Y_2O_3 and an addition of CeO_2 was used. The samples were prepared by the modified melt crystallization process. During growth the samples were cooled down slowly with a rate of $0.2\text{-}1 \text{ }^\circ\text{C/h}$. Contrary to reference [60], a Sm-123 seed crystal was used [61]. After growth the samples were oxygenated. Table 4 summarizes the parameters of samples *Np-6* and *Np-11*. The top surfaces (Fig. 46) of the samples were polished before the measurements with SiC abrasive paper and diamond paste. Both samples were irradiated at ATI to a fluence of $2 \cdot 10^{21} \text{ m}^{-2}$. Unfortunately sample *Np-6* was damaged due to water leakage into the quartz capsule during irradiation. Fig. 47 documents the result. Results on the irradiation of the sample *Np-11* can be found in Chapter 6 *Discussion*.

Table 4: YBCO bulk superconductors from IPHT Jena

sample code	<i>Np-6</i>	<i>Np-11</i>
mass	34.71 g	34.76 g
thickness	11.95 mm	12.00 mm
diameter	25.00 mm	25.00 mm
received on	17 10 2003	13 04 2004
status	<i>irr</i> ($2 \cdot 10^{21} \text{ m}^{-2}$)	<i>irr</i> ($2 \cdot 10^{21} \text{ m}^{-2}$)
	ATI Vienna	ATI Vienna
	Chemistry Lab	KIL #14
	<i>damaged</i>	

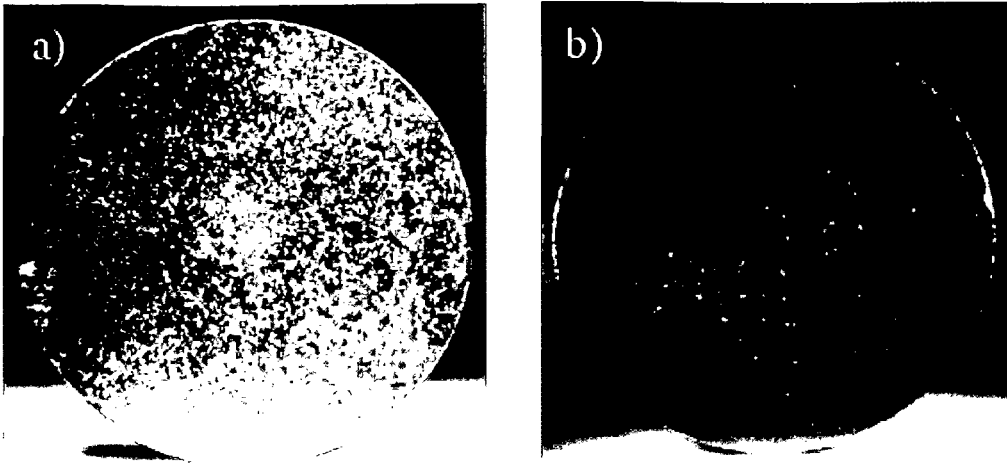


Fig. 46: Top surfaces of a) *Np-6* and b) *Np-11*



Fig. 47: Water leakage into the quartz tube after irradiation and damaged sample *Np-6* [62].

3.3 Samples from Nexans SuperConductors GmbH

Two $\text{YBa}_2\text{Cu}_3\text{O}_{7.8}$ samples from Nexans SuperConductors GmbH were investigated. No detailed process parameters are available, but both samples, *SLY-14-21* and *SLY-14-32*, originate from the same batch. The values of the levitation force were reported to be 89.98 N for sample *SLY-14-21* and 84.02 N for sample *SLY-14-32*, respectively. A SmCo permanent magnet of 25 mm diameter and 15 mm thickness was used for levitation force measurements in liquid nitrogen. The distance between magnet and sample was 0.2 mm [63]. In addition, trapped field measurements were reported with a maximal trapped field of around 700 mT. Detailed parameters of the Hall scans (scan grid, gap between Hall probe and sample surface, etc.) are not available. The reported results are shown in Fig. 49. In the meantime the process parameters were changed in order to obtain more homogeneous samples. The sample parameters can be found in Table 5. Fig. 48 shows the top surface of the samples.

From sample *SLY-14-21* four slices were cut along the *a-c* plane. The slices were polished and analyzed by the magnetoscan technique. In order to obtain information on the microstructure, scanning electron microscopy was employed. The dimensions of sample *SLY-14-32* were changed too, i.e. its thickness was reduced in two steps from 9.60 mm to 8.30 mm.

Table 5: YBCO bulk superconductors from NEXANS company

sample code	SLY-14-21	SLY-14-32
levitation force	89.98 N	84.02 N
mass	85.57 g	84.48 g
thickness	9.90 mm	9.60 mm
a × b	38.35 × 38.30 mm	38.30 × 38.00 mm
received on	03 07 2003	03 07 2003
status	unirr, cut into slices	unirr
	ATI Vienna	ATI Vienna

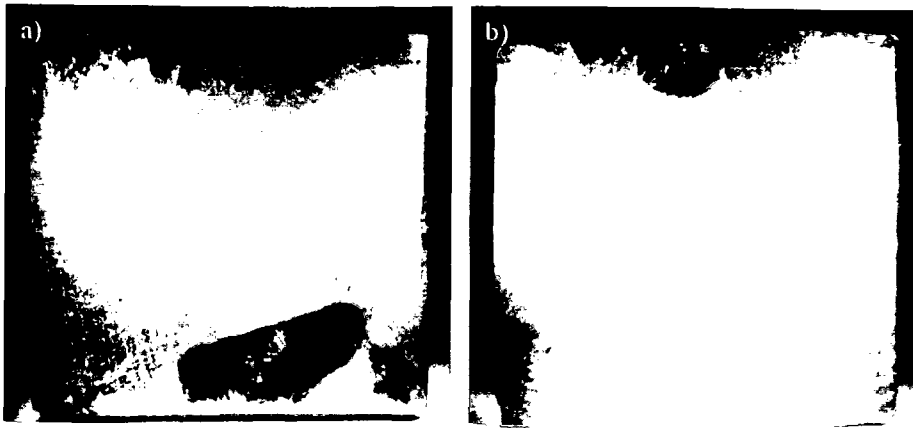


Fig. 48: Top surfaces of a) *SLY-14-21* and b) *SLY-14-32*

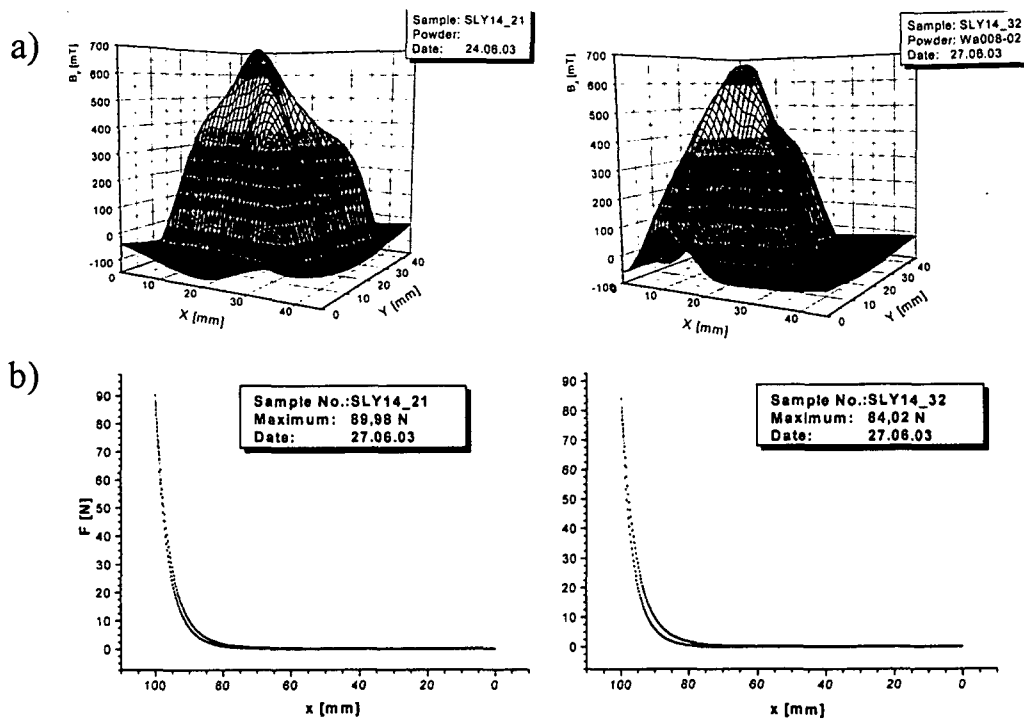


Fig. 49: Trapped field and levitation force data [63].

3.4 Sample from ZfW Göttingen

One $\text{YBa}_2\text{Cu}_3\text{O}_{7-8}$ sample was manufactured at ZfW Göttingen. The exact process conditions are not available. Before the sample was sent to the Atomic Institute, EDX measurements were performed at different positions of the sample surface at Göttingen. The results show a mean Y-211 content of 18 ± 6 mol% [64]. Fig. 50 illustrates the positions, where the Y-211 content was measured (see also [65]). Hence, it can be assumed that the initial precursor composition was approximately $\text{YBa}_2\text{Cu}_3\text{O}_{7-8} + (25 \pm 5)$ mol% Y_2O_3 and maybe + 1 wt.% CeO_2 , which would be similar to the composition quoted in [56, 66].

Table 6: Y-123 and Y-211 contents at the surface of sample *H186* at different positions

pos.	Y-123	Y-211
<i>B1</i>	88 mol%	12 mol%
<i>B2</i>	81 mol%	19 mol%
<i>B3</i>	80 mol%	20 mol%
<i>W1</i>	82 mol%	18 mol%
<i>W2</i>	77 mol%	23 mol%

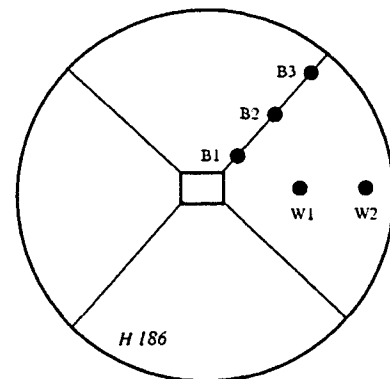


Fig. 50: Positions of EDX measurements

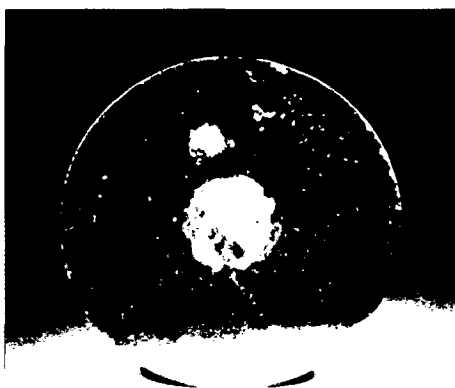


Fig. 51: Top surface of sample *H186*.

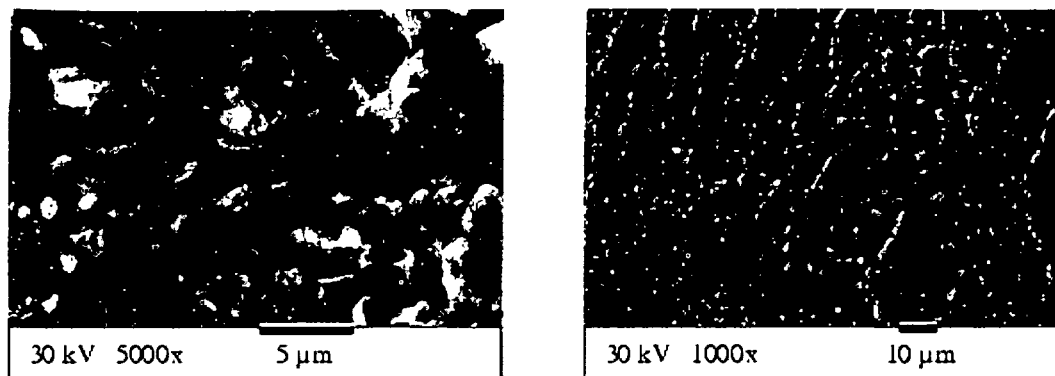


Fig. 52: Scanning electron micrographs of the surface of sample *H186* at an *a-a*-GSB [64].

In the course of the vertical assessment of the homogeneity of the sample, the thickness was reduced in ten steps from 10.90 mm to 5.60 mm. The mass of the remaining sample is 16.5 g. Images of the sample surfaces during the vertical assessment can be found in 6 *Discussion*.

Table 7: YBCO bulk superconductor from ZfW Göttingen

sample code	H186
mass	30.05 g
thickness	10.90 mm
diameter	25.75 mm
received on	10 02 2001
	unirr
status	reduced in thickness
	ATI Vienna

3.5 Samples from IRC Cambridge

3.5.1 Multi-seeded-melt-grown samples

A series of MSMG samples manufactured at the IRC Cambridge was investigated. It consists of four big cylindrical monoliths *MS-1*, *MS-2*, *MS-3* and *MS-4* ($\varnothing \approx 31$ mm, $h \approx 15$ mm) and a ring-shaped sample *R1* (with an inner diameter of 21.6 mm and an outer diameter of 31 mm, $h \approx 11.9$ mm). The specifications of the samples can be found in Table 8. Commercially available $\text{YBa}_2\text{Cu}_3\text{O}_{7-\delta}$ and Y_2BaCuO_5 powders (Nexans SuperConductors GmbH) with a purity of 99.9% were used for all samples. The precursor starting composition of all samples was 70 wt.% $\text{YBa}_2\text{Cu}_3\text{O}_{7-\delta}$ + 30 wt.% Y_2BaCuO_5 + 0.15 wt.% Pt. The powders were mixed and pressed into pellets.

Details of the fabrication of *R1* can also be found in [67]. The pellet of *R1* was sintered at 930 °C for 12 h, afterwards a hole was drilled into it. Nd-123 crystals were used as seeds. The green pellets were placed onto an alumina plate with an intermediate layer of 50 wt.% Y_2O_3 + 50 wt.% Yb_2O_3 powder. This should avoid the formation of heterogeneous nuclei from the substrate. The precursor was heated to 1040 °C in 8 h, then the melt was cooled rapidly to the starting growth temperature of 1005 °C, where slow cooling to 970 °C with a rate of 0.5 °C/h started. The sample was oxygenated at 400 °C for 7 days.

Fig. 54 shows the annular sample *R1*, which consists of 10 grains. The Nd-123 seeds for this sample had a size of approximately 1 mm × 1 mm × 0.5 mm and were placed in nearly equal distances from each other on the top of the ring. A vertical analysis of the sample *R1* required the reduction of the sample thickness to 6.95 mm.

Table 8: MSMG $\text{YBa}_2\text{Cu}_3\text{O}_{7-\delta}$ bulk superconductors from IRC Cambridge

sample code	<i>MS-1</i>	<i>MS-2</i>	<i>MS-3</i>	<i>MS-4</i>	<i>R1</i>
number of seeds	3	4	2	2	10
mass	67.21 g	66.33 g	65.43 g	64.55 g	31.27 g
thickness	15.4 mm	15.4 mm	15.0 mm	15.0 mm	11.9 mm
diameter	30.8 mm	30.5 mm	30.8 mm	30.6 mm	31.0 mm 21.6mm
received on	17 10 2003	17 10 2003	13 04 2004	13 04 2004	17 10 2003
status	unirr ATI Vienna				

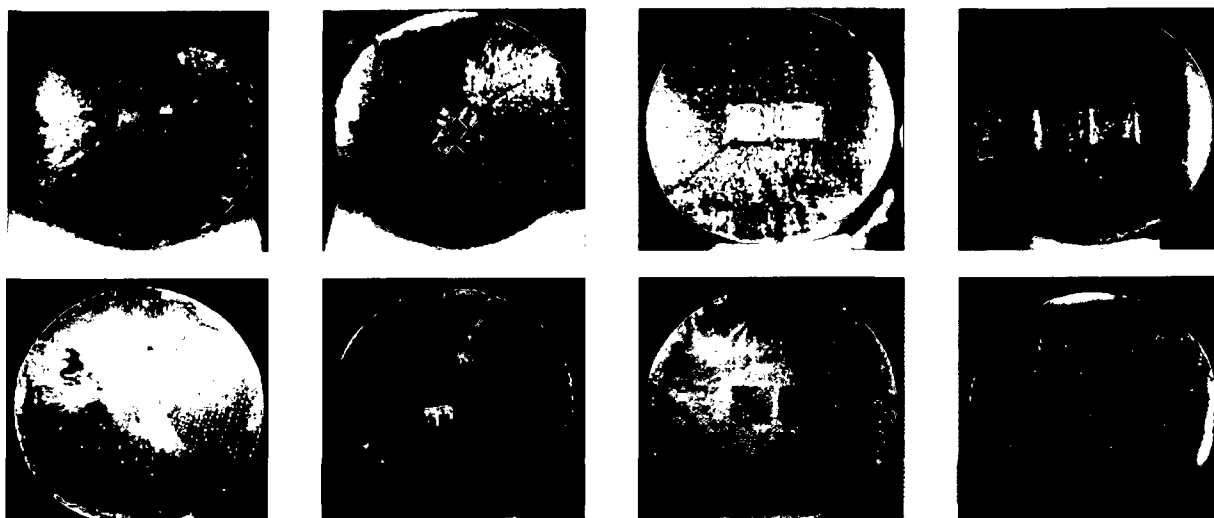


Fig. 53: Samples *MS-1*, *MS-2*, *MS-3* and *MS-4* before and after polishing the sample surface

For samples *MS-1* and *MS-2*, $\text{SmBa}_2\text{Cu}_3\text{O}_{7.8}$ seeds were used. Therefore, a precursor pellet with starting composition of 70 wt.% Sm-123 + 30 wt.% Sm-211 was prepared. MgO seeds were used for the TSMG process. The pellets were placed onto an alumina plate with an intermediate layer of Sm_2O_3 powder. The pellet was heated to 1100 °C in 3h. After a holding time of 1 h, the melt was cooled first rapidly to 1060 °C and then slowly to 1030 °C. The orientation of the *c*-axis of the monodomain $\text{SmBa}_2\text{Cu}_3\text{O}_{7.8}$ sample was unknown at first. Small seed specimens with a size of 1.5 mm × 1.5 mm × 2.0 mm were cut from the bulk. Investigation by optical microscopy showed that the crystallographic *a-b* plane was approximately 45° inclined to the basal plane of the seed cuboid, which is schematically drawn in Fig. 55. The TSMG process parameters (heating profile, oxygenation) of sample *MS-1* and *MS-2* with the grown Sm-123 seed crystals are very similar to those for sample *R1*.

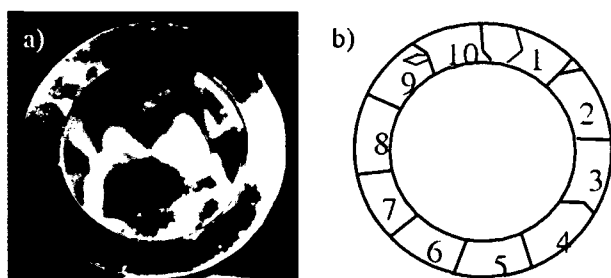


Fig. 54: a) Photograph of the top side of sample *R1*.

b) Schematic diagram of the ten different grains of *R1*.

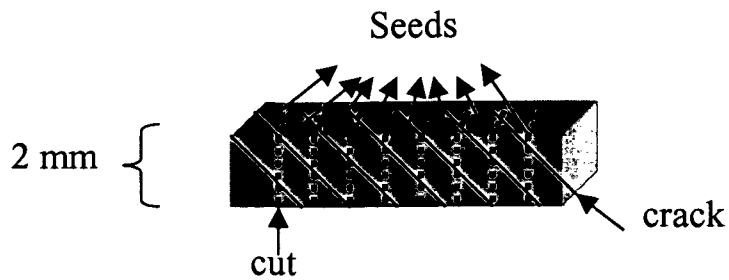


Fig. 55: Orientation of the crystallographic a - b -plane (crack) of the seeds for samples $MS-1$ and $MS-2$ [68].

For samples $MS-3$ and $MS-4$ two Nd-123 crystals with the same dimension were used as seeds. Therefore, the contact area for both seeds (now the a - b plane of the seeds) was the same. The distance between the seeds was about 0.6 mm. Much attention was paid to the parallel alignment of a and b axes of both seeds.

After growing $MS-3$, the same two seeds were used to grow $MS-4$, but now the distance between the seeds was about 0.8 mm. In addition there was a slight misalignment between the a - b directions of the seed crystals in the contact plane.

3.6 Samples from ICMAB Barcelona

In order to test the newly developed magnetoscan technique, small joined $\text{YBa}_2\text{Cu}_3\text{O}_{7-\delta}$ samples were investigated as well. Joining is, like multi-seeding, a technical way to fabricate large bulk superconductors with complex shape. It can be assumed that the fabrication process is similar to that cited in [69], where $\text{YBa}_2\text{Cu}_3\text{O}_{7-\delta}$ monoliths with 30 wt.% Y_2BaCuO_5 were grown using Nd-123 seeds. Ag was used as a welding agent to fabricate YBCO/Ag/YBCO joints.

Table 9: Ag-joined $\text{YBa}_2\text{Cu}_3\text{O}_{7-\delta}$ samples from ICMAB Barcelona

sample code	SLY-65-22t	SLY-14-14f d2t
mass	1.401 g	1.570 g
thickness	5.60 mm	2.50 mm
a × b	7.70 × 7.20 mm	9.50 × 11.50 mm
received on	17 10 2003	17 10 2003
status	will be sent back to ICMAB	

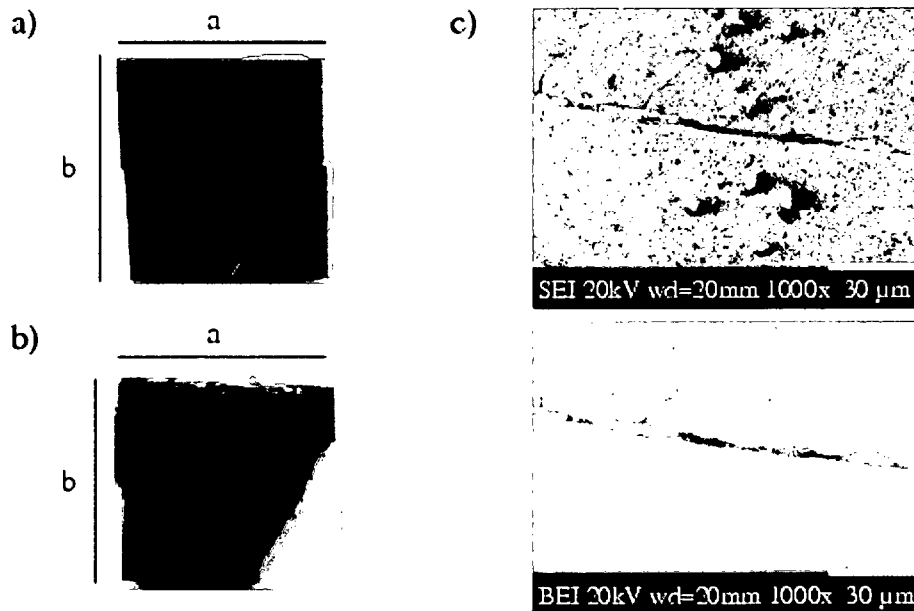


Fig. 56: a) Sample *SLY-14-14f d2t*, and b) sample *SLY-65-22t*. c) Scanning electron micrograph of the joint area of sample *SLY-14-14f d2t*.

EXPERIMENTAL METHODS

Hall probe scans of trapped fields provide a simple non destructive method for investigating the homogeneity of bulk superconductors. Experimental details of this method have already been widely discussed [65, 70]; they are summarized in the next section. In addition the so called magnetoscan technique will be described. With the help of this technique, interesting aspects of the homogeneity of a bulk monolith are obtained. Combined with microstructural investigations, such as optical microscopy and scanning electron microscopy, an interpretation of the results can be achieved.

4.1 Hall probe measurements

4.1.1 Principles

Hall probes are useful devices for measuring magnetic fields. They are based on the Hall effect, which was discovered by E. F. Hall in 1879. The principles of this effect are very simple [71]: a magnetic field exerts a force on the charge carriers of an electric current, the Lorentz force $\mathbf{J} \times \mathbf{B}$, which is directed perpendicular to the plane of \mathbf{J} and \mathbf{B} . A charge builds up at the sides of the conductor and results in a Hall voltage U_H , which increases linearly with increasing magnetic field. If the Hall probe is supplied with a constant control current, the measurement of the output voltage provides directly information on the magnetic induction \mathbf{B} . Hall probes are usually made of thin semiconductor layers. Using these sensors in a cryogenic environment, we have to ensure, that temperature dependence on the sensitivity is known. Special Hall probes were bought from AREPOC Ltd. in Bratislava.



Fig. 57: Hall probe of the type HHP-SF with uncovered active area [72].

For example, the Hall probe used for trapped field measurements was of the type HHP-SF, which operates in the temperature range from 1.5 K – 350 K and in magnetic fields of up to $\mu_0 H = 5$ T. The semiconductor surface of the Hall probe is not covered, which allows a very small gap between the probe and the surface of the superconductor down to 150 μm . This is desirable, because a reduction of the gap enhances the spatial resolution. Around the sensor system a resin enclosure protects the Hall probe against accidental contacts with a sample. Another advantage is the small size of the active area, which is in the case of the HHP-SF model 20 $\mu\text{m} \times 20$ μm . Fig. 57 shows the Hall probe schematically.

In order to obtain the proportionality factor between the output voltage and the magnetic induction, it is necessary to calibrate the sensor in a well-known magnetic field. This can be done in a cryostat, where the temperature is adjustable around 77 K. This is a reasonable temperature value for liquid nitrogen. The calibration of the Hall probe HHP-SF-301 was already performed by R. González Arrabal [65] and the proportionality factor is 22.22 $\text{T}\cdot\text{V}^{-1}$.

4.1.2 Experimental arrangement

The superconducting samples were magnetized in an 8 T magnet or in a 1.4 T electromagnet in the zero field cooled (zfc) or the field cooled mode (fc). To measure the spatial distribution of the flux density, the Hall probe was inserted into a hole of an acrylic glass cylinder, which was mounted on an x - y sledge. It can be lifted and lowered in the z -direction. A fixed sliding caliper was used to determine the position of the Hall probe above the sample surface. Thus a regulation of the gap between the sensor and the sample was possible. The sample was mounted on a sample holder and fixed with vacuum grease. The sample holder is placed into the liquid nitrogen bath. The setup is shown in Fig. 58. The positioning of the x - y sledge was

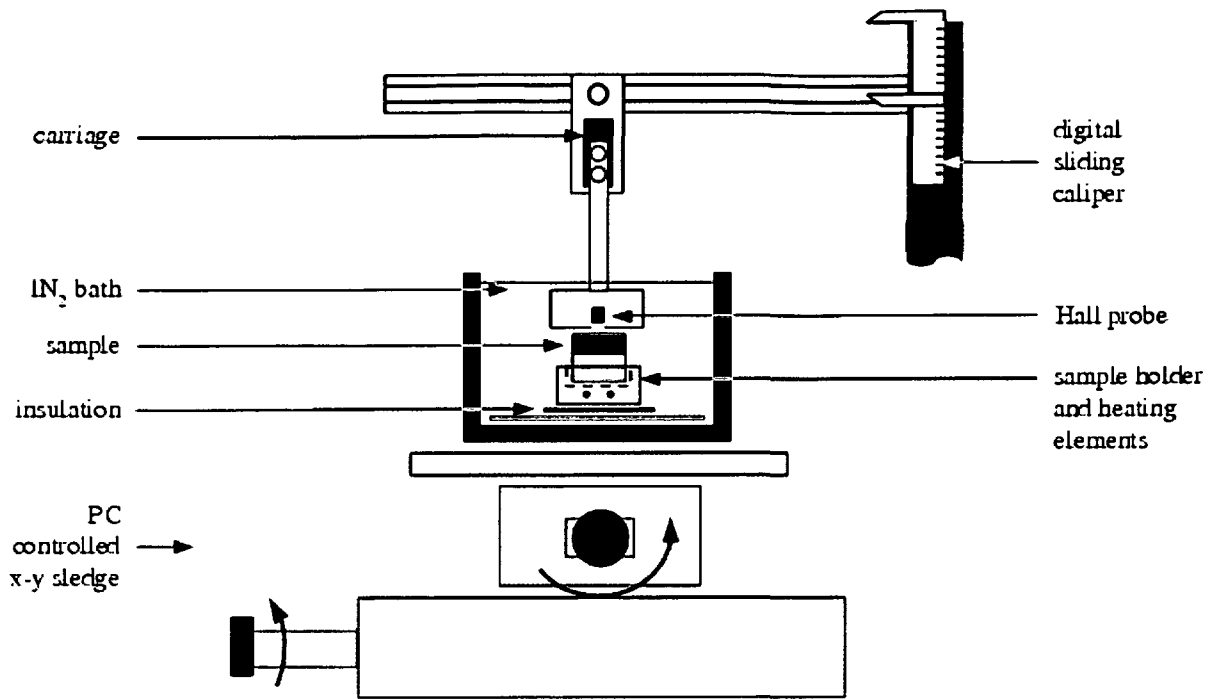


Fig. 58: Experimental setup of the trapped field measurements.

computer controlled via a MPK-3 control card. A Lakeshore constant current source supplied the Hall probe with a constant control current. The Hall voltage of the Hall probe is read by a Keithley DMM. Two important points should be added. First, mounting the rod with the Hall probe on a skid should avoid accidental damage of the Hall probe. When the acrylic glass touches the sample surface, no pressure on the sample would be exerted, because the carriage will lift the rod with the Hall probe. Second, two heating elements below the sample holder and a cover tool were used to warm up the sample carefully to room temperature. This was necessary, since the samples were measured several times and, therefore, had to survive several thermal cycles. Fig. 59 shows an example of crack formation, which happened due the enormous thermal stresses, when the sample was taken out of the liquid nitrogen abruptly. The bottom side of this sample had to be grinded to obtain coplanar alignment between top and bottom surfaces again. Crack formation between the individual measurements disturb the

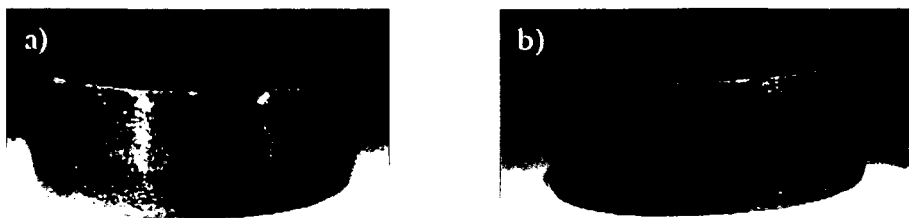


Fig. 59: Sample *Li0at5* a) before the thermal cycle and b) after it was taken out from liquid nitrogen.

investigation of the growth-related inhomogeneities massively and are to be avoided.

4.1.3 Experimental parameters for trapped field measurements

Several factors influence Hall scans of the remnant flux. These factors were already discussed in the previous work by R. González Arrabal [65]. Nevertheless, it should be noted, that the temperature of the liquid nitrogen bath is an important parameter which influences the value of the trapped field. Therefore, the temperature of the liquid nitrogen bath was recorded by a PT-100 before and after each scan. Another important parameter is the time between the activation of the sample and the start of the measurement. In order to avoid relaxation dependent drifts, we started the scans 15 minutes after activation. An often unnoted factor is the sweep rate of the external magnetic field during the activation of the sample. The sweep rate was 0.37 T/min up to $\mu_0 H = 0.1$ T and subsequently 1.48 T/min at higher fields. For activation fields of $\mu_0 H = 0.1$ T or $\mu_0 H = 0.2$ T, the sweep rate often remained unchanged. Already mentioned were the resolution determining factors of the Hall scan. They are the size of the active area of the Hall probe, the distance between Hall probe and sample surface during the scan (“gap”) and the grid size of the data points. Table 10 summarizes the standard parameters for the conventional Hall scans.

Table 10: Standard parameters for conventional Hall scans

Technical	
Hall probe	<i>AREPOC HHP-SF-301</i>
active area	<i>20 μm \times 20 μm</i>
Activation	
sweep rate	<i>1.48 T/min</i>
start after activation	<i>15 min</i>
Scan	
scan grid	<i>0.25 mm \times 0.25 mm</i>
gap	<i>0.2 mm</i>
temperature control	<i>before and after measurement</i>

4.1.4 Bean model and radial assessment of bulk superconductors

Conventional Hall scans are performed typically on a fully activated sample (expected saturation at $2H^*$). The experiments showed, however, that more detailed information on

sample inhomogeneities can be obtained, when the sample is only partially penetrated, rather than fully magnetized. When the activation field is increased sequentially in the zero field cooled (zfc) mode and the trapped field is measured, the flux penetration into the sample occurs stepwise and the bulk properties, which may vary in radial direction, can be detected. Fig. 60 illustrates the penetration of the magnetic flux with increasing activation field according to the Bean model.

In 1962 C. P. Bean introduced the critical state model to explain the magnetization of hysteretic type-II superconductors [1-2]. In this model the following assumptions are made: *i*) the superconductor has the shape of an infinitely long slab; *ii*) the current density J_C is independent of the field. The result is a field dependent penetration into the superconductor.

Applying Maxwell's equation $\nabla \times \mathbf{H}$ in cylindrical coordinates and assuming a circumferential current $\mathbf{J} = J_C \mathbf{e}_\phi$ and a vertical magnetic field $\mathbf{H} = H_z \mathbf{e}_z$, the rotor reduces to

$$\frac{\partial H_z}{\partial r} = J_C. \quad (8)$$

Generally, the critical current density $J_C(H)$ is field dependent. In Bean's model $J_C(H) = J_C = \text{const.}$ is assumed. The geometrical interpretation of the above equation is then a constant gradient of the field inside the superconductor. At an activation field of H^* , we get by integration

$$H^* = J_C R, \quad (9)$$

with R the radius of the cylindrical superconductor.

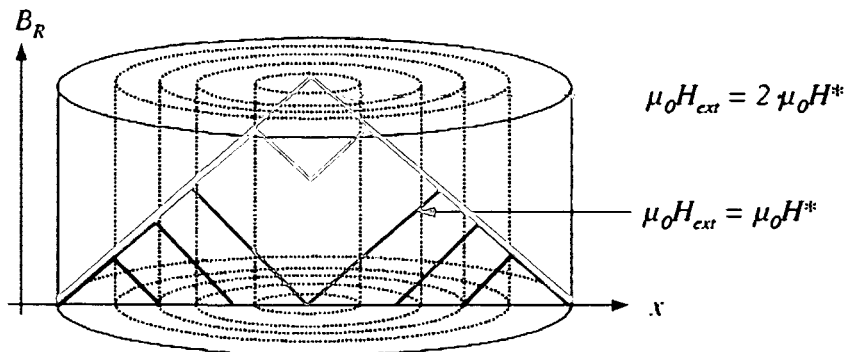


Fig. 60: Sequential flux penetration into the bulk cylinder. According to the Bean model, in the zfc mode the two fronts of the remnant field inside the sample collide when the activation field reaches $\mu_0 H^*$.

4.2 Magnetoscan

4.2.1 Principles

A qualitative description of the magnetoscan technique was published in [10]. In an initial experiment the top surface of a superconducting bulk sample was “touched” by a small permanent magnet, i.e. the magnet was moved vertically into the liquid nitrogen to the surface of the superconductor and was removed again. Then the sample was scanned by a conventional Hall scan. This deviates from the usual procedure, i.e. the sample is not exposed to a homogeneous magnetic field anymore, but only a small part of the sample “feels” the small magnet. The result of this Hall scan is shown in Fig. 61a, where the positions of the magnet and the sample are indicated by circles. It was observed that the magnetic flux remained trapped in the sample only at the edge of the magnet. Also the change in the direction of the magnetic field lines is strongest there. A closer look shows that the pattern is not radially symmetric. This indicates, that the flux penetration is a local sample property. Fig. 61b shows a Hall scan of the sample after having “scanned” the whole sample surface with the permanent magnet previously. This means, that the magnet was moved in the same way above the sample as the Hall probe in a Hall scan. The flux is only trapped at the edge of the sample, which means that no hysteretic effects occur during the magnetoscan.

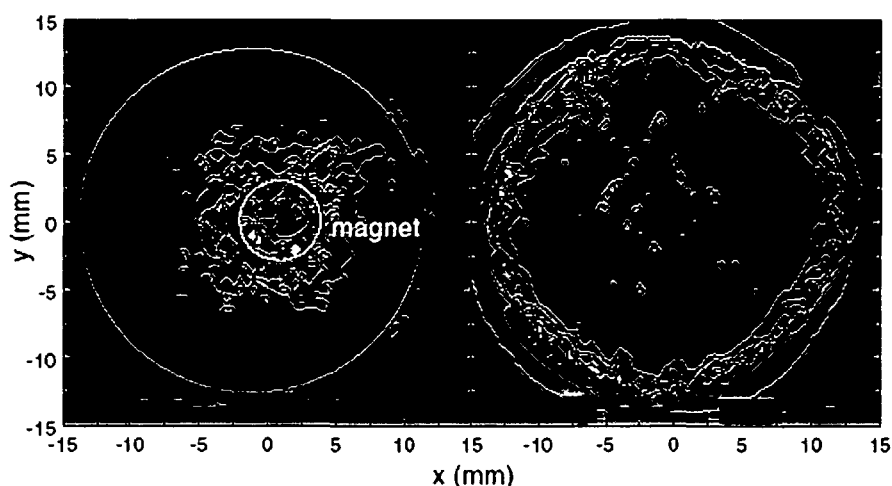


Fig. 61: a) Trapped flux profile after touching the surface of the superconductor with a permanent magnet. The size of the magnet is indicated by the white circle. The sample size is indicated by the black circle. b) Remnant flux in the sample after a complete magnetoscan, measured by a conventional Hall scan. A typical signal range is given, too [10].

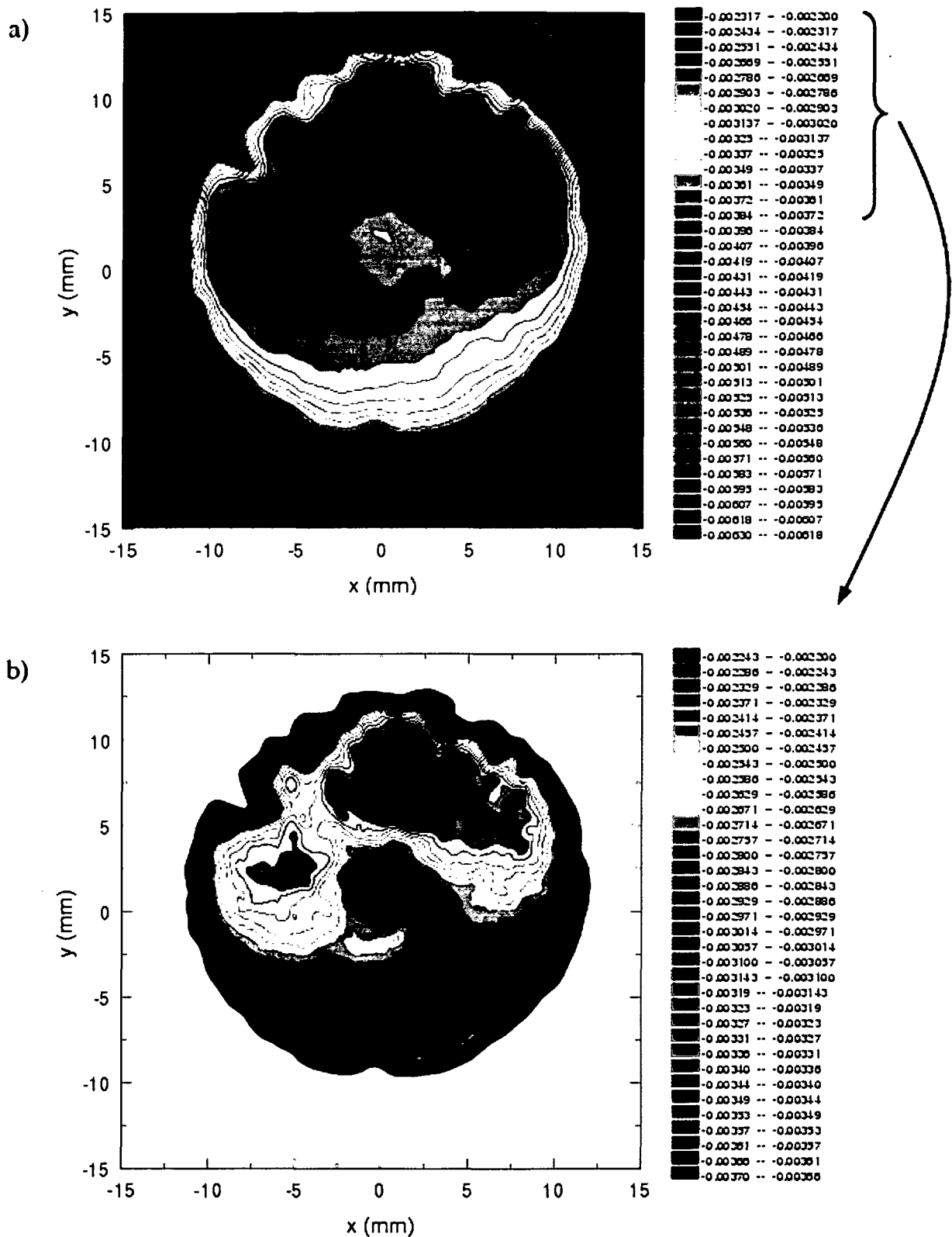


Fig. 62: One of the first results of the magnetoscan (sample *H186*): a) whole signal range and b) zoomed into the high response range.

The permanent magnet used for the magnetoscan has a magnetic induction of $\mu_0 H = 80$ mT. Assuming a critical current density of 10^8 Am⁻², the estimated penetration depth δ of the

magnetic field is about 1 mm. This means, that the shielding currents are flowing in a surface layer of 1 mm. The new technique called magnetoscan involves scanning the surface of the superconductor simultaneously with a Hall probe and a permanent magnet. First experiments with the active area of the Hall probe positioned in the center of the magnet resulted in only a small signal variation. A much better resolution was obtained, when the active area was positioned at the edge of the magnet. Initial magnetoscan results are shown in Fig. 62. However, with this arrangement an asymmetry was obtained. Because the voltage of the Hall probe is always stored during the movement in positive y -direction, first the magnet and then the Hall probe are moved above the surface of the sample. This can be seen in the slight shift of the signal to lower values compared with the background (no sample) at the front edge (as seen during scanning). There, the magnetic field is shielded by the sample and one can expect that the field lines are pushed backwards (dark blue). At the back edge of the sample the signal is shifted to higher values compared to the background (light blue). One can imagine that in this case the field lines are entailed by the magnet (turquoise). However, massive shielding can be found right above the sample (red). If one zooms into the upper part of the scale, a strongly position dependent signal becomes visible. It can be assumed, that regions with better shielding properties show a high response, regions with lower shielding properties show a smaller response, which is understood qualitatively, if one assumes that in these regions the magnetic flux penetrates more easily.

4.2.2 Magnetoscan Setup

The setup of the magnetoscan contains a permanent magnet in addition to the Hall probe. The Hall probe is mounted with varnish under the magnet in such a way, that the position of the active area coincides with the edge of the permanent magnet. Hall probe and permanent magnet scan the sample surface simultaneously. The setup is shown schematically in Fig. 63a. Fig. 63b shows a photograph of the part made of acrylic glass, in which the magnet and the Hall probe are inserted. For the standard setup, the Hall probe AREPOC HHP-VPO-48 was used because of its flat geometry. After damaging the probe in September 2004, it was replaced by AREPOC HHP-VU-492, which has the same geometry. The size of the active area is $50 \mu\text{m} \times 50 \mu\text{m}$. A picture of the Hall probe is shown in Fig. 63c.

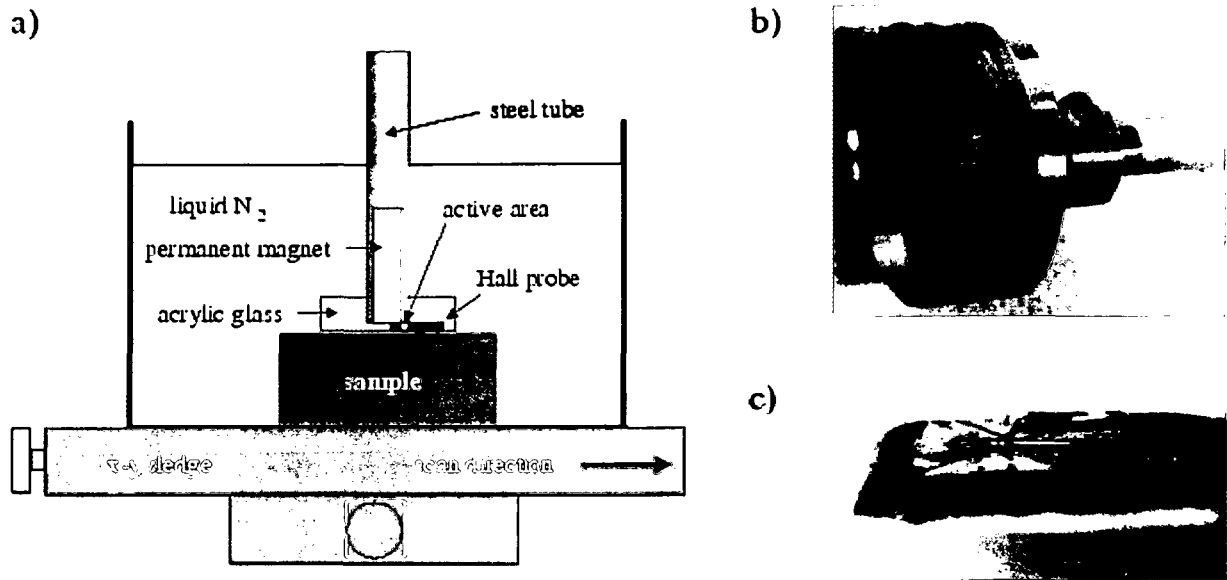


Fig. 63: a) Setup of the magnetoscan facility. b) Acrylic glass with mounted Hall probe and magnet. c) Hall probe HHP-VPO-48.

4.2.3 Experimental parameters for the magnetoscan

The main problem of the magnetoscan technique is the exact alignment of the sample surface parallel to the plane in which the Hall probe moves. As it can be seen already in Fig. 62, there is a slight drift of the signal over the whole sample, which is due to a varying distance between sample surface and Hall probe. To solve the problem, the bottom side of the samples often had to be grinded to obtain a sample with exactly equal thickness. The standard parameters can be found in Table 11.

Table 11: Standard parameters for the magnetoscan.

Hall probe	
Hall probe	AREPOC HHP-VPO-48 AREPOC HHP-VU-492 (since 09 2004)
active area	50 μm \times 50 μm
magnet	
induction	80 mT
dimensions	$\varnothing = 6 \text{ mm}$, $h = 18 \text{ mm}$
scan	
scan grid	0.25 mm \times 0.25 mm
gap	0.2 mm
temperature control	before and after measurement

4.2.4 More tests of the new technique

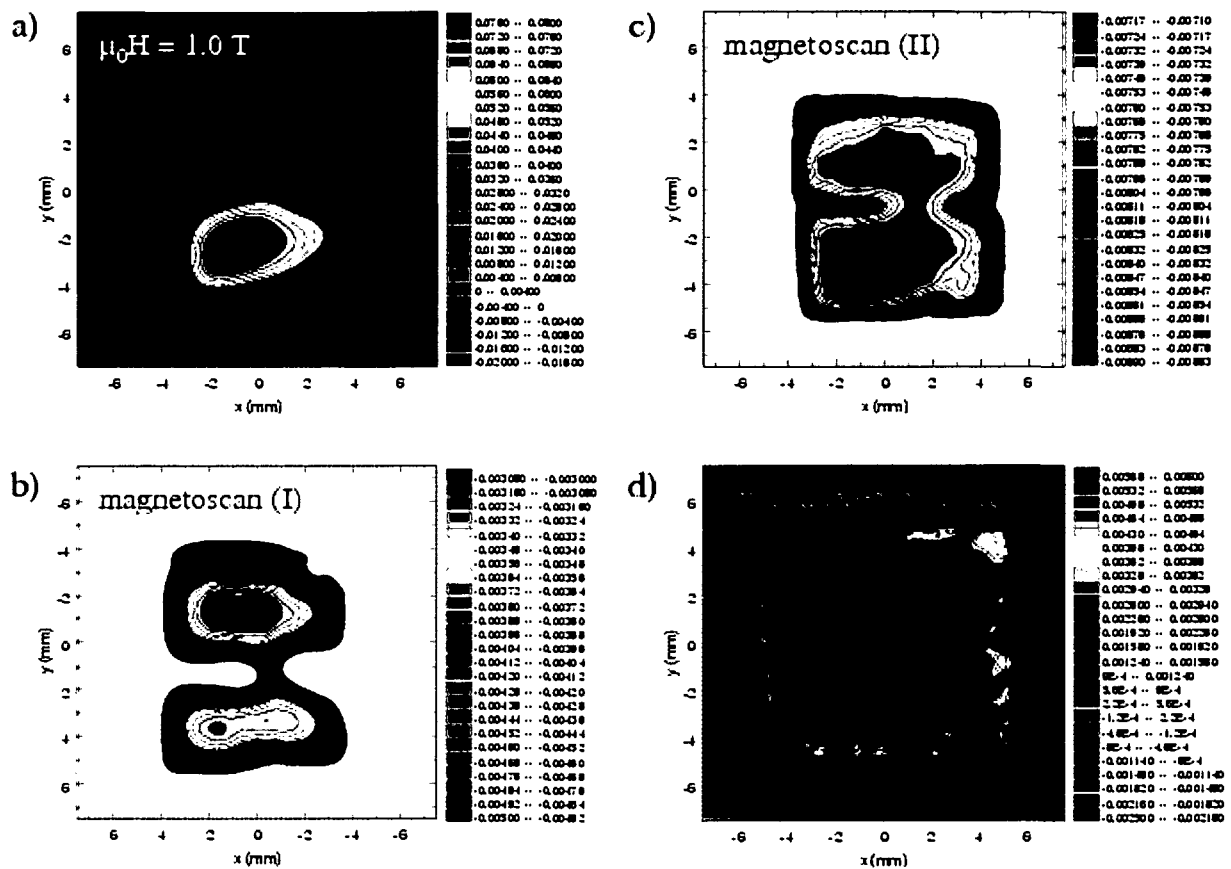


Fig. 64: Sample *SLY14-14f-d2t* a) Conventional Hall scan after activation at $\mu_0 H = 1.0 \text{ T}$. b) Magnetoscan (I) with parameters of the magnet: $B = 80 \text{ mT}$, $\varnothing = 6 \text{ mm}$. c) Magnetoscan (II) with changed configuration: $B = 100 \text{ mT}$, $\varnothing = 3 \text{ mm}$. d) Conventional Hall scan after the magnetoscan (II). Scales for the conventional Hall scans are in Tesla, scales for the magnetoscans are in Volt.

To test the magnetoscan, a very thin joined bulk superconductor (*SLY14-14f-d2t*) was investigated. Fig. 64 summarizes the comparison between a conventional Hall scan and the magnetoscan. Moreover, the configurational parameters of the magnetoscan were changed. First, a conventional field scan was performed. The maximal trapped field of this sample is not very high, 79.3 mT. The region of the weld is, however, well visible. When the magnetoscan was performed on the same sample, the shielding behaviour did not show many details, except a sharp decrease at the welding zone. This can be explained by the small thickness of the sample. A similar result was obtained, when the size of the magnet and also its induction were changed (denoted by “magnetoscan (II)”). The main difference is caused by the smaller size of the magnet, leading to a “sharper” signal, i.e. a better spatial resolution, especially at the edge of the sample. The shape of the sample is much better mapped by

magnetoscan (II) than by magnetoscan (I). After the magnetoscan (II) another Hall scan was performed, which shows that most of the flux is trapped at the edge of the sample and along the weld.

It should be pointed out, that an improvement of the spatial resolution can be obtained by smaller magnet diameters. The technical problem however is the measurement of the small signal variations. Efforts to improve of the technique were not yet successful.

Table 12: Parameters of the measurements shown in Fig. 64.

	<i>Hall scan 1T zfc</i>	<i>Magnetoscan (I)</i>	<i>Magnetoscan (II)</i>	<i>Hallscan after Magnetoscan (II)</i>
magnet induction	-	80 mT	100 mT	-
Hall probe	HHP SF 301	HHP VPO 48	HHP VC 397	HHP SF 301
active area	20 μm \times 20 μm	50 μm \times 50 μm	50 μm \times 50 μm	20 μm \times 20 μm
gap	0.2 mm	0.2 mm	0.2 mm	0.2 mm
grid size	0.25 mm \times 0.25 mm	0.25 mm \times 0.25 mm	0.20 mm \times 0.20 mm	0.25 mm \times 0.25 mm
temperature control	77.92 K	77.75 K	77.75 K	78.47 K

4.3 VSM Measurements

Critical currents of several small reference samples were measured in a vibrating sample magnetometer (VSM). In a VSM the magnetic moment of the sample is measured by vibrating the sample inside a pick up coil system, which contains 8 small coils. The physical principle of this device is the induction law, where the voltage U and the magnetic flux ϕ are related via

$$U = -\frac{d\phi}{dt}. \quad (10)$$

The VSM used in this work was manufactured by Oxford Instruments. A variable temperature facility allows to adjust temperatures in the range from 1.6 K to 350 K. The measured output voltage is proportional to the magnetic moment m of the sample. The $m(H)$ -curves were evaluated employing the Bean model to obtain the critical current densities $J_C(H)$. The magnetic moment is evaluated from the upper, $m(H^+)$, and lower, $m(H^-)$, branch of the hysteresis loop:

$$m(H) = \frac{m(H^+) - m(H^-)}{2}. \quad (11)$$

With the sample volume $V = a \times b \times c$, the critical current density $J_C(H)$ is obtained:

$$J_C(H) = \frac{|m(H)|}{V} \cdot \frac{4}{b \left(1 - \frac{b}{3a}\right)}, \quad (12)$$

where the second part of the formula is a geometry dependent factor. In the case of cylindrical samples, $a = b = \pi^{0.5} \cdot r$.

4.4 Microstructural investigation: XRD of powders, scanning electron microscopy and optical microscopy

Additional experimental methods were used to investigate the microstructure of the samples.

Powder X-ray diffraction was performed at TU Vienna by M. Müller. The experimental parameters are given in the table below. In the course of the vertical homogeneity assessment of some samples, the powders of each grinding step were analyzed. The strongest peaks of the Y-123 and the Y-211 phase were related to estimate the overall Y-211 content. The peaks were evaluated with the help of a database [46]. A typical result is shown in Fig. 65.

In addition, a scanning electron microscope JEOL JSM 5410 at TU Vienna was used. It was equipped with an X-ray Si(Li)-detector, and the signals were evaluated analytically using the software RÖNTEC.

Finally, an optical microscope was used, “universal camera microscope” ME-F, Reichert. It is equipped with a polarizer/analyzer system. An adapter was prepared for the OLYMPUS mirror reflection camera.

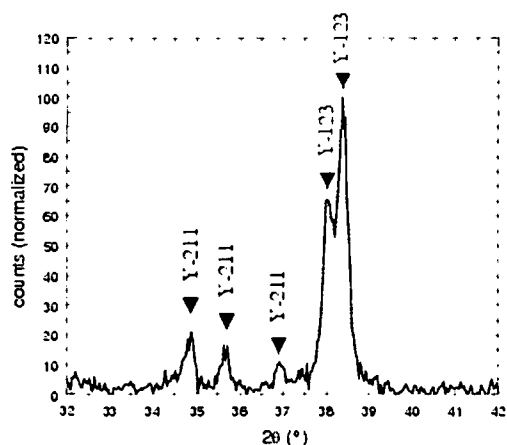


Fig. 65: Typical result of a powder diffraction pattern of “YBCO”.

Peaks of the Y-123 and the Y-211 phase are indicated.

Table 13: Parameters for the X-ray powder diffraction [73].

X-ray tube	Cobalt	wavelength $\lambda(K_{\alpha 1})$	1.78892 Å
geometry	Bragg Brentano	2θ interval	[20°, 80°]
Voltage	30 kV	increment $\Delta(2\theta)$	0.04°
Current	35 mA	measurement duration	10 s

5 NEUTRON IRRADIATION

5.1 Calculation of the activity

Calculations of the neutron activation of $\text{YBa}_2\text{Cu}_3\text{O}_{7.8}$ bulk samples require detailed information on the composition and mass of the sample. The expected activity A (given in MBq) of the sample as a function of time is

$$A = 3.7 \cdot 10^5 \cdot 0.6 \cdot m \cdot A_S \cdot (1 - e^{-0.693 \Delta/T}) \cdot e^{-0.693 t/T}. \quad (13)$$

Published standard tables of the saturation activity A_S and the half lives T of the elements can be found in [74]. Δ is the exposure time of the sample to radiation, and is determined by the

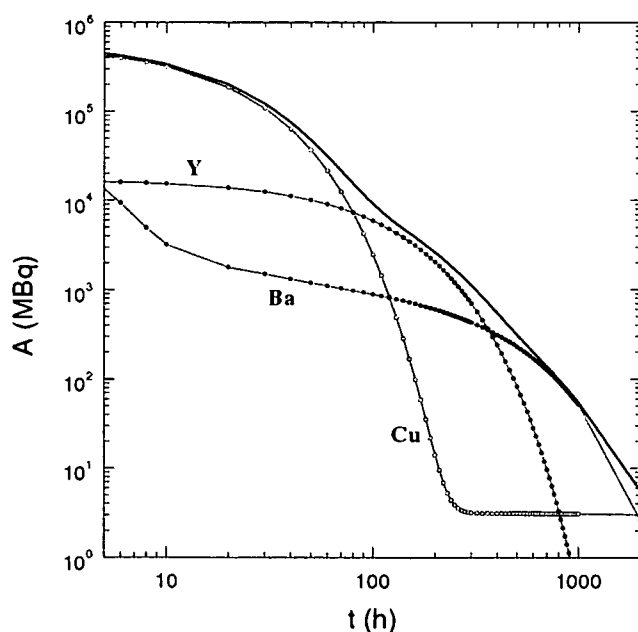


Fig. 66: Calculation of the activity of $\text{YBa}_2\text{Cu}_3\text{O}_{7.8}$ (with a mass of 35 g and at a fluence of $2 \cdot 10^{21} \text{ m}^{-2}$)

flux density of the TRIGA MARK II reactor and the fluence. The value $\Delta = 7\text{ h } 19\text{ m}$ for a fluence of $2 \cdot 10^{21} \text{ m}^{-2}$ was used. The nuclides of Y, Ba and Cu have half lifes of a few hours or days and do not show extremely high saturation activities, i.e. the expected high activity is due to the large mass of the bulk superconductor.

5.2 Neutron Irradiation of $\text{YBa}_2\text{Cu}_3\text{O}_{7-\delta}$ bulk samples

Two $\text{YBa}_2\text{Cu}_3\text{O}_{7-\delta}$ bulk samples were irradiated. Because of the damage of sample *Np-6*, a second irradiation experiment was necessary. Simultaneously with the irradiation of sample *Np-11*, a Ni foil ($m = 820 \text{ }\mu\text{g}$) was exposed to the same fluence. The irradiation-related data is shown in Table 14. When the sample was measured again after irradiation, its dose was below $100 \text{ }\mu\text{Sv/h}$.

Table 14: Irradiation data of bulk $\text{YBa}_2\text{Cu}_3\text{O}_{7-\delta}$ samples at the TRIGA MARK II reactor in Vienna

date	sample	position	fluence	exposure time	nuclides
02 01 2004	<i>Np-6</i>	ZBR	$2 \cdot 10^{21} \text{ m}^{-2}$	7 h 19 m	$^{90}\text{Y}, ^{131}\text{Ba}, ^{133}\text{Ba}, ^{131}\text{Cs}, ^{64}\text{Cu}$
14 07 2004	<i>Np-11</i>	ZBR	$2 \cdot 10^{21} \text{ m}^{-2}$	7 h 19 m	

5.3 Neutron Irradiation of Li doped $\text{YBa}_2\text{Cu}_3\text{O}_{7-\delta}$

Lithium consists of two naturally occurring isotopes: ^6Li (7.6 %) and ^7Li (92.4 %). ^6Li has a large thermal neutron absorption cross section ($\sigma = 950 \text{ barns}$, [74]). The nuclear reaction leads to α -particles and ^3H according to



Tritium, ^3H , is radioactive with a half life of 12.26 years. Irradiation of lithium doped YBCO produces columnar defects with a length of $25 \text{ }\mu\text{m}$. Because of the homogeneous distribution of Li in the material, the columnar defects are homogeneously distributed as well.

Table 15: Irradiation data of bulk Li-doped $\text{YBa}_2\text{Cu}_3\text{O}_{7.8}$ samples at the TRIGA MARK II reactor in Vienna

date	sample	position	fluence	exposure time	nuclides
02 01 2004	<i>Li0at6</i>	ZBR	$2 \cdot 10^{21} \text{ m}^{-2}$	7 h 19 m	$^{90}\text{Y}, ^{131}\text{Ba}, ^{133}\text{Ba}, ^{131}\text{Cs}, ^{64}\text{Cu}, ^3\text{H}$
14 07 2004	<i>Li0at6Nr2</i>	ZBR	$2 \cdot 10^{21} \text{ m}^{-2}$	7 h 19 m	

First results on low fluence neutron irradiation were obtained by Manton et al. [75]. Their precursor powder contained Y-123 + 10 mol% Y-211 + 1% LiHO. The fluence of thermal neutrons was 10^{17} cm^{-2} ($= 10^{21} \text{ m}^{-2}$). VSM measurements, carried out to determine the critical current density J_C before and after irradiation, showed that neutron irradiation of Li doped $\text{YBa}_2\text{Cu}_3\text{O}_{7.8}$ changed the magnitude and the field dependence of J_C . An improvement of flux pinning was achieved.

5.4 Neutron Irradiated Samples of this work

Neutron irradiations were performed at the TRIGA MARK-II reactor of the Atomic Institute in Vienna. All samples were sealed in a quartz tube, which was placed into an Al cylinder. It is important that the quartz tube is sealed correctly, because the Al cylinder is filled with the distilled water inside the reactor. The Al cylinder is then inserted into the central irradiation facility (ZBR) where the fast neutron flux density is $7.6 \cdot 10^{16} \text{ m}^{-2} \text{ s}^{-1}$ ($E > 0.1 \text{ MeV}$) at a power level of 250 kW (steady state). The neutron spectrum of the TRIGA MARK-II reactor in Vienna was published by Weber et al. [76].

In a first irradiation experiment, the Li-doped $\text{YBa}_2\text{Cu}_3\text{O}_{7.8}$ sample *Li0at6* was sealed together with the $\text{YBa}_2\text{Cu}_3\text{O}_{7.8}$ bulk sample *Np-6* in a quartz tube. Unfortunately the two samples were destroyed due to water leakage into the quartz tube. In a second irradiation experiment, a separate quartz tube was used for each sample. Simultaneously with the irradiation of sample *Li0at6Nr2*, a Ni foil ($m = 722 \mu\text{g}$) was exposed to the same fluence. When the sample was removed from the reactor (date: 17 12 2004), a liquid scintillation experiment was carried out to measure possible tritium emissions from the bulk, which yielded a tritium activity of 33.8 kBq [82], which requires special handling precautions due to tritium diffusion from the sample. The radiation dose was below $100 \mu\text{Sv/h}$. Table 15 shows the the important data of both Li-doped $\text{YBa}_2\text{Cu}_3\text{O}_{7.8}$ samples.

DISCUSSION

6.1 Radial homogeneity of TSMG bulk superconductors

6.1.1 Mapping of the growth sectors

A very impressive result obtained by the magnetoscan technique is the mapping of the growth sectors in the superconducting monolith. Scanning the surface of the bulk superconductor with a Hall probe and a small permanent magnet simultaneously, generally information as shown in Fig. 67a is obtained. A slightly different signal between *a*-GSs and *c*-GS can already be recognized there. Zooming into the upper range of the scale, we get the result shown in Fig. 67b. On this new scale, the depression of the signal (yellow and green) at the location of the *c*-GS becomes clearly visible, whereas the average signal is higher at the *a*-GSs due to a better shielding capability. The obvious depressions of the signal within the *a*-GSs are due to cracks. Maximal signals are observed near the *a*-*a*-GSB, which will be discussed in more

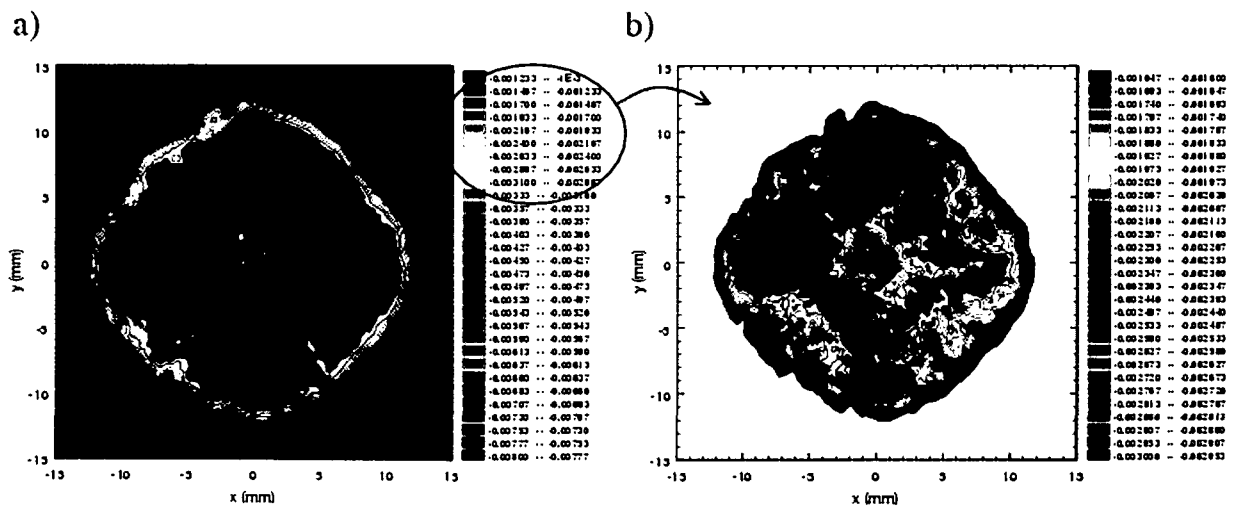


Fig. 67: Magnetoscan result on sample *Li0at6*. a) Full scale and b) zoomed into the upper part of the scale.

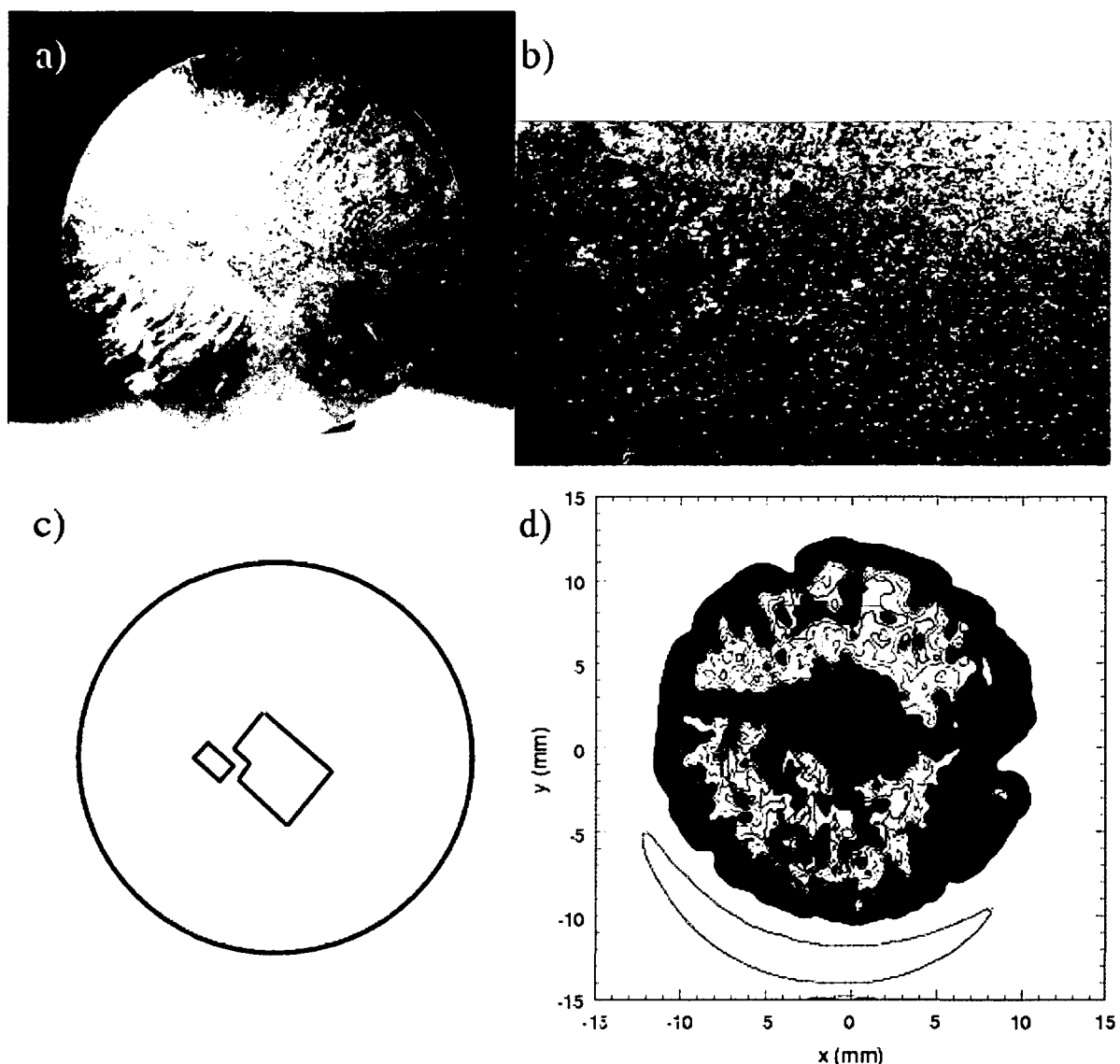


Fig. 68: Growth sector irregularity in sample *H186(s4)*. a) Photograph of the sample surface. b) Detail of the *c*-growth sectors. c) Schematic representation of the *c*-growth sectors. d) Magnetoscan.

detail in the next section. Fig. 68 shows an example of a *c*-growth sector irregularity. This was found after having removed 1.6 mm from the top of a $\text{YBa}_2\text{Cu}_3\text{O}_{7-\delta}$ bulk by grinding. The photograph of the sample surface shows that two neighboring *c*-growth sectors had been formed. The reason might be a broken seed, for example. The magnetoscan of the sample surface shows directly the two parts of the *c*-GS according to the schematic representation.

Fig. 69 shows localized inhomogeneities in the *a*- and *c*-GS of sample *Lip1*. The rectangular section of the *c*-GS is exactly mapped. The inhomogeneities, visible as signal suppressions, may be due to very fine cracks in the sample surface. Except for a slight drift in the signal, the *a*-GS shows a high signal (red) everywhere.

Mapping of the growth sectors in the *a*-*c* direction was successful as well. A $\text{YBa}_2\text{Cu}_3\text{O}_{7-\delta}$

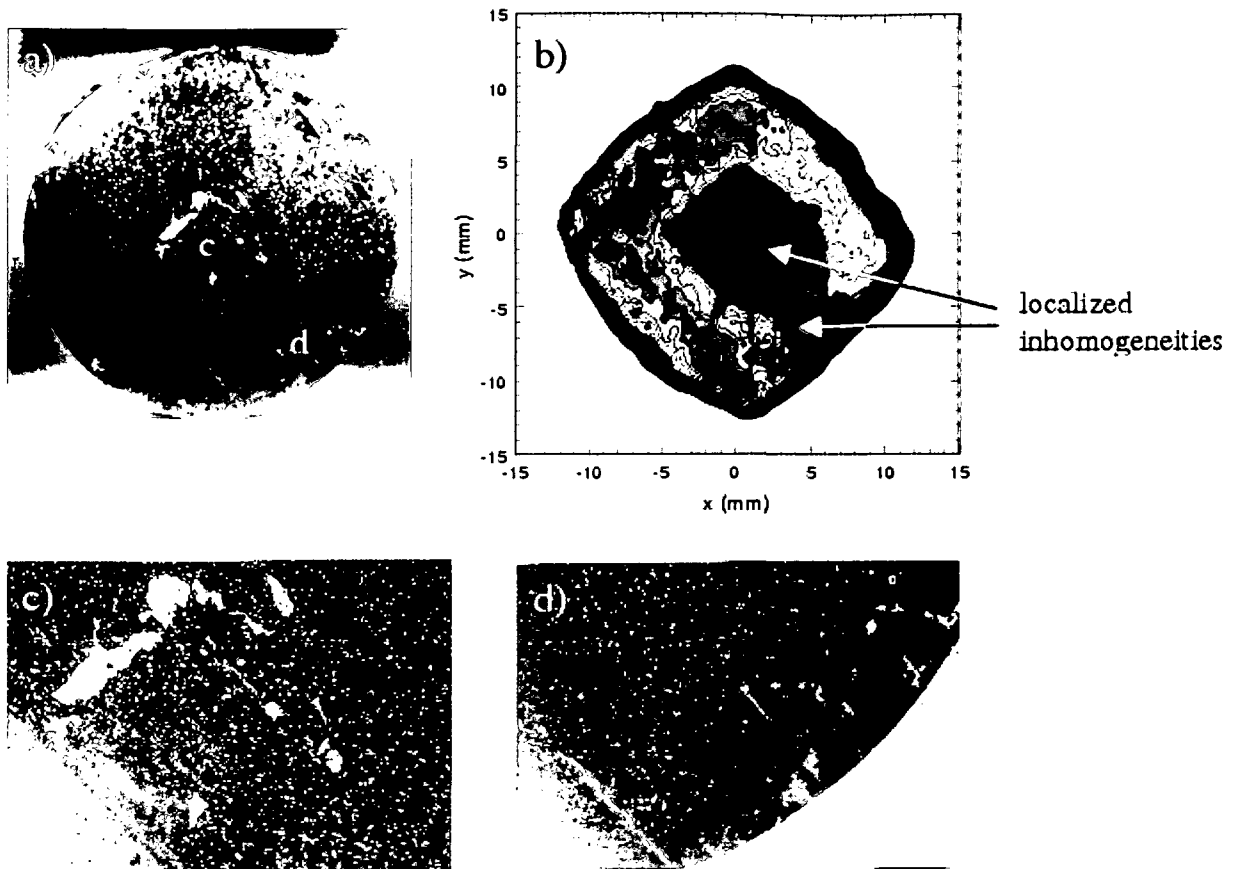


Fig. 69: a) Photo of top side of sample *Lip1*. b) Magnetoscan and c),d) magnification of the areas, where inhomogeneities were localized by the magnetoscan.

bulk sample (*NEXANS SLY-14-21*) was cut in vertical direction along the a - c plane. Fig. 70 shows the cross section of the sample. The c -GS can be distinguished from the a -GS by a difference in contrast. The scanning plane of the magnetoscan was now parallel to the a - c plane of the bulk monolith. The c -GS is directly visible (yellow and green) and related to the suppression of the shielding currents in this region. On the left and on the right from the c -GS,

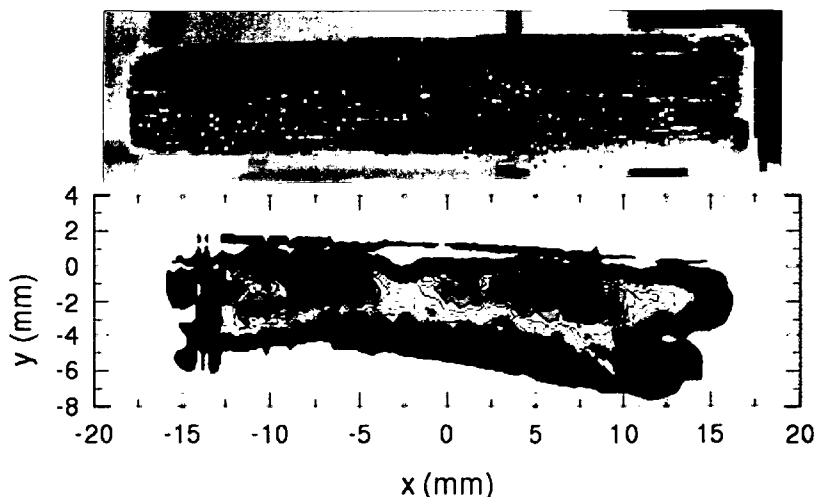


Fig. 70: Cross section of the sample and magnetoscan of the cross section.

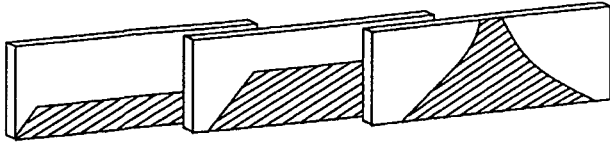


Fig. 71: Schematic diagram of *c*-GS (hatched area) development as found in sample *SLY-14-21*.

inside the *a*-GS, the shielding behavior is much higher (red). Other slices with increasing horizontal distance from the seed were investigated as well. The growth of the *c*-GS could be followed clearly by the mapping via the magnetoscan. Fig. 71 shows schematically the development of the vertical cuts of the *c*-GS as found experimentally (Fig.72) in sample *SLY-14-21*. With increasing vertical distance from the top, the *c*-GS becomes wider, whereas with increasing horizontal distance from the seed position, the *c*-GS becomes smaller. Similar experimental results on a superconducting monolith were obtained by Zeisberger et. al [11]. There the *a*-GSs showed also higher screening than the *c*-GS. As a result of a simulation, the measured fields in the *a*-GSs correspond to an “effective” critical current density of $2.6 \cdot 10^8 \text{ Am}^{-2}$, whereas the “effective” critical current density in the *c*-GS is estimated to be only 10^8 Am^{-2} .

Further results on the vertical distribution of the screening currents will be presented in Section 6.2.

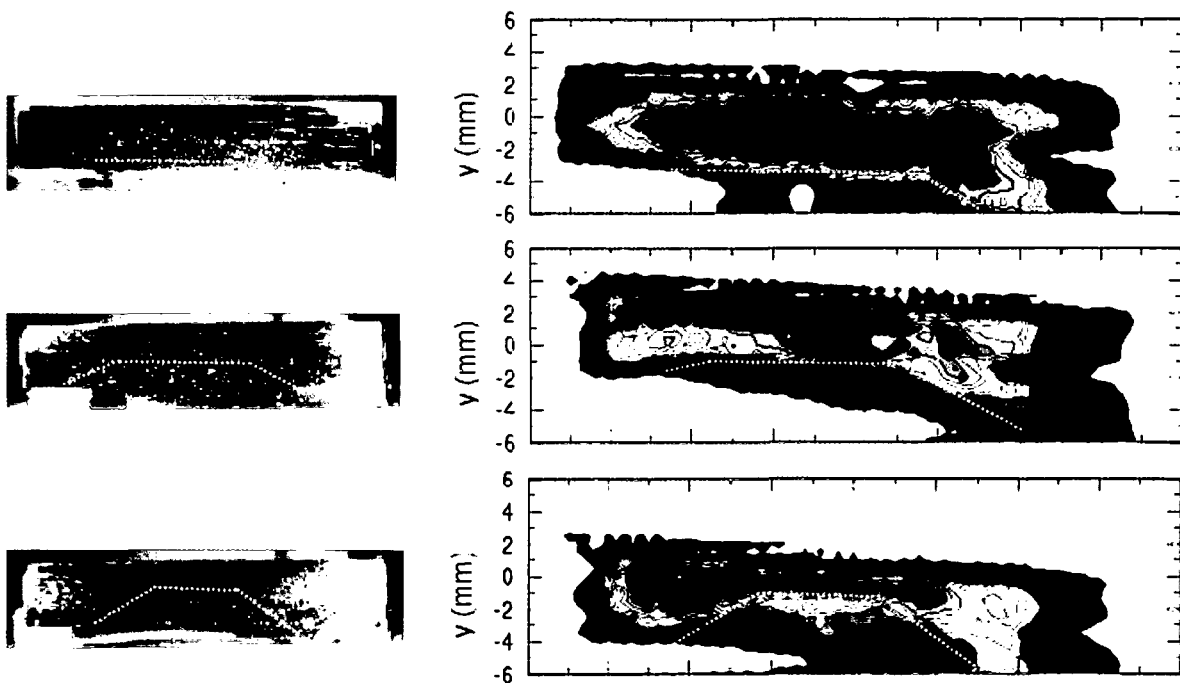


Fig. 72: Photograph of the other slices (left) and magnetoscans (right) of sample *SLY-14-21*.

The *c*-GS is indicated by a dotted line.

6.1.2 Mapping of subgrain free regions

Figure 73a shows a picture of the top side of the sample, where subgrain-free regions are clearly observed along the growth sector boundaries. There are *a-a*-growth sector boundaries as well as *a-c*-growth sector boundaries. A number of grains and subgrains are observed inside the four *a*-growth sectors and in the *c*-growth sector. A schematic representation of the growth sectors and growth sector boundaries, as seen in the photograph, is shown in figure 73b. Figures 73c and 73d present two trapped field measurements on the same sample. Table 16 lists experimental parameters. A color code of the measured trapped field values is not of importance in this case, because we are only interested in a qualitative interpretation. Comparing these data with the photograph, the local maxima of the trapped field distribution are located precisely at the growth sector boundaries. Trapped field measurements in the zfc mode are extremely sensitive to growth induced inhomogeneities like growth sector

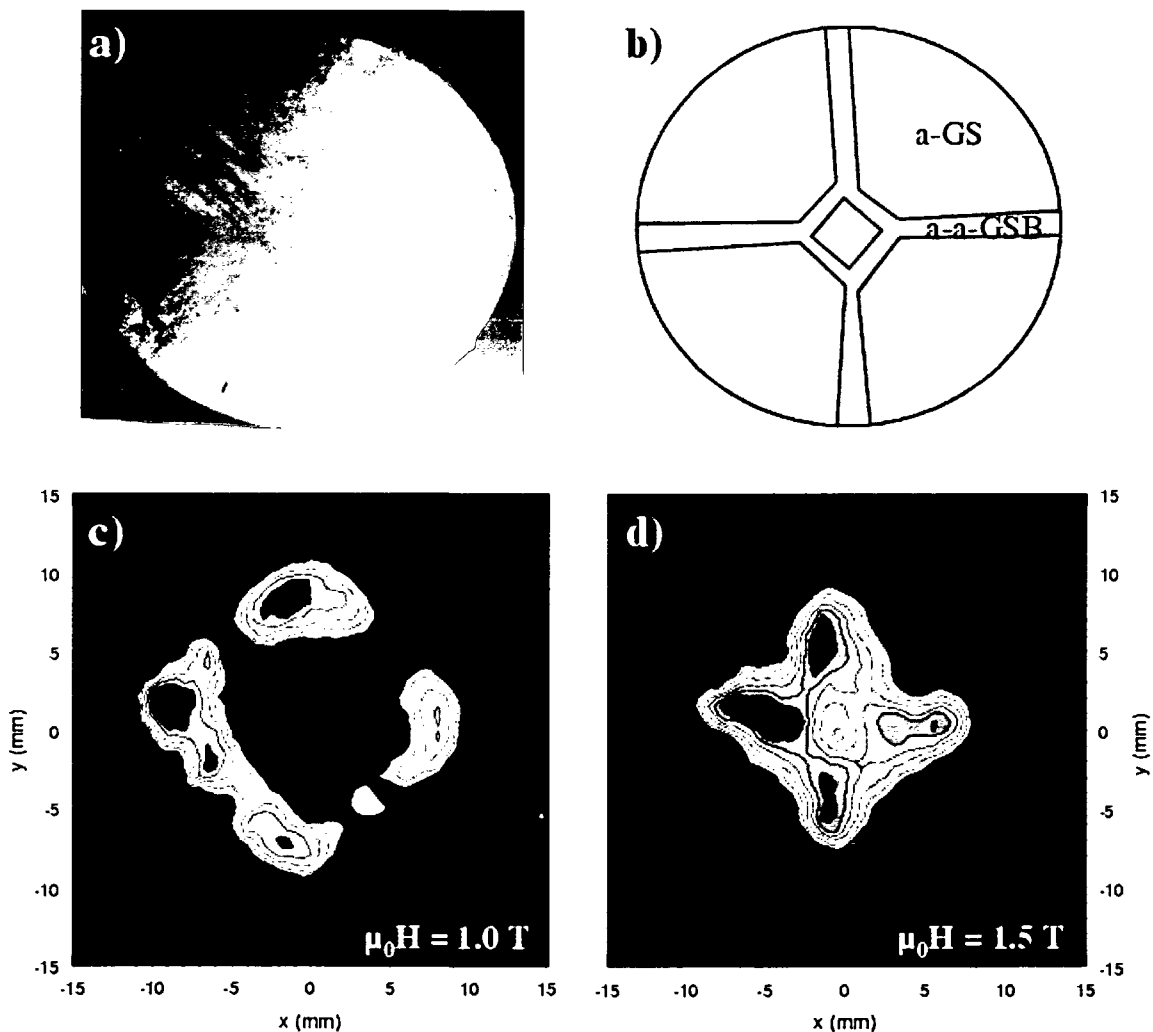


Fig. 73: a) Picture of the top side of the sample. b) Schematic view of the growth sectors and the growth sector boundaries. c), d) Trapped field measurements on the same sample at different activation fields.

Table 16: Parameters of trapped field measurements shown in Fig. 73c) and 73d).

sample code	<i>Li0at6Nr2 (YBCO + 0.6 at% Li)</i>
Hall probe	<i>HHP-SF-301</i>
grid size	<i>0.5 mm × 0.5 mm</i>
gap	<i>0.2 mm</i>
start after activation	<i>15 min</i>
activation field	<i>1.0 T (zfc), 1.5 T (zfc)</i>

boundaries. Another example is shown in Fig. 74. Again the emphasis is placed on a qualitative interpretation. The activation field $\mu_0 H$ was 1.2 T. The four local maxima of the trapped field profile are located at the *a-a*-growth sector boundaries, which indicates that the flux penetration along the *a-a*-GSBs is different from the penetration directly into the *a*-growth sectors. Between the maxima, smaller irregularities in the trapped field profile can be detected. The shape of the *c*-growth sector can be roughly estimated, especially from the contour plot. Table 17 contains the parameters of the measurement in Fig. 74.

Comparable results were found with the magnetoscan. Fig. 75 shows the result of the magnetoscan of sample *Li0at6*. The most striking features are the depression of the signal (green) in the *c*-GS and an increased signal (red) in broad regions around the *a-a*-GSBs. VSM measurements on small reference samples cut from a Li-doped $\text{YBa}_2\text{Cu}_3\text{O}_{7.8}$ bulk sample (similar to the other Li-doped $\text{YBa}_2\text{Cu}_3\text{O}_{7.8}$ samples) were carried out at 77.8 K.

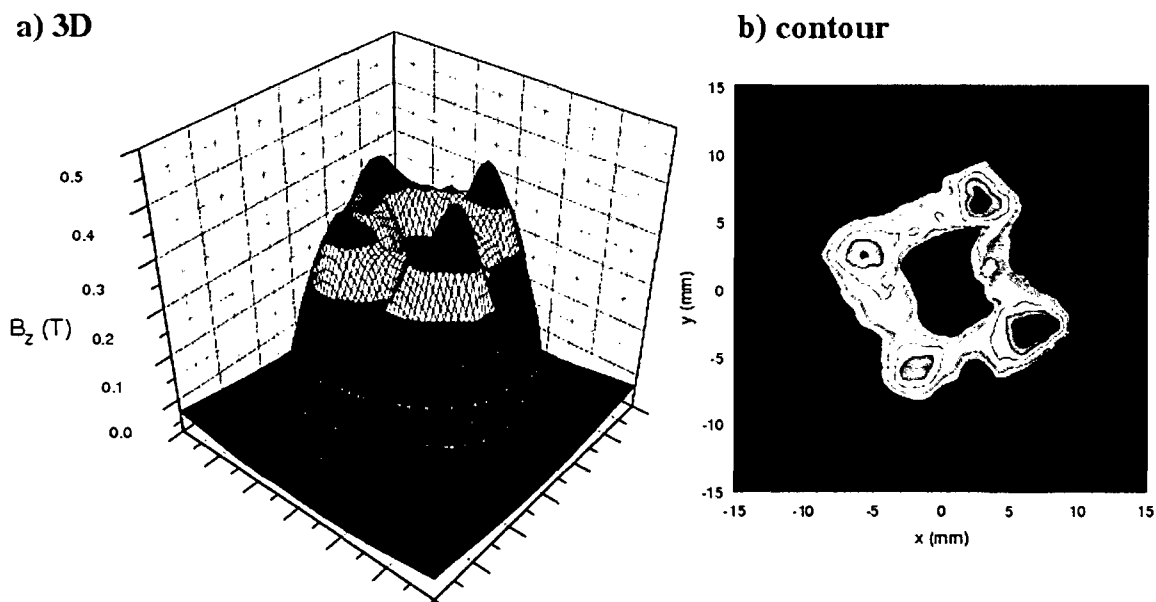


Fig. 74: a) 3-dimensional trapped field pattern. b) Contour plot of the same measurement.

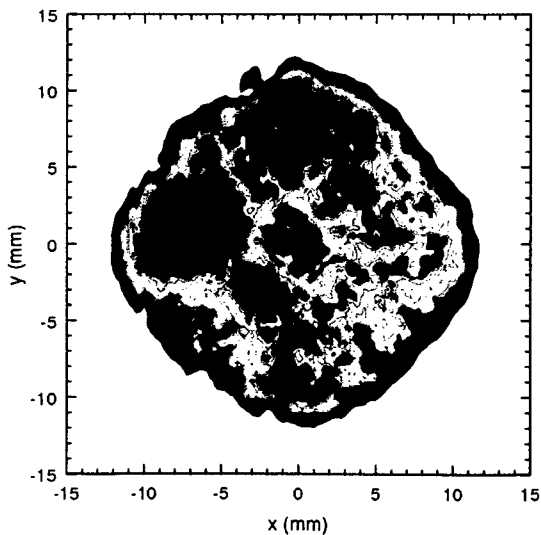
Table 17: Parameters of trapped field measurements shown in Fig. 74.

sample code	<i>Li0at5 (YBCO + 0.5 at% Li)</i>
Hall probe	<i>HHP-SF-301</i>
grid size	<i>0.25 mm × 0.25 mm</i>
gap	<i>0.2 mm</i>
start after activation	<i>15 min</i>
activation field	<i>1.2 T (zfc)</i>

The specimens were taken from different positions, so that a position sensitive interpretation was possible. The measured magnetization loops and, hence, the calculated critical current densities J_C were compared. The critical current densities J_C of the specimen taken from the *a-a*-GSB was highest, whereas those of the specimen taken from the *c*-GS was lowest. Further, J_C in the *a*-GS showed lower values than J_C at the *a-a*-GSB. This result can directly be related to the results of the magnetoscan. Fig. 76 shows the results of the position dependence of the critical current in a surface layer of the bulk sample. The sample had a diameter of 26 mm, i.e. “0” refers to the center of the sample, and “12” is the position at the edge of the sample.

Table 18: Parameters of the magnetoscan shown in Fig. 75.

sample code	<i>Li0at6 (YBCO + 0.6 at% Li)</i>
Hall probe	<i>HHP-VPO-48</i>
grid size	<i>0.25 mm × 0.25 mm</i>
gap	<i>0.2 mm</i>

Fig. 75: Magnetoscan of the top side of the sample *Li0at6*.

Considering the results of the trapped field scans, the magnetoscan, the VSM measurements and the optical investigation of the sample surface, a strong correlation is established between grain boundary free regions (*a-a*-GSB) and high critical currents.

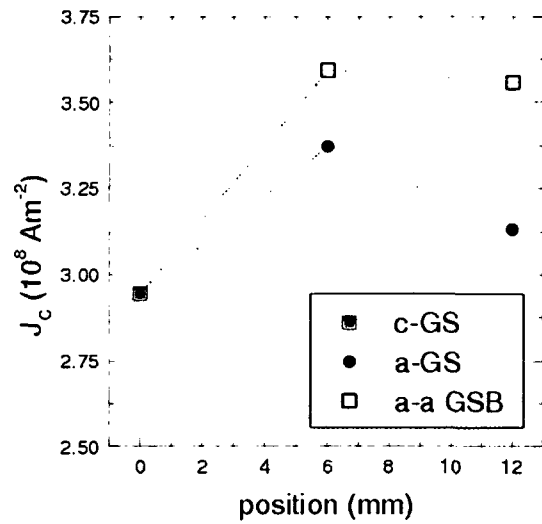


Fig. 76: Critical current densities dependent on the position of the reference samples in the bulk.

6.1.3 Flux penetration into $\text{YBa}_2\text{Cu}_3\text{O}_{7.8}$ bulk superconductors *Np-6* and *Np-11*

The stepwise flux penetration into the samples *Np-6* and *Np-11* was investigated, in order to characterize them in detail before irradiation. Both samples show similar results, which demonstrates the good quality and uniformity of the production within the same batch. Also the maximum trapped fields of both samples are in good agreement. The highest trapped fields were reached after activation at 2.5 T. For sample *Np-6*, however, the location of the maximum was slightly out of center, as shown in Fig 77.

The reported maximum trapped field (IPHT Jena) was $B_{T,max} = 0.955$ T in the case of sample *Np-6*, 97 % of the value measured at ATI. In the case of sample *Np-11* the reported value was $B_{T,max} = 0.785$ T, 80 % of the value measured at ATI. The standard measurement parameters in Jena are slightly different: activation in the fc mode at $\mu_0 H = 2.0$ T, the gap is 0.6 mm and the grid size is 1 mm \times 1 mm. The larger gap is responsible for the difference in the results.

Table 19: Comparison between sample *Np-6* and sample *Np-11*
($\mu_0 H = 2.5$ T in zfc mode) measured at the top side

sample code	<i>Np-6</i>	<i>Np-11</i>
temperature control	77.73 ± 0.17 K	77.76 ± 0.04 K
grid size	0.5 mm \times 0.5 mm	0.5 mm \times 0.5 mm
gap	0.2 mm	0.2 mm
start after activation	15 min	15 min
$B_{T,max}$	0.986 T	0.983 T

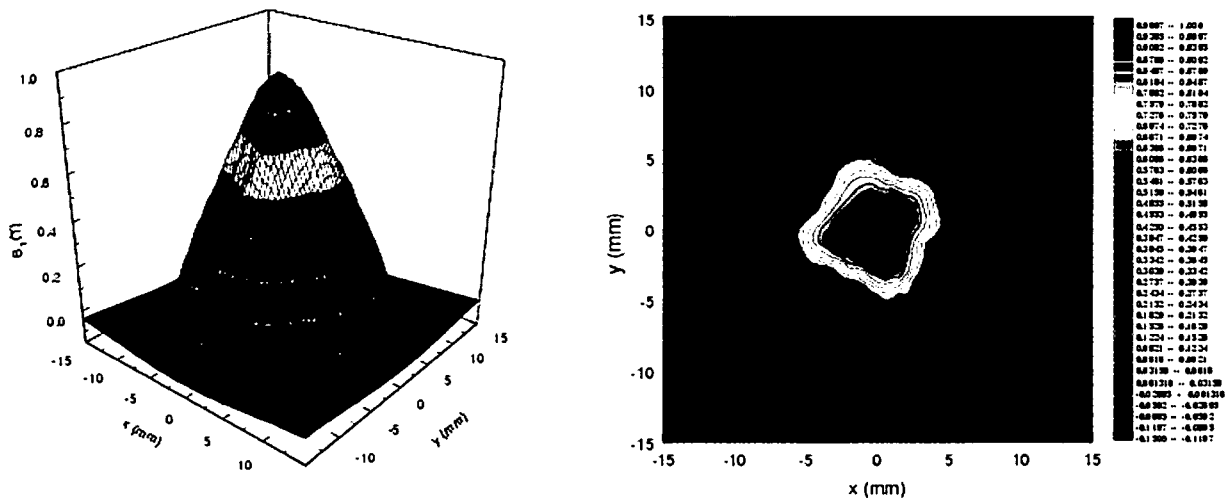


Fig. 77: Trapped field of sample *Np-6* at an activation of 2.5 T.

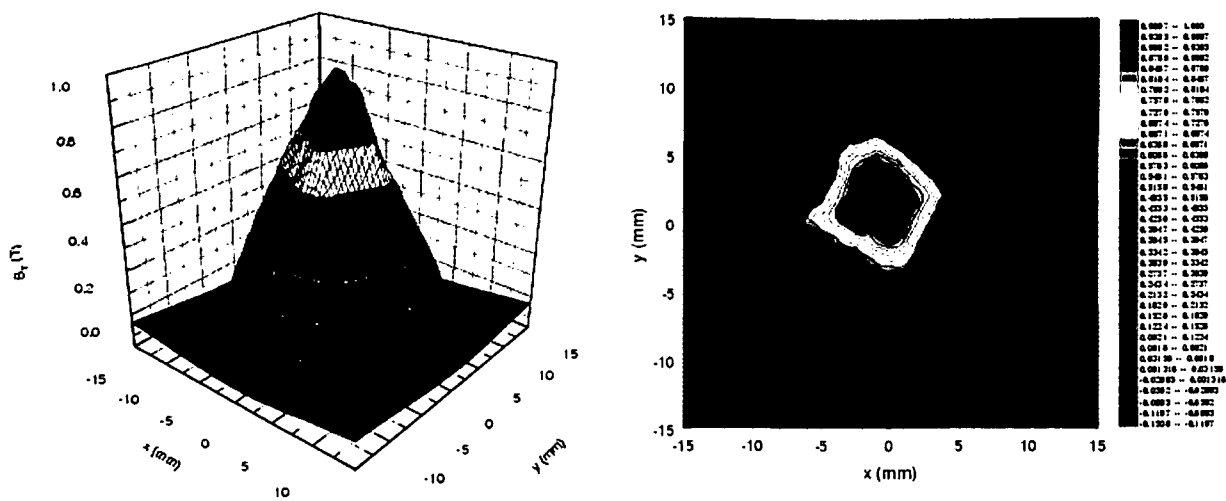


Fig. 78: Trapped field of sample *Np-11* at an activation of 2.5 T.

The homogeneous trapped field pattern in the fully activated state on the top side was compared to a Hall scan of the bottom side. A scan of the bottom side is an initial indication of its axial homogeneity. Again the samples were activated under a magnetic field of 2.5 T in the zfc mode.

Table 20: Trapped Field measurements of sample *Np-6* and *Np-11*
($\mu_0 H = 2.5$ T in zfc mode) measured at the bottom side

sample code	<i>Np-6</i>	<i>Np-11</i>
temperature control	78.18 ± 0.07 K	77.74 ± 0.01 K
grid size	0.5 mm \times 0.5 mm	0.5 mm \times 0.5 mm
gap	0.2 mm	0.2 mm
start after activation	15 min	15 min
$B_{T,max}$	0.421 T	0.418 T

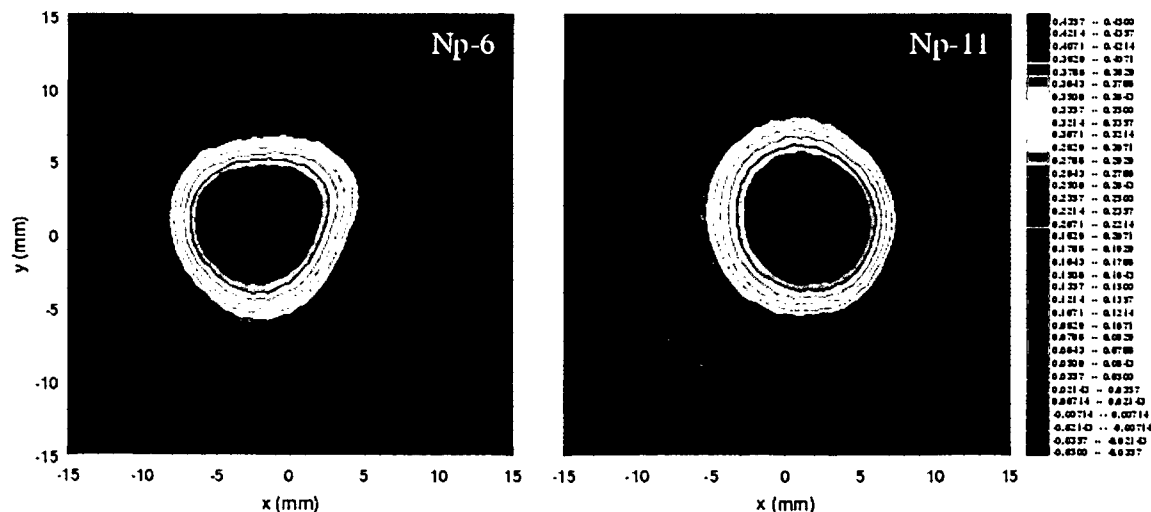


Fig. 79: Hall scan of the bottom side of *Np-6* (left) and *Np-11* (right) after an activation of 2.5 T.

Both samples showed a homogeneous trapped field pattern also at the bottom side. The trapped fields were again comparable: The maximum trapped field of *Np-6* was 0.421 T, that of *Np-11* 0.418 T.

A detailed investigation of the flux penetration into samples *Np-6* and *Np-11* followed. Figs. 80 and 81 show contour plots of Hall scans after increasing the zfc activation field from 0.1 T to 2.5 T for samples *Np-6* and *Np-11*, respectively. As already discussed for the Li-doped samples with respect to the subgrain free regions near *a-a*-GSBs, local maxima at the *a-a*-GSBs can be observed in Hall scans, when the sample is not fully magnetized. Interestingly, samples *Np-6* and *Np-11* show various local maxima occurring in the trapped field pattern in addition to the major four maxima along the *a-a*-GSBs. An optical investigation of the sample surface did not show many subgrains. This leads to the conclusion, that the subgrain formation in these samples is not as dense as in, the Li-doped $\text{YBa}_2\text{Cu}_3\text{O}_{7.8}$ bulk samples manufactured at IFW Dresden. The reason for this difference may be found in the manufacturing process itself. More detailed investigations of the seed crystal did not lead to new results. The seeds were ordinary Sm-123 seeds of rectangular shape. Table 21 lists the parameters of each measurement.

The maximal trapped field values as a function of the activation field are shown in Fig. 82. The results demonstrate again the reproducibility of the sample quality within batches achieved by IPHT Jena. The trapped field increases linearly up to an activation of $\mu_0 H = 2.5$ T where saturation occurs. All measurements were performed in liquid nitrogen at similar temperatures ($T \approx 77.8$ K) and at the same distance of 0.2 mm (gap) above the sample surface.

The maximal trapped field values of the samples after an activation at $\mu_0 H = 3.0$ T are slightly smaller (-6 % for *Np-6*, -2 % for *Np-11*) than those at $\mu_0 H = 2.5$ T. This was observed for many samples. The lower value for sample *Np-6* can be attributed mainly to a higher temperature of the liquid nitrogen bath during the Hall scan, which was 78.36 ± 0.07 K in this case. It is known from previous measurements, that the trapped field value is strongly dependent on the temperature. An increase in temperature by 1 K results in a reduction of the trapped field by up to 10% [65]. However, the temperature of the liquid nitrogen bath during the scan of sample *Np-11* (activation at 3.0 T) was 77.77 ± 0.03 K, which is comparable to the average temperature of the Hall scan after activation at 2.5 T. This suggests that additional, non-negligible influences on the trapped field, exist. Because of the activation mode dependence, the sweep rate during activation could have some influence, although this was not confirmed for these samples.

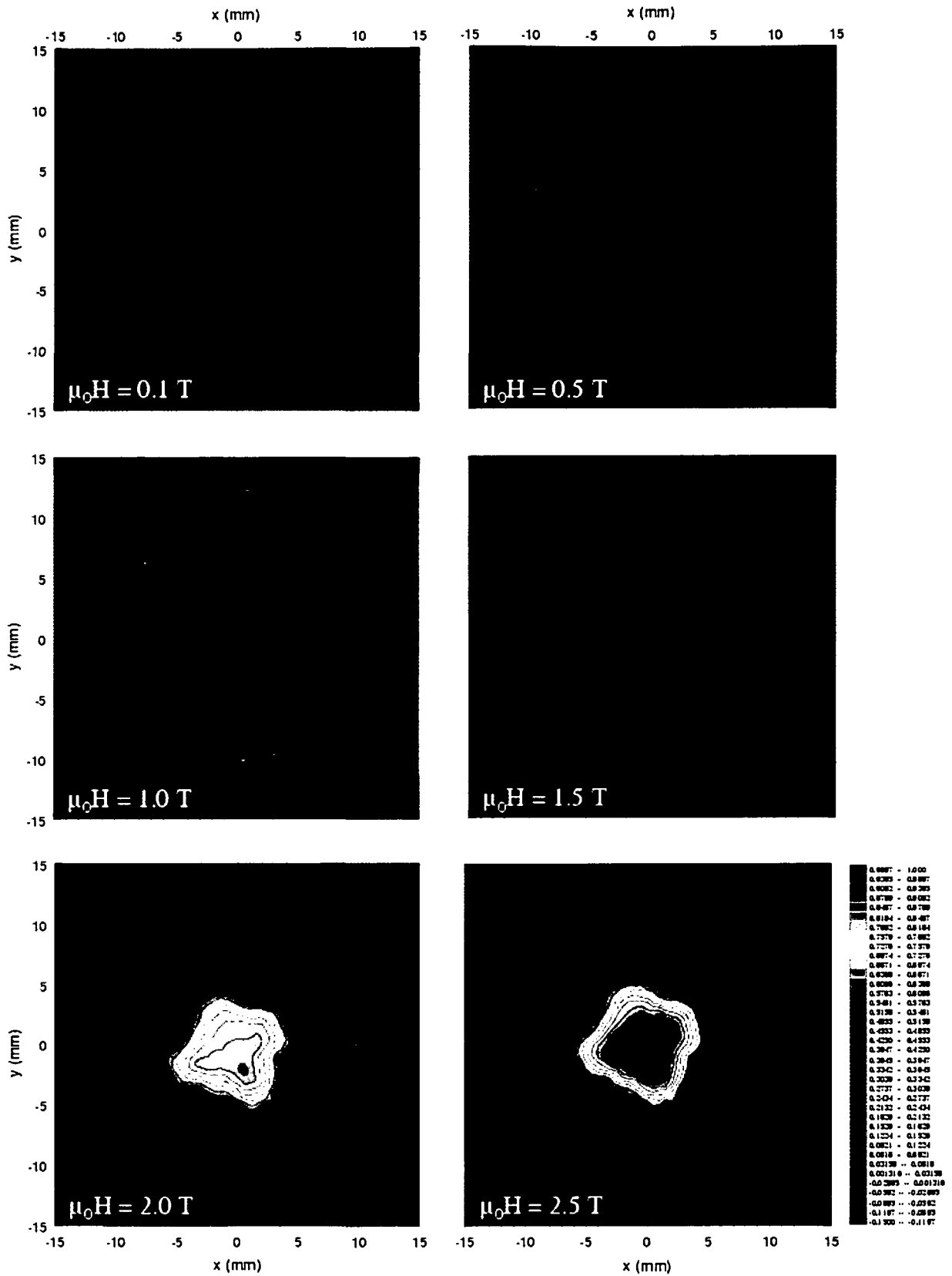
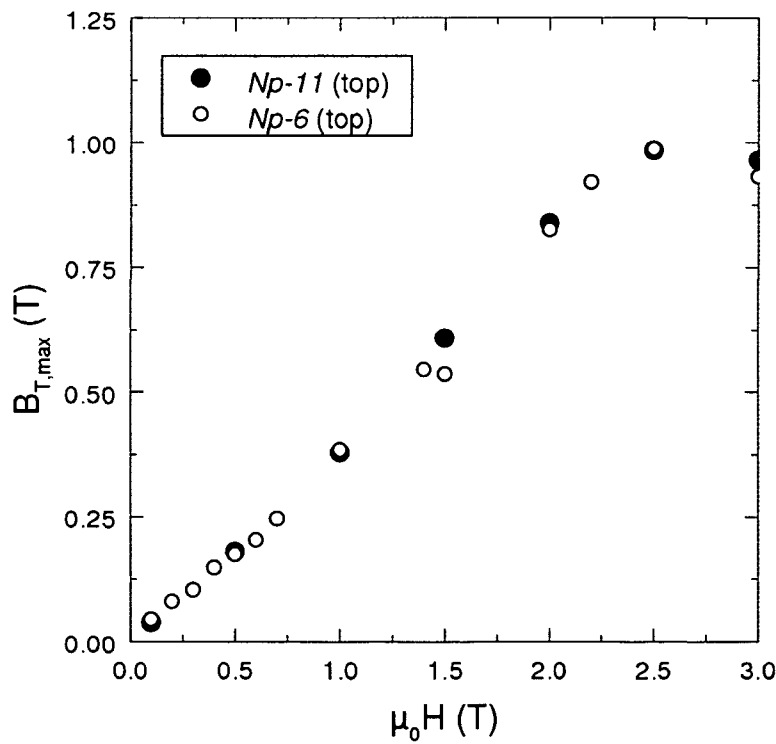


Fig. 80: Flux penetration into sample Np-6.

Table 21: Parameters of selected Hall scan measurements for *Np-6* and *Np-11* and maximal trapped fields

sample code	<i>Np-6</i>				
activation field	temperature	grid size	gap	start	$B_{T,max}$
0.1 T	77.96 ± 0.03 K	0.25 mm \times 0.25 mm	0.2 mm	15 min	0.044 T
0.5 T	77.68 ± 0.05 K	0.25 mm \times 0.25 mm	0.2 mm	15 min	0.175 T
1.0 T	78.35 K	0.25 mm \times 0.25 mm	0.2 mm	15 min	0.384 T
1.5 T	77.74 ± 0.04 K	0.25 mm \times 0.25 mm	0.2 mm	15 min	0.544 T
2.0 T	77.99 ± 0.05 K	0.25 mm \times 0.25 mm	0.2 mm	15 min	0.825 T
2.5 T	77.73 ± 0.07 K	0.50 mm \times 0.50 mm	0.2 mm	15 min	0.986 T
sample code	<i>Np-11</i>				
activation field	temperature	grid size	gap	start	$B_{T,max}$
0.1 T	77.64 ± 0.05 K	0.25 mm \times 0.25 mm	0.2 mm	15 min	0.038 T
0.5 T	77.69 ± 0.03 K	0.25 mm \times 0.25 mm	0.2 mm	15 min	0.180 T
1.0 T	77.70 ± 0.05 K	0.25 mm \times 0.25 mm	0.2 mm	15 min	0.378 T
1.5 T	77.74 ± 0.04 K	0.25 mm \times 0.25 mm	0.2 mm	15 min	0.607 T
2.0 T	77.81 ± 0.04 K	0.50 mm \times 0.50 mm	0.2 mm	15 min	0.838 T
2.5 T	77.76 ± 0.04 K	0.50 mm \times 0.50 mm	0.2 mm	15 min	0.983 T

Fig. 82: Maximal trapped field of *Np-6* and *Np-11* as a function of the activation field ($T \approx 77.8$ K).

6.1.4 Flux penetration into Li-doped $\text{YBa}_2\text{Cu}_3\text{O}_{7.8}$ bulk superconductors

The flux penetration into Li-doped $\text{YBa}_2\text{Cu}_3\text{O}_{7.8}$ samples was already partly discussed in *Chapter 6.1.2*, where mapping of subgrain-free regions by Hall scans after activating the sample in the zfc mode at fields below $2H^*$ was demonstrated.

During the investigation of melt grown bulk superconductors, it was found that saturation and, therefore, the maximum trapped field cannot be determined by one single measurement alone. Fig. 83 shows the results of three measurements on the same sample, *Li0at6Nr2*, but activated at different fields: 2.0 T, 2.5 T and 3.0 T. Each measurement shows a “regular” trapped field cone, but only a comparison shows that the maximum trapped field differs. For a maximum trapped field of $B_{T,max} = 0.989$ T, an estimation of the full magnetization in the zfc mode leads to an activation field of $\mu_0 H = 2.0$ T. But, as can be clearly seen from Fig. 83, the saturation value, $B_{T,max}$, of the sample is obviously reached only after an activation of 3.0 T. The parameters of the scans and the maximal trapped fields can be found in Table 22. It should be pointed out, that the flux penetration there is qualitatively similar, i.e. Hall scans after an activation at 2.5 T and 3.0 T do not provide additional information on the homogeneity of the sample.

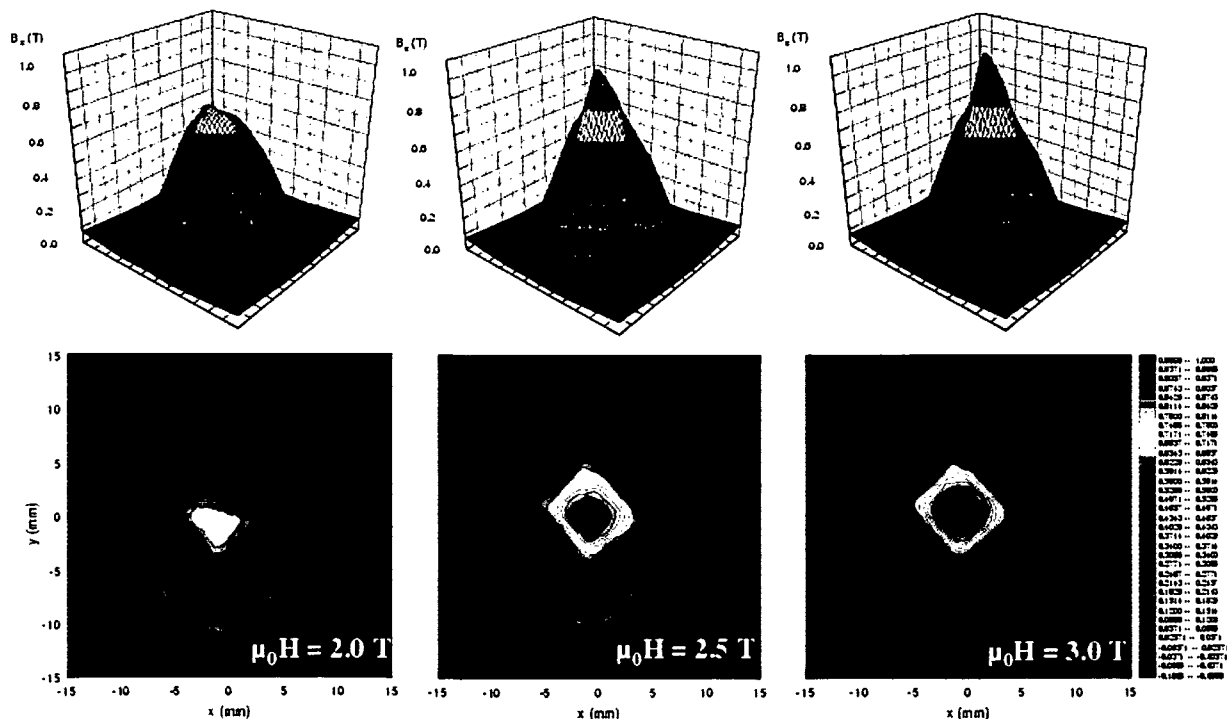


Fig. 83: 3D- and contour plots of the trapped flux distribution in sample *Li0at6Nr2*.

Table 22: Hall scans of the top surface of sample *Li0at6Nr2*.

activation field	2.0 T	2.5 T	3.0 T
grid size	0.5 mm × 0.5 mm	0.5 mm × 0.5 mm	0.5 mm × 0.5 mm
gap	0.2 mm	0.2 mm	0.2 mm
start after activation	15 min	15 min	15 min
$B_{T,max}$	0.688 T	0.922 T	0.989 T

A detailed investigation of the flux penetration shows the difficulties in an accurate determination of H^* . Fig 84 shows four Hall scans of the top surface of sample *Li0at5* at different activation fields $\mu_0 H = 0.6$ T, 0.7 T, 0.8 T and 0.9 T. Taking cross sections of these profiles along $x = 0$, a slight increase of the trapped field in the center of the sample can be observed, when the activation field is increased. According to the definition of H^* , a clear joining of the left and the right flux fronts occurs after an activation at 0.8 T.

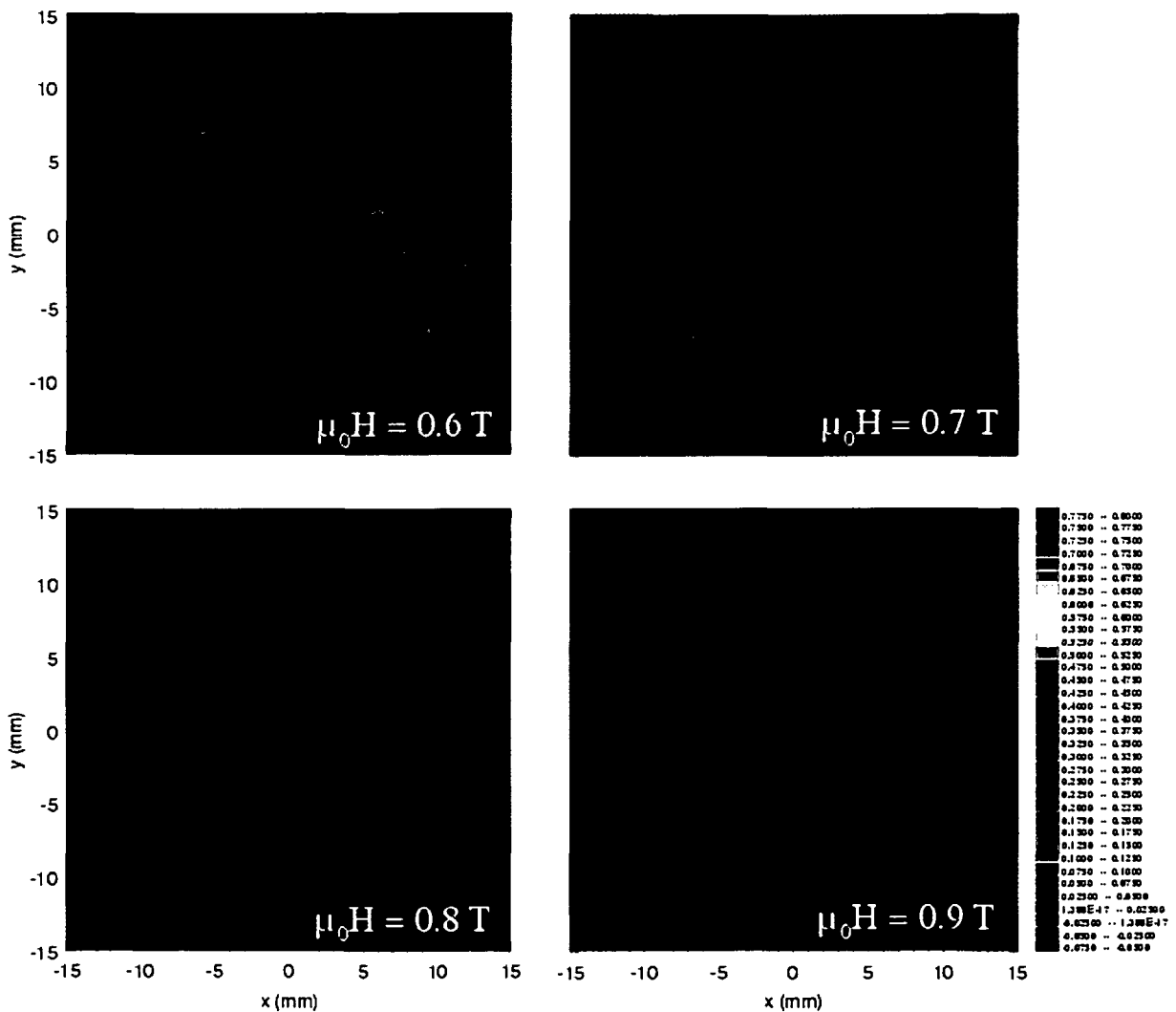
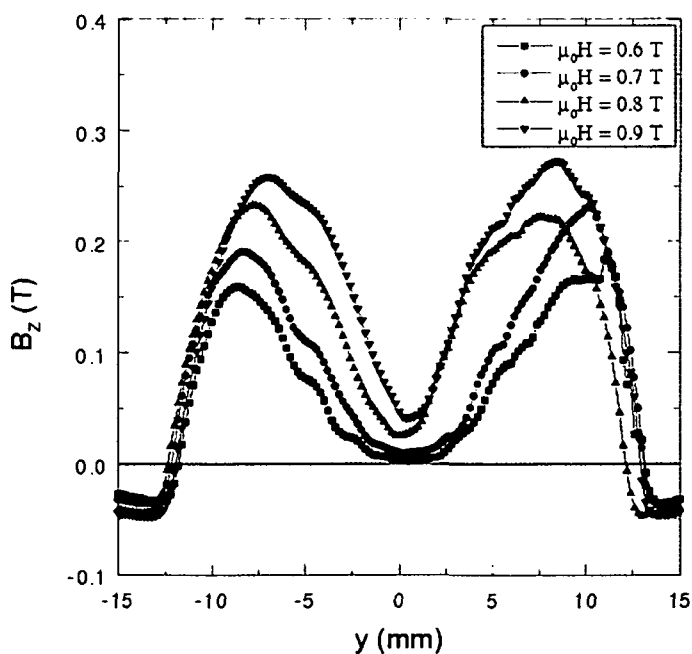
Fig. 84: Flux penetration into sample *Li0at5* near H^* .

Table 23: Hall scans of the top surface of sample *Li0at6Nr2*.

activation field	0.6 T	0.7 T	0.8 T	0.9 T
grid size	0.2 mm × 0.2 mm			
gap	0.2 mm	0.2 mm	0.2 mm	0.2 mm
temperature control	77.54 ± 0.02 K	77.54 ± 0.02 K	77.59 ± 0.04 K	77.66 ± 0.16 K
start after activation	15 min	15 min	15 min	15 min
$B_{T,max}$	0.230 T	0.260 T	0.318 T	0.353 T

The parameters of these measurements are listed in Table 23. For sample *Li0at5*, the results on the flux penetration as a function of the activation field were already published in [77]. The data at higher activation fields (1.4 T – 1.6 T) also show interesting features in the *c*-GS. A comparison with the magnetoscan reveals a distorted symmetry of the flux penetration due to cracks in the top surface of the sample (Fig. 86a-d). Two irregularities are indicated by small arrows and a circle. The vertical analysis of this sample will be presented in the next chapter, where it is reported, that the marked crack can be located after having reduced the thickness by several millimeters. Thus, such irregularities as observed in the Hall scans of Fig. 86 provide direct evidence for a larger current flow barrier somewhere in the sample volume.

Fig. 87 summarizes the maximal trapped fields of the Li-doped $YBa_2Cu_3O_{7-8}$ samples as a function of the activation field. The slope of the linear increase is 0.39, in good agreement with Bean's model (including demagnetization corrections).

Fig. 85: Cross sections of the trapped flux profiles of sample *Li0at5*.

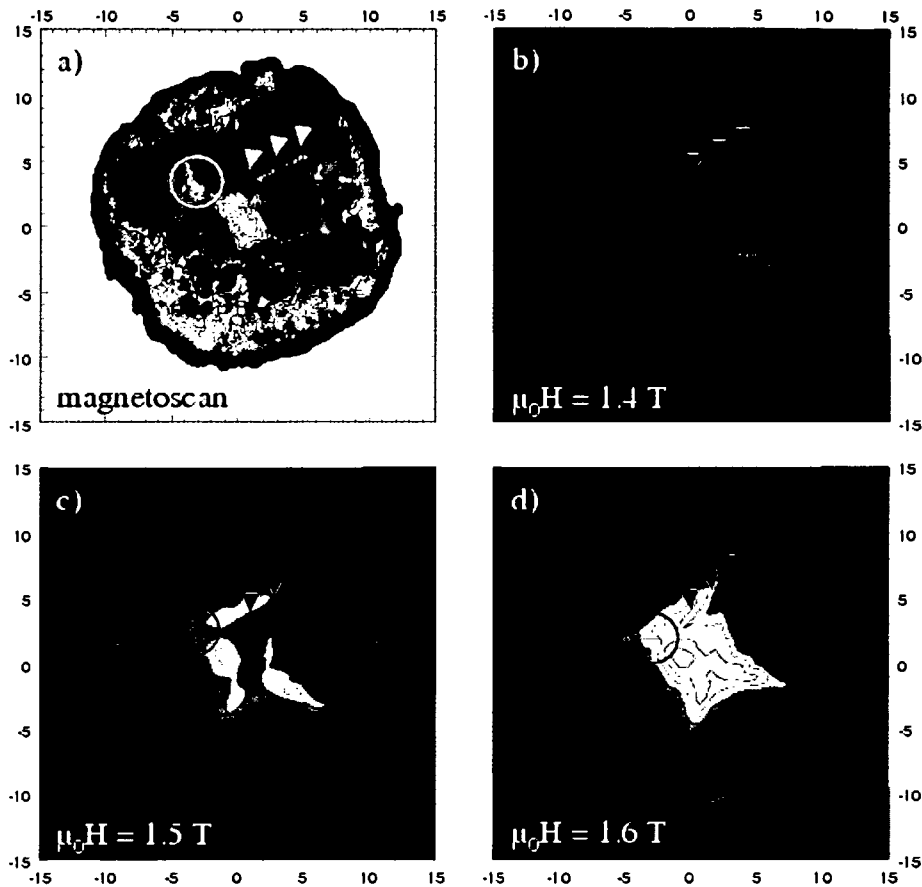


Fig. 86: Comparison of a) magnetoscan and b)-d) zfc Hall scans at higher activation fields: $\mu_0 H = 1.4$ T, 1.5 T and 1.6 T.

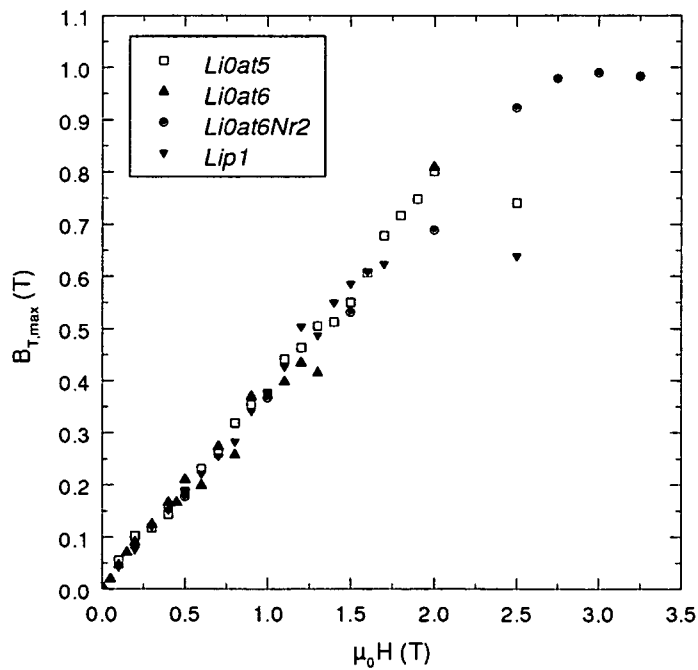


Fig. 87: Maximal trapped fields of the Li-doped $\text{YBa}_2\text{Cu}_3\text{O}_{7.8}$ samples as a function of the activation field ($T \approx 78$ K).

6.2 Vertical homogeneity of TSMG bulk superconductors

An analysis of melt-textured bulk superconductors in vertical direction was made by a stepwise reduction of their thickness followed by conventional Hall scans and magnetoscans. The idea of a vertical assessment of the bulk superconductor in such a way is slightly different from cutting the monolith horizontally into slices. For a preliminary test of this idea, an ordinary $\text{YBa}_2\text{Cu}_3\text{O}_{7.8}$ bulk, sample *H186*, was investigated [78].

Fig. 88 compares the measured maximal trapped field as a function of thickness with the theoretical curve, assuming a sample with the same geometry and a constant current density of $J_C = 8.8 \cdot 10^7 \text{ Am}^{-2}$ [79-80]. The deviation from the theoretical behavior shows clearly, that the critical current density cannot be assumed to be constant, but is locally perturbed. Qualitatively, trapped field scans of the saturated sample and magnetoscans at each grinding step offer local information on inhomogeneities occurring with increasing vertical distance from the seed position (Figs. 89 and 90).

The main results are: *i)* The increasing *c*-GS with decreasing thickness is directly mapped by the magnetoscan. *ii)* Misaligned grains, mostly at the edge of the monolith, occur, when the thickness is reduced, and they directly affect the result of the magnetoscan. *iii)* In the contour plots of the remnant flux, cracks from the edge of the monolith are observed to influence the flux distribution, when the thickness is reduced by 2.4 mm. Apparently these cracks severely reduce the current flow in the bulk volume. However, a loss of homogeneity can already be seen by the asymmetric double peak structure of the trapped field, when the thickness is only slightly reduced.

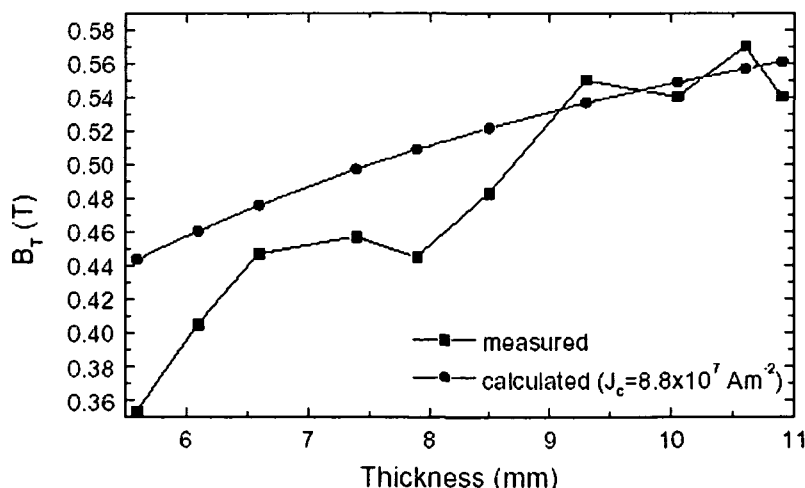


Fig. 88: Maximal trapped field value versus thickness of the sample [78].

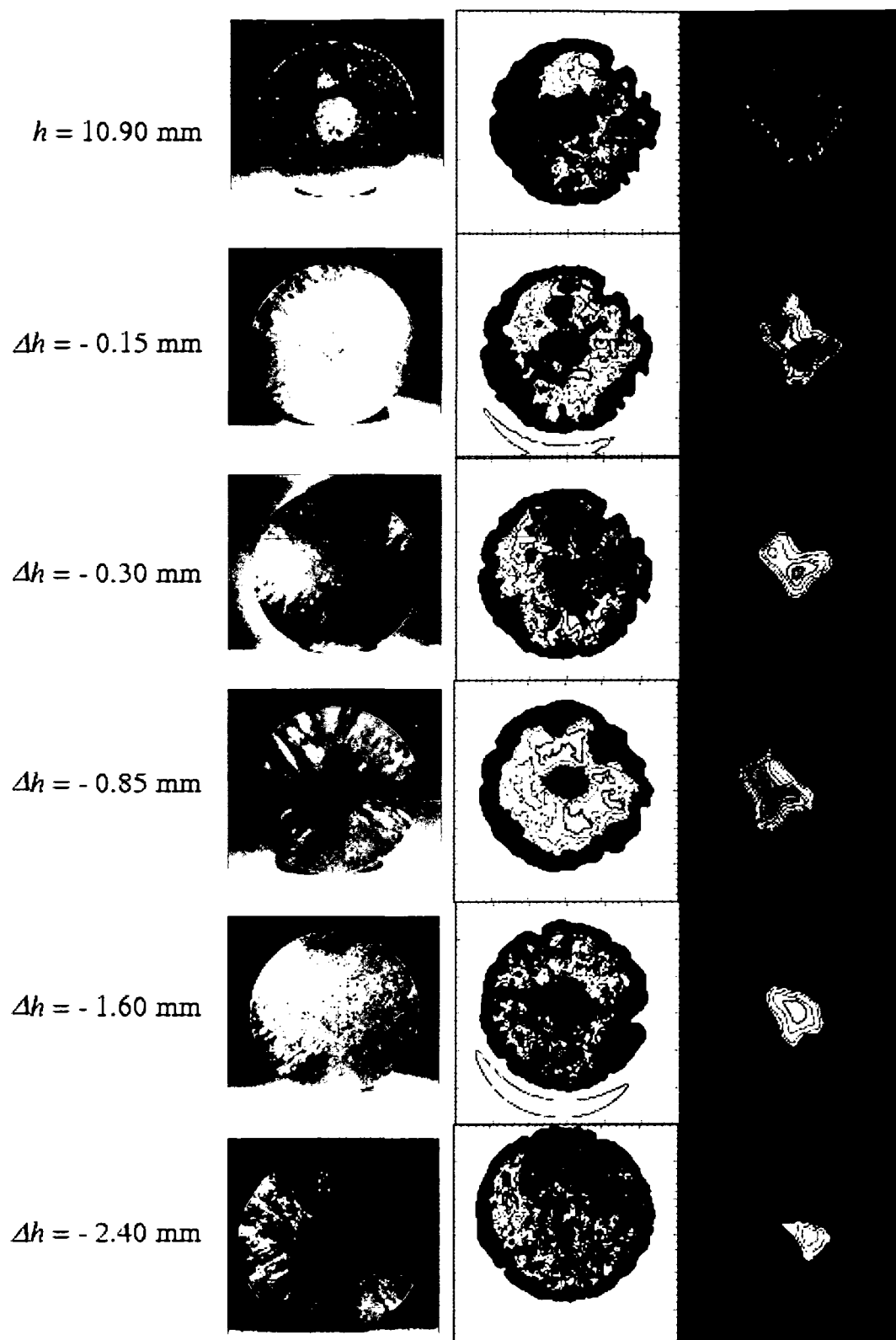


Fig. 89: Vertical assessment of sample *H186*. Photograph of the sample surface, magnetoscan and saturated trapped flux distribution for decreasing thickness.

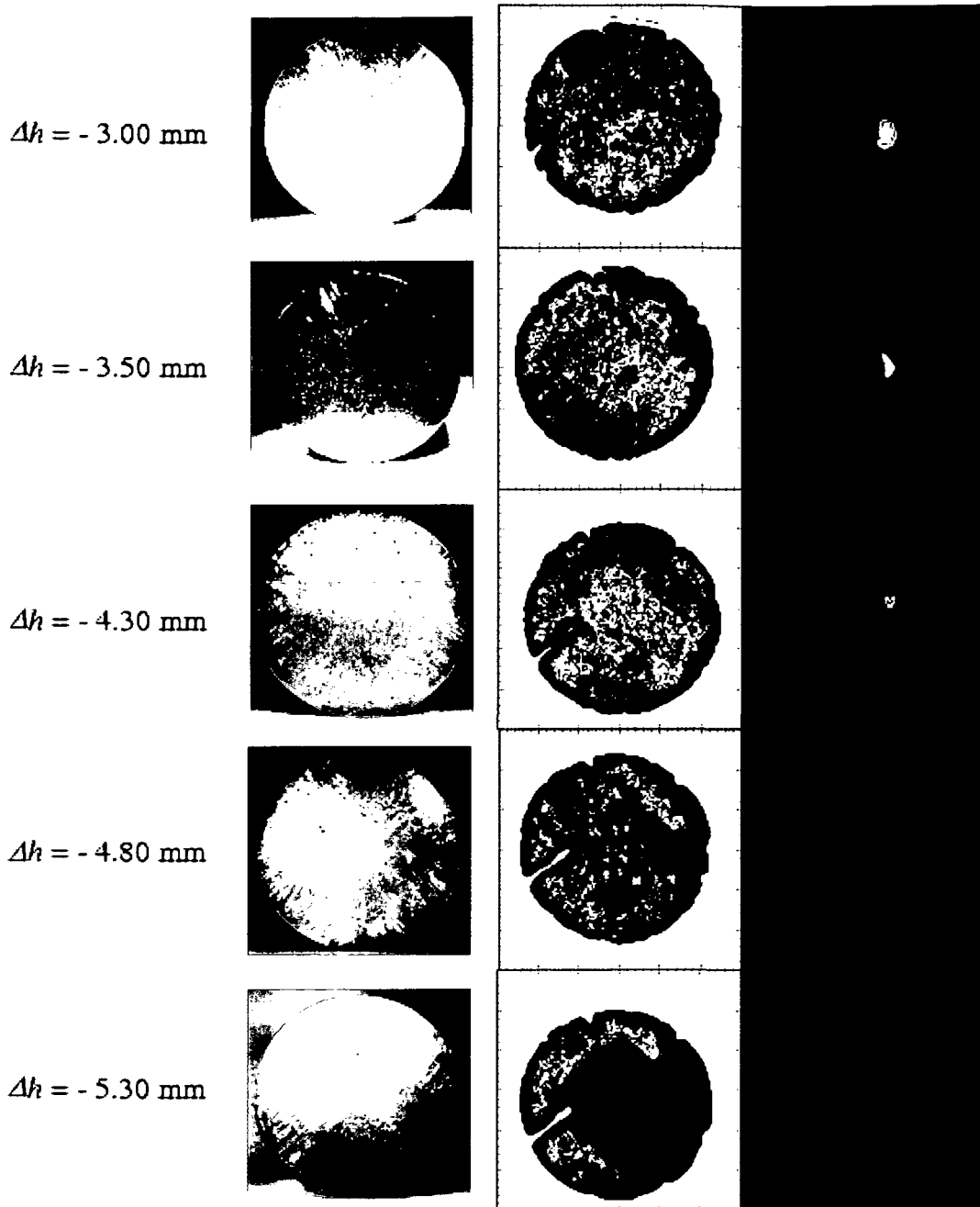


Fig. 90: Vertical assessment of sample *H186*. Continuation of Fig. 89.

The same experiment was done on sample *Li0at5*. The sample showed a homogeneous trapped field profile at its original thickness, but the axial symmetry of the field profile disappeared after having removed a layer of several millimeters from the top. A double-cone of the remnant field is then found, which is caused by a crack. Trapped field scans following different activation fields show a non-uniform flux penetration due to inhomogeneities, as already discussed. Fig. 91 shows magnetoscans with decreasing sample thickness. Local inhomogeneities, primarily cracks in the *c*-GS, were detected by the magnetoscan technique

and numerous grain boundaries were found after removing several layers from the top surface, which were identified by optical and polarized light microscopy. Note, that the crack mentioned in Fig. 86 disappears (Fig. 91b) and re-appears again (Fig. 91c). Fig. 92 shows the maximal trapped fields of zfc measurements as a function of the activation field. Taking the saturation value at $\mu_0 H = 2.0$ T, the geometrical dependence of the trapped field can be evaluated.

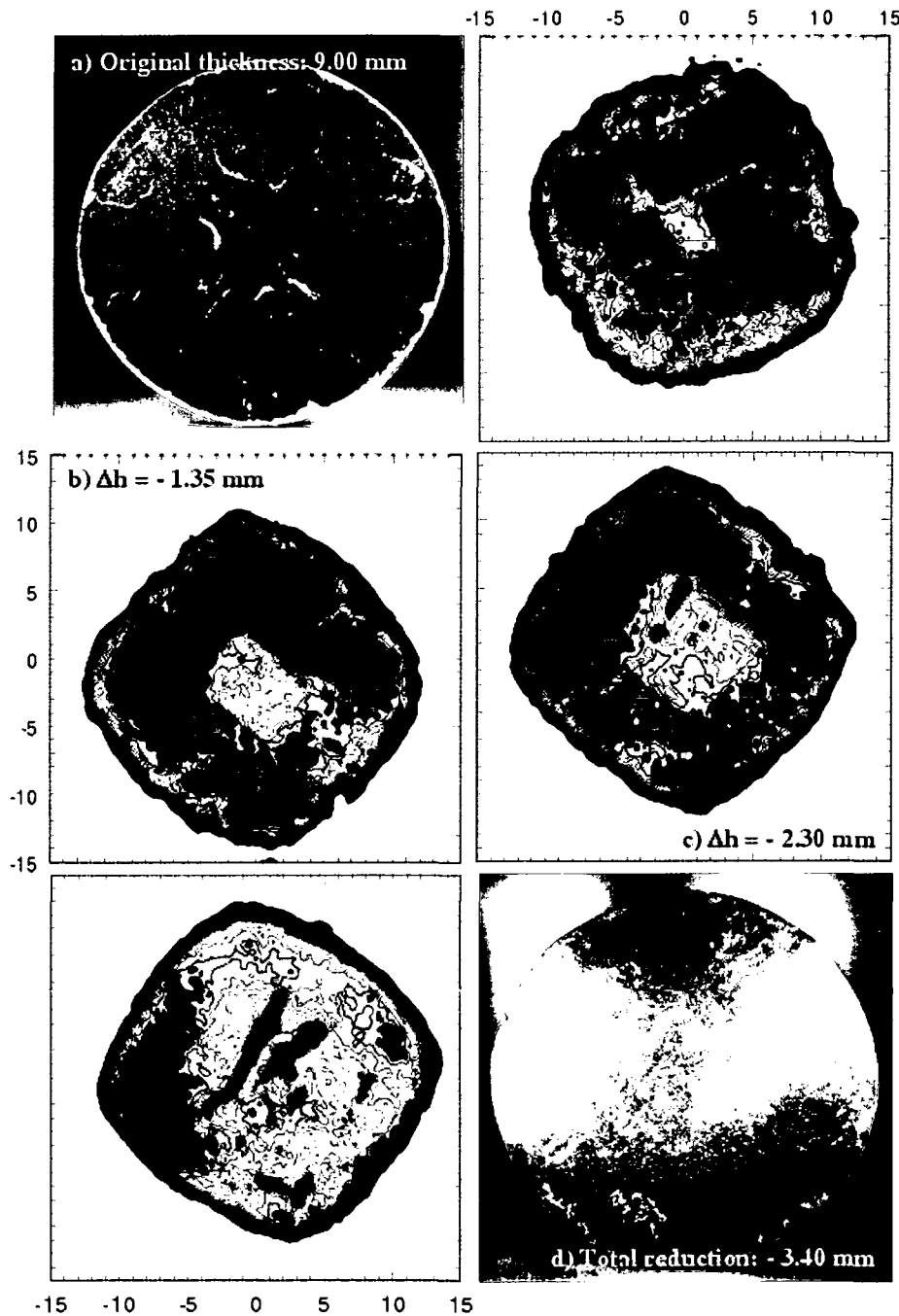


Fig. 91: Magnetoscan of sample *Li0at5* at a) the original thickness, and at b) - d) reduced thicknesses. Appearing cracks in the *c*-GS.

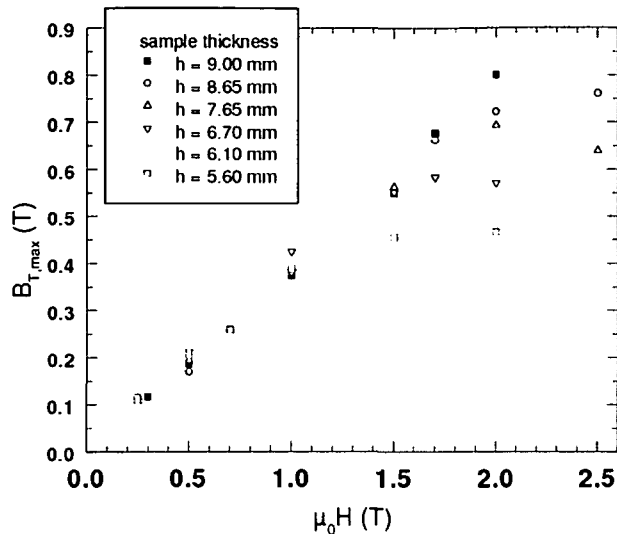


Fig. 92: Maximal trapped field values as function of the activation field and for different sample thicknesses.

The maximal trapped fields as a function of sample thickness (Fig. 93), match the assumption of a constant critical current density of $J_C = 1.02 \cdot 10^8 \text{ Am}^{-2}$ matches much better than for sample *HI86*.

In addition, XRD-measurements were performed on the remaining powder after each grinding step [81]. The resulting maxima in the peaks of the Y-123 phase and the Y-211 phase were analyzed. In this way, the average Y-211 content in horizontal layers of the sample can be deduced. An increase of the Y-211 phase was found with increasing vertical distance from the seed.

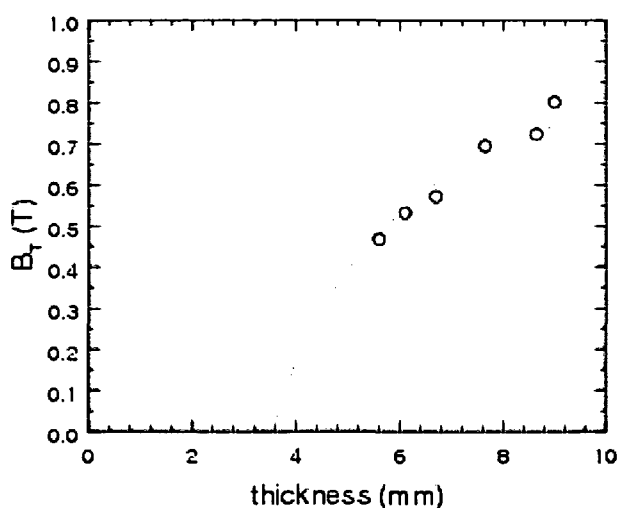


Fig. 93: Maximum trapped field as a function of the thickness. The circles indicate the experimental results. Theoretical calculations yield the dashed curve. No significant deviations are found.

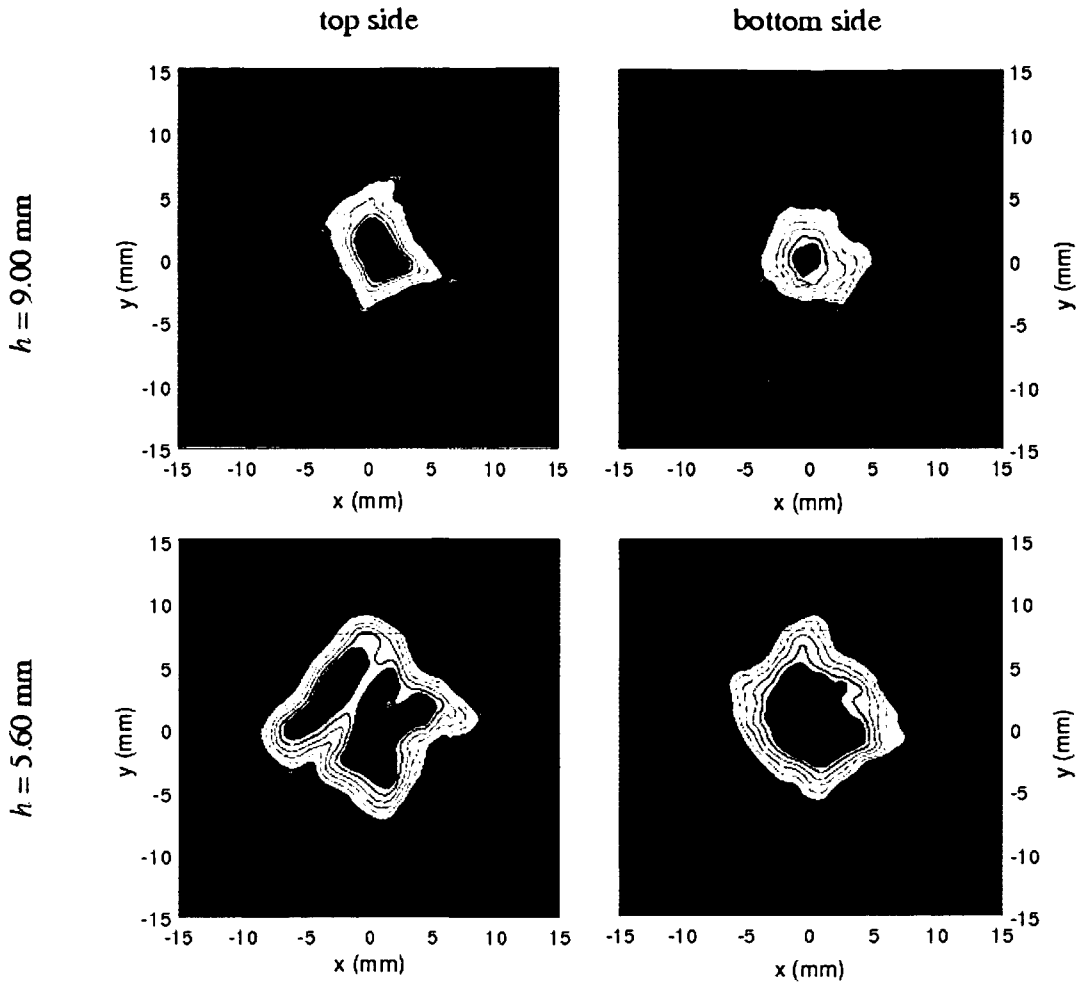


Fig. 94: Hall scans of the top and the bottom side (zfc) of Li_{0at5} with $h = 9.00$ mm and $h = 5.60$ mm.

Further investigations of the homogeneity involved Hall scans of the bottom side of the sample. Fig. 94 shows the field maps after zfc activation of the top and the bottom side of the sample Li_{0at5} at two different thicknesses. Whereas the trapped field pattern of the top side is obviously changed, nearly no changes were detected in the Hall scan of the bottom side.

Table 24: Parameters of trapped field measurements (zfc) shown in Fig. 94.

thickness	9.00 mm		5.60 mm	
	top	bottom	top	bottom
grid size	$0.25 \times 0.25 \text{ mm}^2$			
gap	0.2 mm	0.2 mm	0.2 mm	0.2 mm
$\mu_0 H$	2.0 T	2.0 T	1.5 T	1.5 T
start after activation	15 min	15 min	15 min	15 min
$B_{T,max}$	0.801 T	0.676 T	0.455 T	0.499 T

6.3 Results of Neutron Irradiation

6.3.1 Neutron irradiation of $\text{YBa}_2\text{Cu}_3\text{O}_{7-8}$: *Np-11*

Neutron irradiation of the $\text{YBa}_2\text{Cu}_3\text{O}_{7-8}$ sample *Np-11* showed an enhancement of the maximal trapped fields, as already often observed before [65]. At an activation field of 2.5 T, the maximal trapped field $B_{T,max}$ increases from 0.983 T to 1.343 T, i.e. the enhancement is 36% compared to the unirradiated state. Fig. 95 shows a comparison between the Hall scans of the unirradiated and the irradiated sample. Table 25 contains information on both measurements. The difference in the smoothness of the contour lines in Fig. 95 is a result of the different grid sizes employed. Also the temperature of the liquid nitrogen bath was 0.4 K higher during the scan of the irradiated sample. All other parameters of the experiment, such as the activation method (zfc), the gap between the sample surface and the Hall probe and the start of the measurement after activation, were not changed.

Table 25: Sample *Np-11* after an activation field of $\mu_0 H = 2.5$ T in zfc mode.

fluence	unirr	$2 \cdot 10^{21} \text{ m}^{-2}$
temperature control	$77.76 \pm 0.40 \text{ K}$	78.21 K
grid size	$0.5 \text{ mm} \times 0.5 \text{ mm}$	$0.25 \text{ mm} \times 0.25 \text{ mm}$
gap	0.2 mm	0.2 mm
start after activation	15 min	15 min
$B_{T,max}$	0.983 T	1.343 T

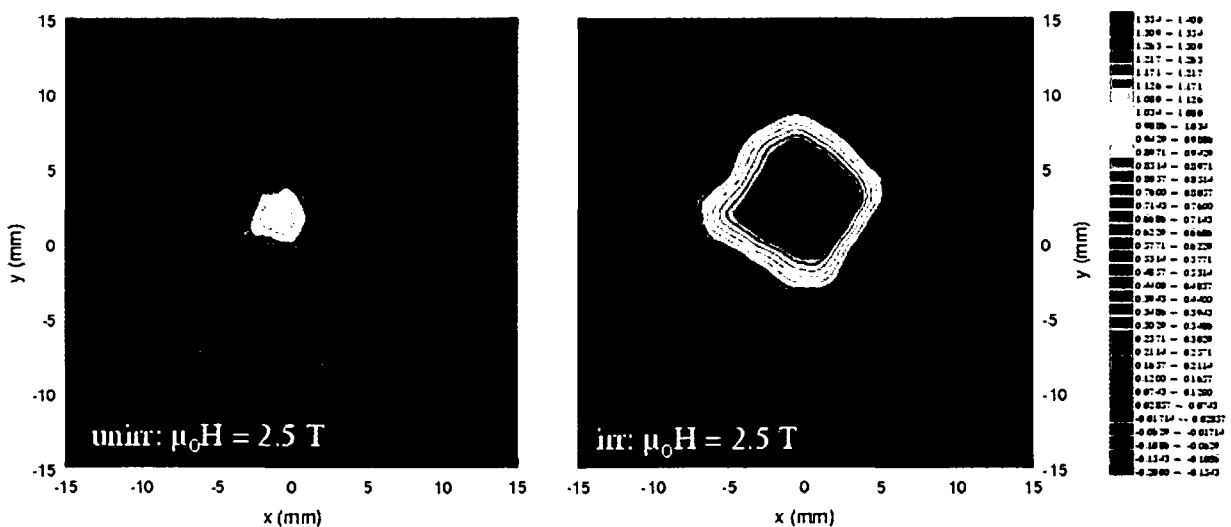


Fig. 95: Enhancement of the trapped field due to neutron irradiation.

Additional Hall scans were performed, in order to determine radiation induced effects on the homogeneity and the development of the maximal trapped fields as a function of the activation fields. Fig. 96 shows contour plots of Hall scans after an activation of 1 T. Because of the enhanced trapped field, the flux penetration inside the irradiated sample has not progressed as far as in the unirradiated state. Therefore, it is better to compare two measurements with approximately equal flux penetration. This is done in Fig. 97, where the Hall scan of the unirradiated sample after an activation at 0.5 T is compared to a Hall scan of the irradiated sample after an activation at 1.0 T. The arrows indicate example features in the trapped field pattern which occur before as well as after irradiation. The appearance of such similar inhomogeneities in the trapped field pattern indicate that their origin is growth induced and not radiation induced. This can be explained by a homogeneous distribution of defects induced by neutron radiation, but a comparatively small.

Table 26: Sample *Np-11* after an activation field of $\mu_0 H = 1.0$ T in zfc mode

fluence	unirr	$2 \cdot 10^{21} \text{ m}^{-2}$
temperature control	$77.69 \pm 0.50 \text{ K}$	$79.79 \pm 0.46 \text{ K}$
grid size	$0.25 \text{ mm} \times 0.25 \text{ mm}$	$0.25 \text{ mm} \times 0.25 \text{ mm}$
gap	0.2 mm	0.2 mm
start after activation	15 min	15 min
$B_{T,\text{max}}$	0.378 T	0.434 T

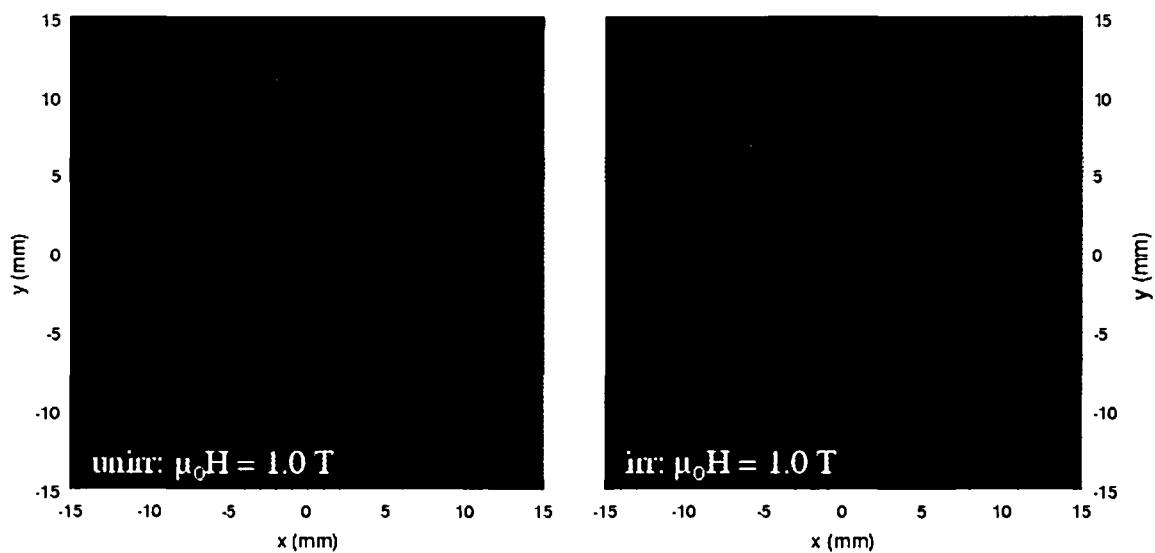


Fig. 96: Comparison between Hall scans after activation at 1 T in the unirradiated and the irradiated state.

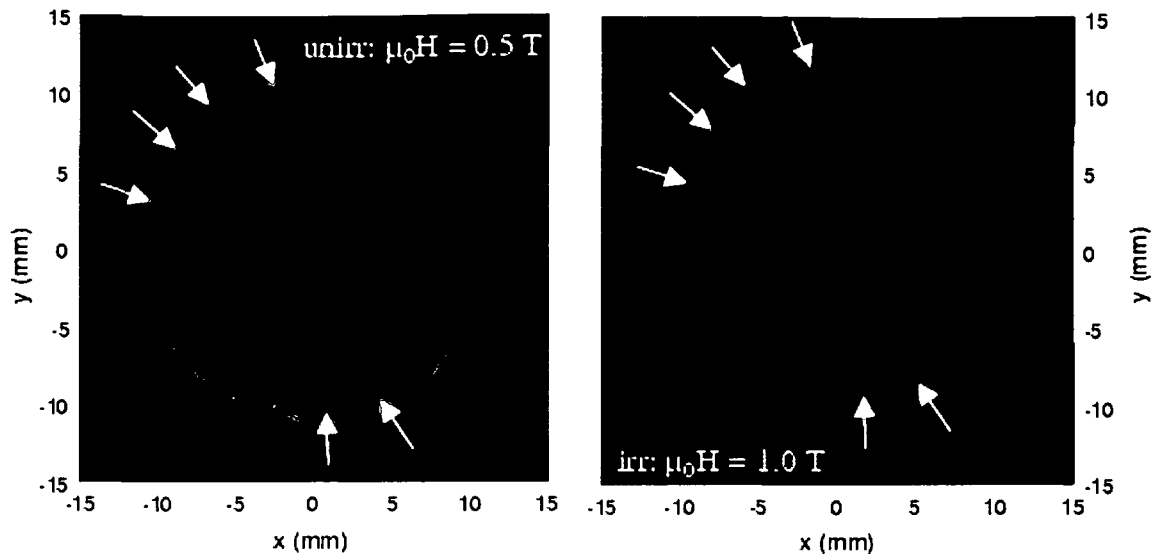


Fig. 97: Sample *Np-11* before and after irradiation.

Fig. 98 shows a comparison between magnetoscans performed before and after irradiation. No magnetoscan data on irradiated samples have been published so far. For clarity, the scales of the signal are the same for both measurements. Qualitatively, there is no distinct change in the pattern, but a clear increase of the signal is detectable over the whole sample. It should be noted, that *i*) the temperature of the liquid nitrogen bath during the magnetoscan of the irradiated sample was 2 K higher and *ii*) different Hall probes were used. The shift of the signal is more clearly visible in Fig. 99. At present, it is not clear whether this signal shift is radiation induced or only dependent on the different experimental conditions. Table 27 summarizes the important measurement parameters of the magnetoscans. Clearly, further experiments are highly desirable, in order to resolve these open issues.

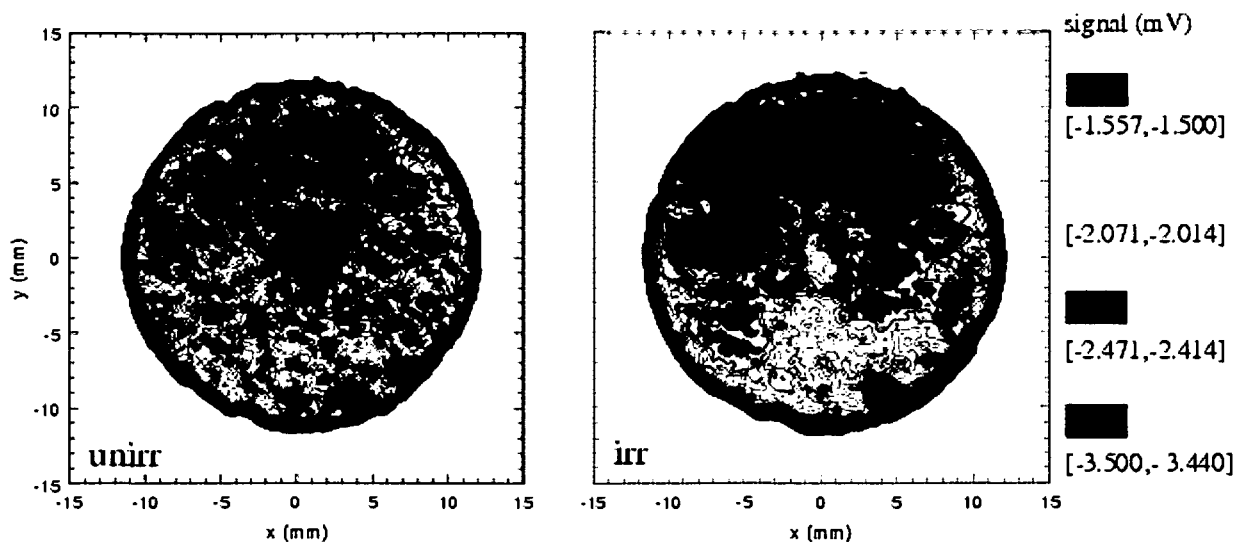
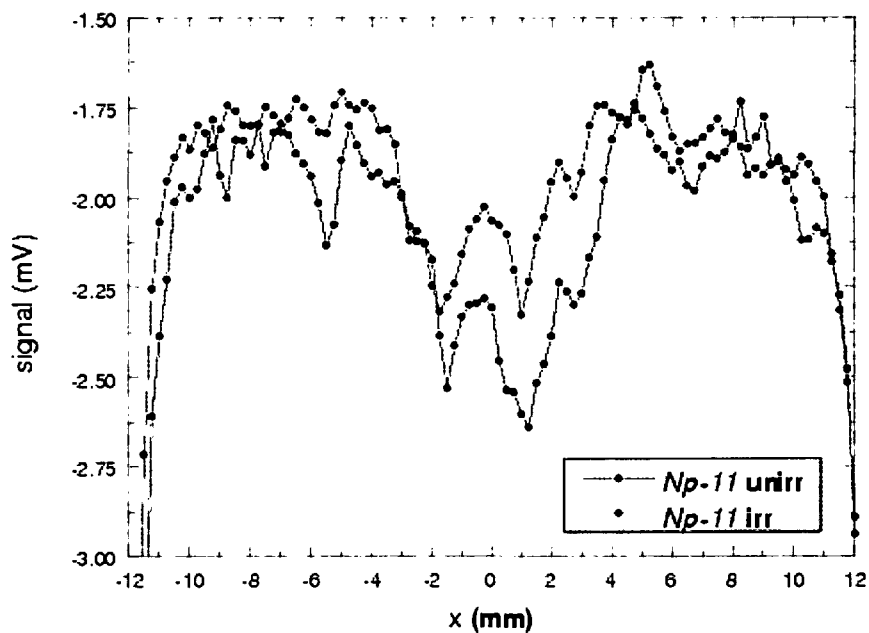


Fig. 98: Magnetoscan of sample *Np-11* before and after irradiation

Table 27: Parameters of the magnetoscans of the top surface of sample *Np-11*

fluence	unirr	$2 \cdot 10^{21} \text{ m}^{-2}$
temperature control	$77.87 \pm 0.16 \text{ K}$	$79.78 \pm 0.45 \text{ K}$
grid size	$0.25 \text{ mm} \times 0.25 \text{ mm}$	$0.25 \text{ mm} \times 0.25 \text{ mm}$
Hall probe	HHP VPO 48	HHP VU 492

Fig. 99: Cross sections of the magnetoscan signal of *Np-11* before and after irradiation.

6.4 Results on MSMG superconductors

6.4.1 Grain Boundaries in *MS-1*, *MS-2*, *MS-3* and *MS-4*

Conventional Hall scans of the MSMG samples *MS-1*, *MS-2*, *MS-3* and *MS-4* were done after activation in a 1.4 T electromagnet in the fc mode. The samples could not be activated in the superconducting magnet, because of their large size. The data show in general very irregular shapes of the trapped field patterns, especially sample *MS-1* and *MS-2*, and the maximum trapped fields are low. Grain boundaries influence the trapped flux distribution drastically. A micrograph of the grain boundary in sample *MS-1* was already shown in chapter 2 *Microstructure*. The inhomogeneous part of the trapped flux distribution of sample *MS-1* can be explained by massive cracks, caused by the different orientation of the seeds to each other.

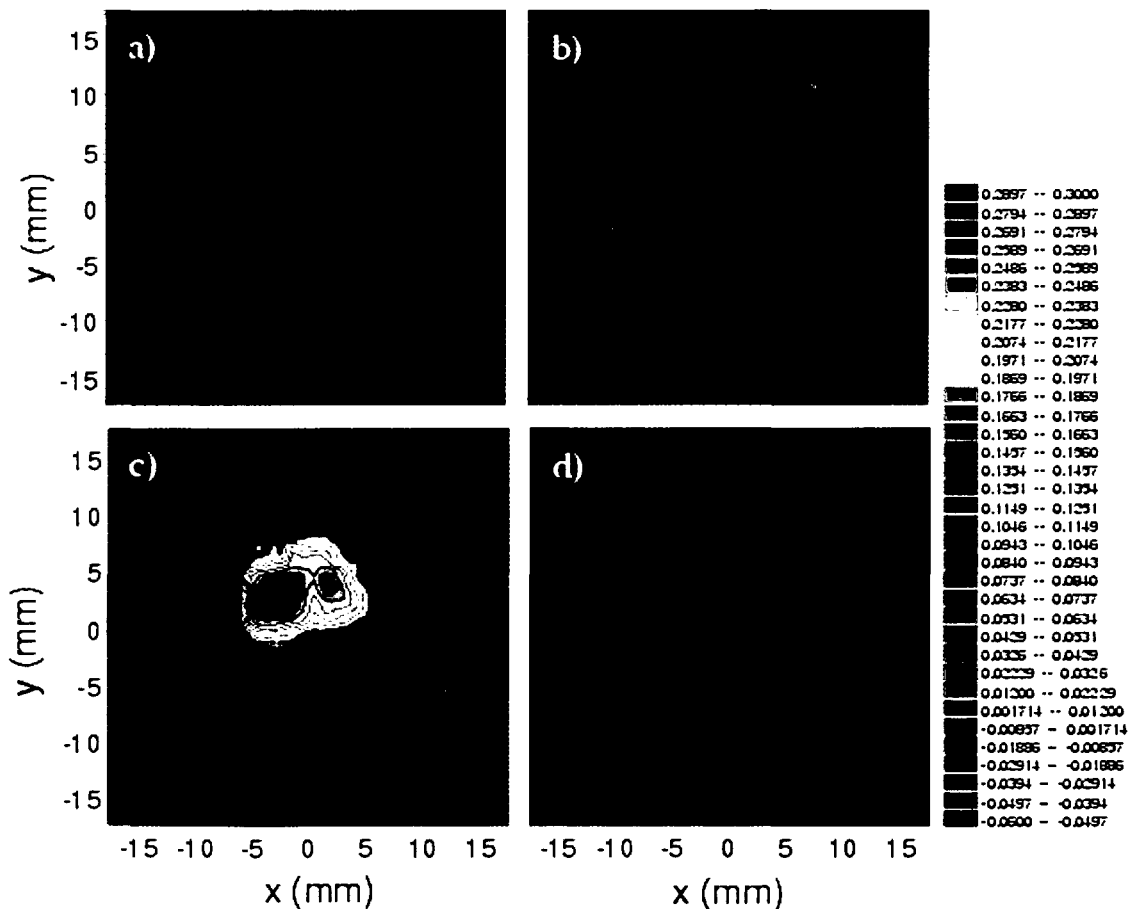


Fig. 100: Trapped flux distribution in samples a) *MS-1*, b) *MS-2*, c) *MS-3* and d) *MS-4*. The samples were activated by an 1.4 T electromagnet in fc mode. The scale is given in Tesla.

Table 28: Parameters of trapped field measurements (zfc) shown in Fig. 100.

sample code	<i>MS-1</i>	<i>MS-2</i>	<i>MS-3</i>	<i>MS-4</i>
grid size	$0.5 \text{ mm} \times 0.5 \text{ mm}$			
gap	0.2 mm	0.2 mm	0.2 mm	0.2 mm
temperature control	$77.76 \pm 0.06 \text{ K}$	$78.72 \pm 0.08 \text{ K}$	$78.40 \pm 0.15 \text{ K}$	$77.71 \pm 0.15 \text{ K}$
$\mu_0 H$ (fc)	1.4 T	1.4 T	1.4 T	1.4 T
start after activation	15 min	15 min	15 min	15 min
$B_{T,\text{max}}$	0.186 T	0.163 T	0.277 T	0.145 T

Table 28 summarizes the parameters of the Hall scans of the MSMG samples. The results of the magnetoscans (Fig. 101) of these samples confirm the inhomogeneity. The best shielding properties (red) of the samples can be found at the seed positions, but the shielding capability of these samples is very low. For sample *MS-1* the highest shielding can be found on the right, but the trapped fields are very inhomogeneous there. Table 29 contains the parameters of the magnetoscans.

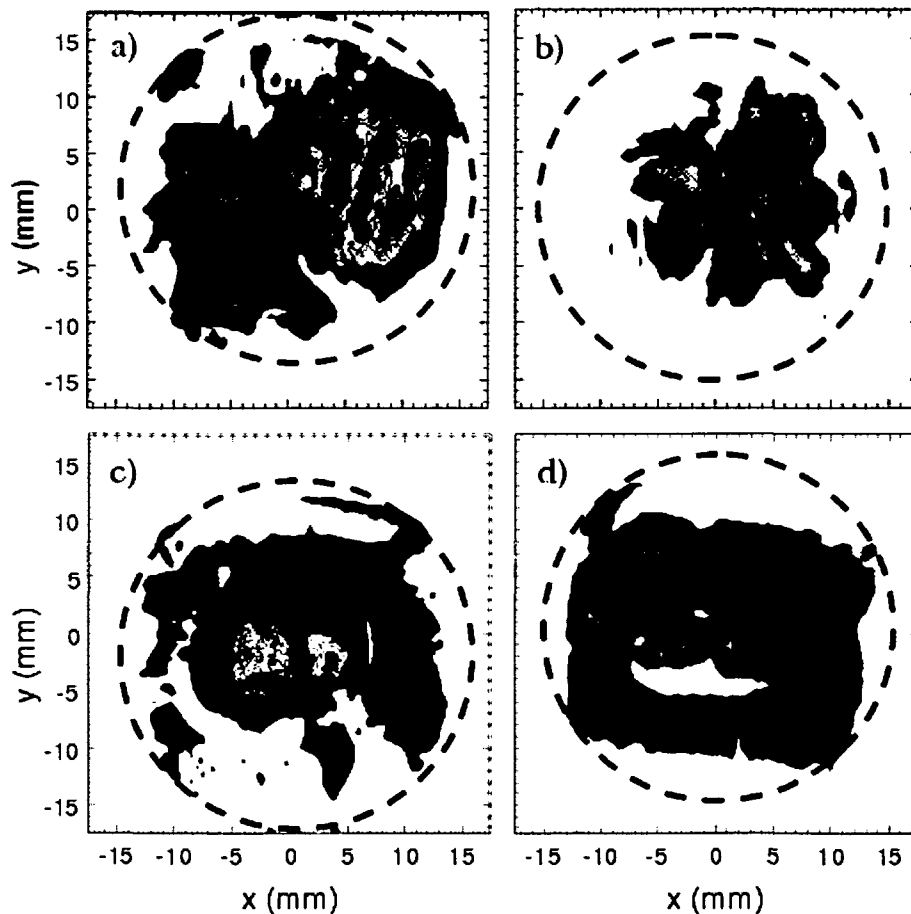
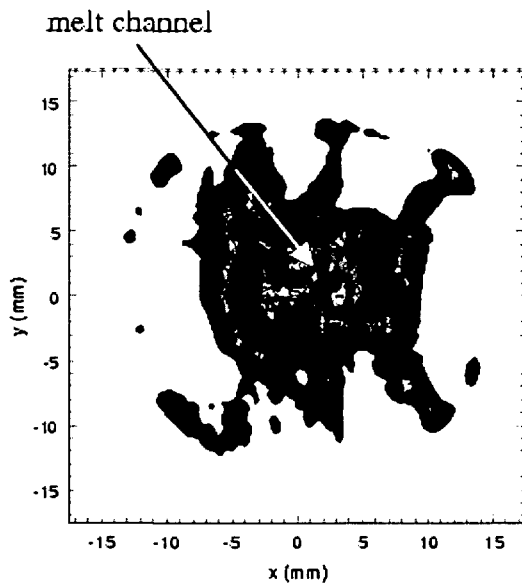


Fig. 101: Magnetoscans of samples a) *MS-1*, b) *MS-2*, c) *MS-3* and d) *MS-4*. The circles indicate the sample circumference.

Table 29: Parameters of magnetoscans shown in Fig. 101.

sample code	<i>MS-1</i>	<i>MS-2</i>	<i>MS-3</i>	<i>MS-4</i>
grid size	0.5 mm × 0.5 mm	0.5 mm × 0.5 mm	0.25 × 0.25 mm ²	0.5 mm × 0.5 mm
gap	0.2 mm	0.2 mm	0.2 mm	0.2 mm
temperature control	77.75	77.86 K	78.21 ± 0.31 K	77.55 ± 0.14 K
Hall probe	HHP VPO 48	HHP VPO 48	HHP VPO 48	HHP VPO 48
magnet	∅ = 6 mm, 80 mT	∅ = 6 mm, 80 mT	∅ = 6 mm, 80 mT	∅ = 6 mm, 80 mT

Upon changing the setup parameters of the magnetoscan (magnet size $\varnothing = 3$ mm, $\mu_0 H = 100$ mT), more details between the seed positions of sample *MS-3* and *MS-4* were found. The result for *MS-3* is shown in Fig. 102. The influence of a “melt channel”, which was found by optical microscopy, on the shielding properties can be observed. Although a depression in the trapped field was found between the seed positions, the magnetoscan provides in this case a better localization of the boundaries for the current flow. The position of the thin melt channel is accurately mapped.

Fig. 102: Magnetoscan of sample *MS-3*. The grid size of the scan was 0.25 mm × 0.25 mm.

6.4.2 Characterization of *R1*

Some microstructural details of sample *R1* were already discussed in chapter 2 *Microstructure*. A Hall scan of the sample surface after activation at $\mu_0 H = 1.4$ T (fc) clearly shows the boundaries between adjacent grains (Fig. 103). This is not surprising, since a thin crack was found at the grain boundary position. The maximal trapped field for the whole sample is 0.41 T, but the 10 individual grains have different maxima.

The following experiment on sample *R1* was motivated by the possibility, that the residual liquids present at the GB would be reduced with increasing vertical distance from the top side of the sample until a “clean” GB forms [67]. To examine this, a vertical assessment of the sample was performed by reducing its thickness step by step, in order to eventually find a more homogeneous trapped flux distribution, i.e. to less dramatic effects of the GBs. After each grinding step, a Hall scan and a magnetoscan were made. Moreover, the GBs were also investigated by optical microscopy and scanning electron microscopy where the sizes of the GB were found to decrease with increasing distance from the top. Fig. 104 shows the results for different sample thicknesses. With decreasing thickness, the homogeneity within the individual domains decreases, but the grain-to-grain-connectivity does not improve.

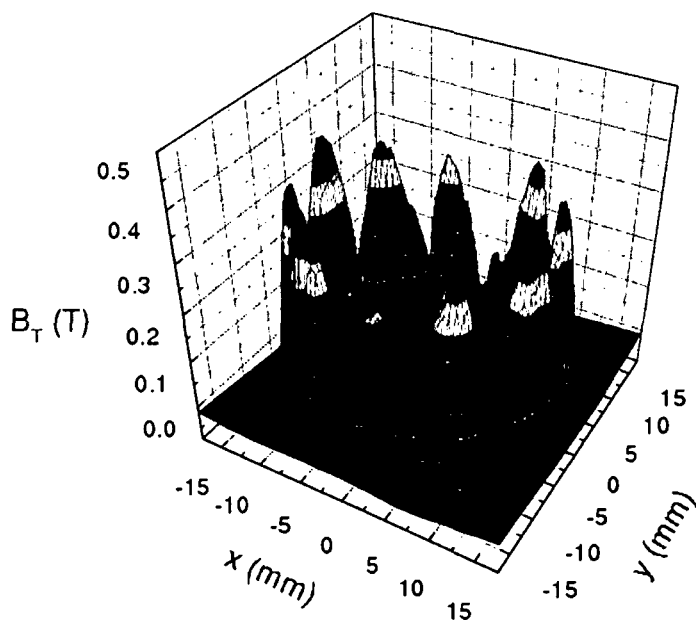


Fig. 103: 3D distribution of the trapped flux in sample *R1*. The boundaries between adjacent grains show deep suppressions of the trapped field.

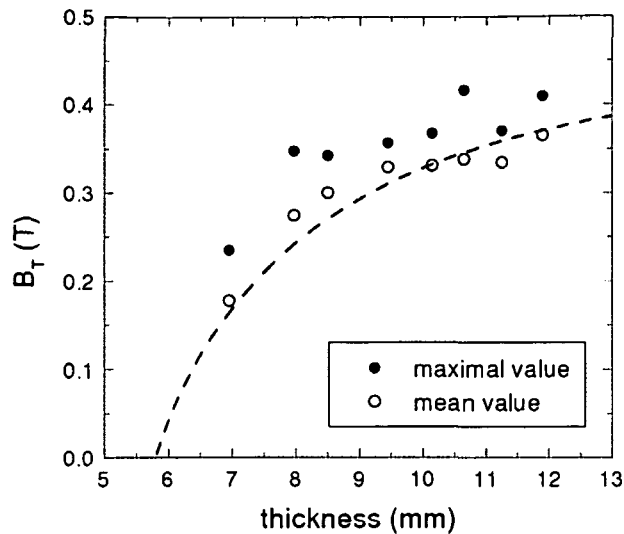


Fig. 105: Trapped fields as a function of thickness. The theoretical curve is based on a constant critical current density.

In Fig. 105, the arithmetic mean of the maximal trapped field values of each domain and the absolute maximum are drawn as a function of thickness. A theoretical fit shows that the assumption of a constant critical current density is not bad for the mean values [79-80]. Stronger deviations from the predicted curve are shown by the absolute values, which indicate qualitative differences between the individual single domains. After having removed about 5 mm from the original thickness of the sample (11.9 mm), the mean maximal trapped fields drop to zero, indicating that the superconducting region contributing to the trapped field is about 6 mm (if the contribution of the bottom part is neglected).

7 OUTLOOK

The results presented in this PhD thesis form the basis for new experiments, particularly when attempts to improve the resolution of the magnetoscan are successful.

It became very soon obvious that the main differences in the signal of the magnetoscan correspond to different growth sectors of the melt-grown bulk superconductor. But when we take a closer look at the signal and its spatial variation, many local maxima and local minima are detected. The important question will be: What is the origin of this variation in the signal? Fig. 106 presents the contour plot of a magnetoscan and the signal variation along its diameter marked by the dashed line. The grid size of the measurement was $0.2 \text{ mm} \times 0.2 \text{ mm}$. “Large” variations in the signal – 0.2 mV – are attributed to the growth sectors. “Small” variations in the signal below 0.05 mV are found too. A higher resolution of the scan will, of course, lead to more local features on the sample surface and would help to determine the origin of these “small” variations in the signal. A possible explanation is the *c*-macrocrack network, presented in chapter 2 *Microstructure*. This network of macrocracks is uniformly distributed over the sample surface. Since these small variations in the signal are also uniformly distributed over the sample surface, the local minima in the magnetoscan could actually map the *c*-macrocracks [83]. However, this has to be proved by a comparison of the spacing between the cracks ($\leq 100 \mu\text{m}$) and the oscillation of the magnetoscan signal ($\leq 1 \text{ mm}$).

Another task, based on an improvement of the spatial resolution of the magnetoscan technique, would be mapping the periodic structure (i.e. Y-123 matrix split by non-superconducting layers) of so called cyclic grown superconductors. There, the phases and Y-211 are pushed by the Y-123 matrix until, as proposed in [84], the concentration of the additi-

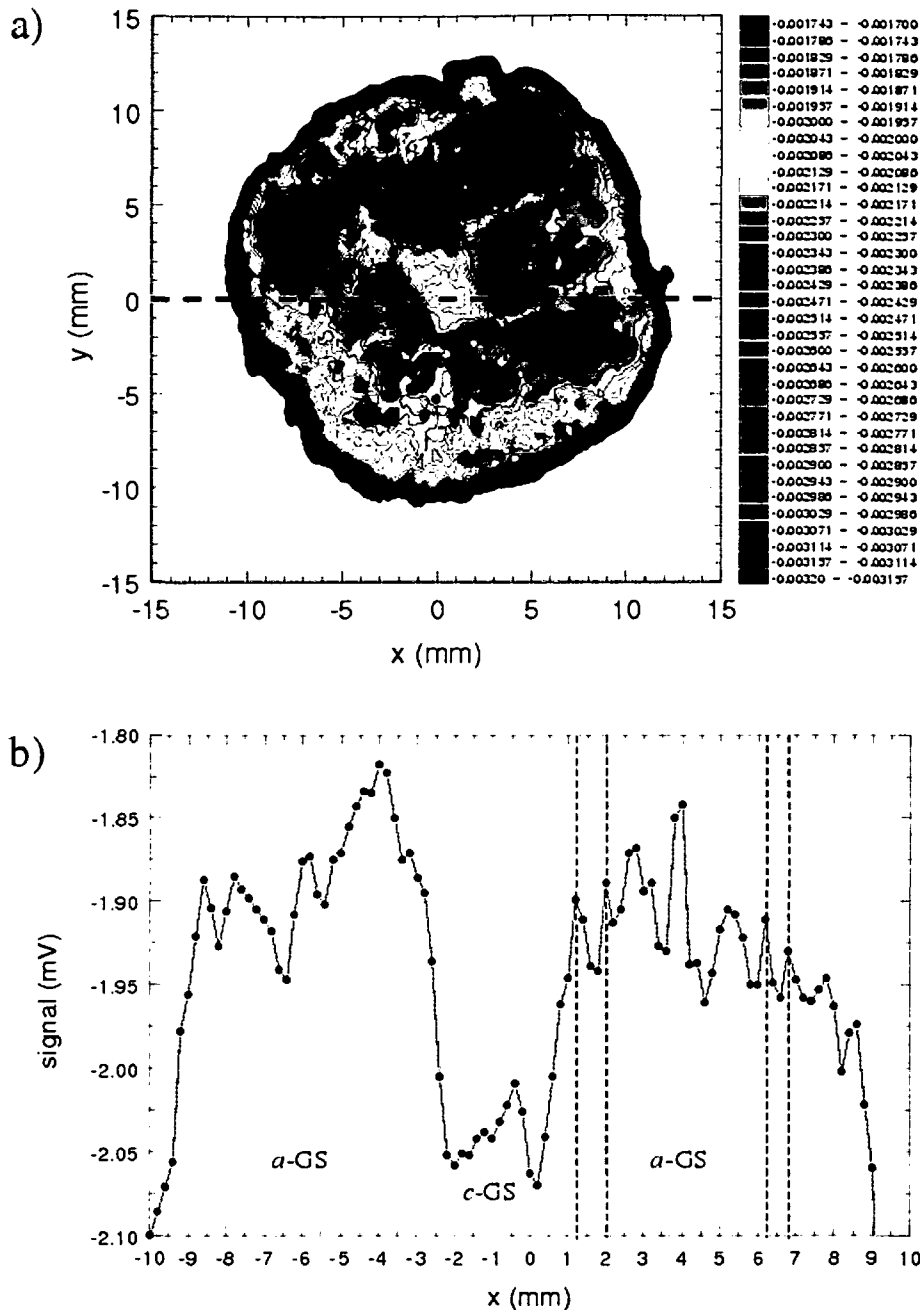


Fig. 106: a) Magnetoscan of sample *Li0at5* and b) signal of the Hall probe along the cross section.

Local variations in the signal show that separations between maxima smaller than 1 mm can be resolved.

ves exceeds the solubility limit of the melt. Then small layers with residual melt and phases containing the dopants, e.g. iridium, are formed. Subsequently, the Y-123 matrix starts to grow again from this small layer. Fig. 107a-c show scanning electron micrographs of an Ir-doped $\text{YBa}_2\text{Cu}_3\text{O}_{7.8}$. There, a zone with trapped Y-211 particles with a size of several hundred μm exists until the Y-123 matrix grows again Y-211 free. This structure, which is schematically sketched in Fig. 107d, is repeated several times. The spacing between the

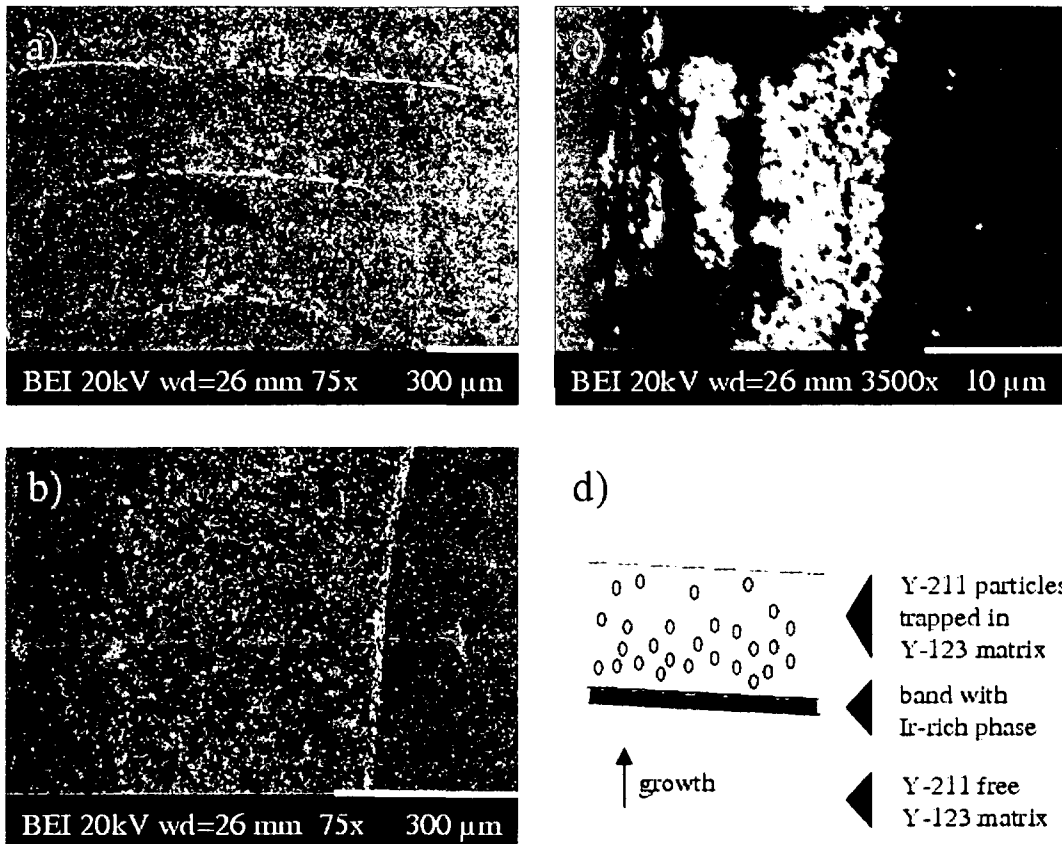


Fig. 107: Backscattering images of an Ir-doped $\text{YBa}_2\text{Cu}_3\text{O}_{7.8}$ sample. a) Periodic layers with an Ir containing phase. b) Zone with trapped Y-211 particles in the Y-123 matrix. c) Ir-rich band containing very small particles. d) Schematic illustration of the cyclic structure. The sample is published in [84].

Ir-rich layers is about 400 μm , the Ir-rich layers have an extension in the a - b plane of only 20 μm . The resolution of this periodic structure would be a great success for the magnetoscan technique and maybe help to clarify details of the formation of this kind of structure.

SUMMARY

In this work, two experimental techniques to investigate the homogeneity of superconducting bulk samples were introduced. These techniques are *i)* conventional Hall scans after zfc activation at different external fields below $2H^*$ and *ii)* a totally new technique, called magnetoscan. Both techniques show advantages for the investigation of growth induced inhomogeneities compared to a conventional Hall scan in the fully magnetized state of the bulk monolith. They provide a non destructive way for a spatial mapping of grain boundaries, subgrains and cracks. In addition, a vertical analysis of bulk monoliths was proposed, where both techniques were employed. Among the general results, experimental evidence for the weaker superconducting properties of the *c*-GS and the weak-link free *a-a*-GSBs was provided. These results were supported by additional microstructural investigations. Two challenges for a future improvement of the magnetoscan technique were proposed: the detection of a *c*-macrocrack pattern and the investigation of cyclic grown superconductors. The magnetoscan of an irradiated sample was also presented for the first time, but no conclusion would be drawn due to the lack of additional experimental data on various samples. Investigations of MSMG samples showed that the change in the crystallographic orientation of the seed crystals had drastic effects on the homogeneity of the trapped flux distribution and its maximum.

REFERENCES

- [1] C. P. Bean, *Phys. Rev. Lett.* 8 (1962) 250-253
- [2] C. P. Bean, *Rev. Mod. Phys.* (1964) 31-39
- [3] G. Fuchs, G. Krabbes, P. Schätzle, P. Stoye, T. Staiger, K.-H. Müller, *Physica C* 268 (1996) 115-120
- [4] S. Nariki, N. Sakai, M. Murakami, *Physica C* 357-360 (2001) 629-634
- [5] R. González Arrabal, M. Eisterer, H. W. Weber, G. Fuchs, P. Verges, G. Krabbes, *Appl. Phys. Lett.* 81 (2002) 868-870
- [6] M. Tomita, M. Murakami, *Nature* 42 (2003) 517-520
- [7] S. Jin, T. H. Tiefel, R. C. Sherwood, R. B. van Dover, M. E. Davis, G. W. Kammlott, R. A. Fastnacht, *Phys. Rev. B* 37 (1988) 7850
- [8] K. Salama, D. F. Lee, *Supercond. Sci. Technol.* 7 (1994) 177-193
- [9] R. González Arrabal, M. Eisterer, H. W. Weber, *J. Appl. Phys.* 93 (2003) 4734-4738
- [10] M. Eisterer, S. Haindl, T. Wojcik, H. W. Weber, *Supercond. Sci. Technol.* 16 (2003) 1282-1285
- [11] M. Zeisberger, T. Habisreuther, D. Litzkendorf, A. Surzhenko, W. Gawalek, *Supercond. Sci. Technol.* 18 (2005) S90-S94
- [12] T. Kono, N. Sakai, S. Nariki, I. Hirabayashi, N. Koshizuka, M. Murakami, to be published in *IEEE Trans. Appl. Supercond.*
- [13] S. Haindl, M. Eisterer, N. Hörhager, H. W. Weber, L. Shlyk, G. Krabbes, H. Walter, N. Hari Babu, D. A. Cardwell, contribution at the ISS 2004, to be published in *Physica C*
- [14] M. Bichler, private communication
- [15] M. Aleksa, P. Pongratz, O. Eibl, F. M. Sauerzopf, H. W. Weber, T. W. Li, P. H. Kes, *Physica C* 297 (1998) 171-175

- [16] C. D. Dewhurst, Wai Lo, Y. H. Shi, D. A. Cardwell, *Mat. Sci. Eng. B53* (1998) 169-173
- [17] I.-G. Chen, G. Jamn, J.-C. Hsu, *Mat. Sci. Eng. B53* (1998) 132-137
- [18] S. Takebayashi, M. Murakami, *Mat. Sci. Eng. B65* (1999) 17-25
- [19] S. Takebayashi, S. I. Yoo, M. Murakami, *Physica C* 383 (2003) 465-472
- [20] B. Latha, M. Yoshikawa, Y. Yanagi, T. Yamada, Y. Itoh, H. Ikuta, U. Mizutani, *Physica C* 392-396 (2003) 521-525
- [21] A. B. Surzhenko, S. Schauroth, D. Litzkendorf, M. Zeisberger, T. Habisreuther, W. Gawalek, *cond-mat/0104578 v3* 15 May 2001 (not published in this form)
- [22] A. B. Surzhenko, S. Schauroth, D. Litzkendorf, M. Zeisberger, T. Habisreuther, W. Gawalek, *Physica C* 372-376 (2002) 1212-1215
- [23] G. Krabbes, P. Schätzle, W. Bieger, U. Wiesner, G. Stöver, M. Wu, T. Strasse, A. Köhler, D. Litzkendorf, K. Fischer, P. Görnert, *Physica C* 244 (1995) 145-152
- [24] M. P. Delamare, H. Walter, B. Bringmann, A. Leenders, H. C. Freyhardt, *Physica C* 323 (1999) 107-114
- [25] M. Murakami, *Supercond. Sci. Technol.* 5 (1992) 185-203
- [26] N. Ogawa, I. Hirabayashi, S. Tanaka, *Physica C* 177 (1991) 101
- [27] N. Ogawa, M. Yoshida, I. Hirabayashi, S. Tanaka, *Supercond. Sci. Technol.* 5 (1992) S89.
- [28] M. Morita, M. Tanaka, S. Takebayashi, K. Kimura, K. Miyamoto, K. Sawano, *Jap. J. Appl. Phys.* 30 (1991) L813
- [29] S. Gauss, S. Elschner, H. Bestgen, *Cryogenics* 32 (1992) 965
- [30] C. Varanasi, P. J. McGinn, *Physica C* 207 (1993) 79
- [31] Y. Shiohara, A. Endo, *Mat. Sci. Eng. R19* (1997) 1
- [32] M. P. Delamare, M. Hervieu, J. Wang, J. Provost, I. Monot, K. Verbist, G. Van Tendeloo, *Physica C* 262 (1996) 220-226
- [33] L. S. Uspenskaya, I. G. Naumenko, G. A. Emelchenko, Yu. B. Boguslavskii, S. A. Zver'kov, E. B. Yakimov, D. Litzkendorf, W. Gawalek, A. D. Caplin, *Physica C* 390 (2003) 127-133
- [34] S. Pinol, F. Sandiumenge, B. Martinez, V. Gomis, J. Fontcuberta, X. Obradors, E. Snoeck, C. Roucau, *Appl. Phys. Lett.* 65 (1994) 1448

- [35] S. K. Chen, L. Zhou, K. G. Wang, X. Z. Wu, P. X. Zhang, Y. Feng, *Physica C* 366 (2002) 190-194
- [36] J. M. S. Skakle, *Mat. Sci. Eng. R23* (1998) 1-40
- [37] L. Shlyk, G. Krabbes, G. Fuchs, K. Nenkov, B. Schüpp, *Journal of Applied Physics* 96 (2004) 3371-3378
- [38] F. Maury, M. Nicolas-Francillon, F. Bourée, R. Ollitrault-Fichet, M. Nanot, *Physica C* 333 (2000) 121-132
- [39] J. Bobroff, W. A. MacFarlane, H. Alloul, P. Mendels, N. Blanchard, G. Collin, J.-F. Marucco, *Phys. Rev. Lett.* 83 (1999) 4381-4384
- [40] L. Shlyk, G. Krabbes, G. Fuchs, K. Nenkov, P. Verges, *Physica C* 392-396 (2003) 540-544
- [41] J. D. Jorgensen, M. A. Beno, D. G. Hinks, L. Soderholm, K. J. Volin, C. U. Segre, K. Zhang, M. S. Kleefisch, *Phys. Rev. B.* 36 (1987) 3608-3616
- [42] N. R. Werthamer, E. Helfand, P. C. Hohenberg, *Phys. Rev.* 147 (1966) 295
- [43] A. Koblishka-Veneva, M. R. Koblishka, K. Ogasawara, M. Murakami, *Cryst. Eng.* 5 (2002) 265-272
- [44] P. Diko, *Supercond. Sci. Technol.* 17 (2004) R45-R58
- [45] R. Cloots, T. Koutzarova, J.-P. Mathieu, M. Ausloos, *Supercond. Sci. Technol.* 18 (2005) R9-R23
- [46] PCPDFWIN v. 2.2, JCPDS (2001) 81-0801, 89-1359
- [47] D. Turnbull, J. C. Fisher, *J. Chem. Phys.* 17 (1949) 71
- [48] R. J. Cava, B. Batlogg, C. H. Chen, E. A. Rietman, S. M. Zahurak, D. Werder, *Phys. Rev. B* 36 (1987) 5719
- [49] P. Diko, W. Gawalek, T. Habisreuther, T. Klupsch, P. Görnert, *Phys. Rev. B* 52 (1995) 13658-13664
- [50] P. Diko, W. Gawalek, T. Habisreuther, T. Klupsch, P. Görnert, *Journal of Microscopy* 184 (1996) 46-57
- [51] P. Diko, *Supercond. Sci. Technol.* 13 (2000) 1202-1213
- [52] P. Diko, S. Takebayashi, M. Murakami, *Physica C* 297 (1998) 216-222
- [53] S. Kracunovska, P. Diko, D. Litzkendorf, T. Habisreuther, J. Bierlich, W. Gawalek, *Supercond. Sci. Technol.* 18 (2005) S142-S148
- [54] C.-J. Kim, H.-J. Kim, J.-H. Joo, G.-W. Hong, *Physica C* 354 (2001) 384-387

- [55] C.-J. Kim, G.-W. Hong, H.-J. Oh, *Physica C* 357-360 (2001) 635-641
- [56] Ch. Jooss, B. Bringmann, M. P. Delamare, H. Walter, A. Leenders, H. C. Freyhardt, *Supercond. Sci. Technol.* 14 (2001) 260-275
- [57] K. Furusawa, N. Chikumoto, K. Ogasawara, T. Nagatomo, M. Murakami, *Physica C* 378-381 (2002) 255-259
- [58] C.-J. Kim, H.-J. Kim, Y. A. Lee, G.-W. Hong, J.-H. Joo, S.-C. Han, Y.-H. Han, T.-H. Sung, S.-J. Kim, *Physica C* 338 (2000) 205-212
- [59] L. Shlyk, G. Krabbes, G. Fuchs, *Physica C* 390 (2003) 325-329
- [60] D. Litzkendorf, T. Habisreuther, M. Wu, T. Strasser, M. Zeisberger, W. Gawalek, M. Helbig, P. Görnert, *Mat. Sci. Eng. B53* (1998) 75-78
- [61] private communication, D. Litzkendorf (2004)
- [62] courtesy of R. Müller
- [63] private communication, H. Walter, Nexans SuperConductors GmbH (2003)
- [64] private communication, M. P. Delamare, R. González Arrabal (2001)
- [65] R. González Arrabal, PhD thesis, TU Vienna (2002)
- [66] H. Walter, Ch. Jooss, F. Sandiumenge, B. Bringmann, M.-P. Delamare, A. Leenders, H. C. Freyhardt, *Europhys. Lett.* 55 (2001) 100-104
- [67] S. Haindl, M. Eisterer, H. W. Weber, N. H. Babu, D. A. Cardwell, to be published in *IEEE Transactions on Applied Superconductivity*
- [68] private communication, N. Hari Babu (2005)
- [69] S. Ilescu, X. Granados, E. Bartolomé, S. Sena, A. E. Carrillo, T. Puig, X. Obradors, J. E. Evetts, *Supercond. Sci. Technol.* 17 (2004) 182-185
- [70] B. R. Lehndorff, *High-T_C Superconductors for Magnet and Energy Technology*, Springer Tracts in Modern Physics Vol. 171 (2001)
- [71] R. Boll, K. J. Overshott W. Göpel (eds.) *Sensors. Vol. 5, Magnetic Sensors*, Verlag Chemie (1989)
- [72] Lubo Kopera, www.arepoc.sk
- [73] private communication, M. Müller (2004)
- [74] F. Baumgärtner, *Kerntechnik* 3.Jg, H.8 (1961) 356
- [75] S. J. Manton, C. Beduz, Y. Yang, K. Deligiannis, P. A. J. deGroot, *Mat. Sci. Eng. B53* (1998) 182-184
- [76] H. W. Weber, H. Böck, E. Unfried, L. R. Greenwood, *J. Nuc. Mat.* 137 (1986) 236-240

- [77] S. Haindl, M. Eisterer, H. W. Weber, L. Shlyk, G. Krabbes, *Supercond. Sci. Technol.* 18 (2005) S164-S167
- [78] M. Eisterer, S. Haindl, T. Wojcik, H. W. Weber, in: G. P. Pepe, R. Cristiano, G. Masullo (Eds.), *Proc. 6th EUCAS*, 181 (2005) 1386
- [79] H. Fukai, M. Tomita, M. Murakami, T. Nagamoto, *Supercond. Sci. Technol.* 15 (2002) 1054-1057
- [80] I.-G. Chen, J. Liu, R. Weinstein, K. Lau, *J. Appl. Phys.* 72 (1992) 1013-1020
- [81] M. Müller, TU Vienna (2003 – 2004)
- [82] private communication, M. Bichler (2004)
- [83] private communication, P. Diko (2004)
- [84] L. Shlyk, B. Schüpp, G. Krabbes, K. Nenkov, G. Fuchs, *Physica C* 406 (2004) 107-114

LIST OF PUBLICATIONS

Publications

1

M. Eisterer, S. Haindl, T. Wojcik, H. W. Weber:

“Magnetoscan’: a modified Hall probe scanning technique for the detection of inhomogeneities in bulk high temperature superconductors”

Supercond. Sci. Technol. 16 No 11 (2003) 1282-1285

2

M. Eisterer, S. Haindl, R. González Arrabal, T. Wojcik, H.W. Weber:

“Current distribution in nearly homogeneous melt textured monoliths”

Physica C, 408-410 (2004) 634-635

3

M. Eisterer, S. Haindl, T. Wojcik, H. W. Weber

“Remnant current distribution in a melt textured monolith: Assessment of variations along the thickness”

in: P. Pepe, R. Cristiano, G. Masullo (Eds.), Proc. 6th EUCAS, 181 (2005) 1386

4

S. Haindl, M. Eisterer, H.W. Weber

“Magnetic flux penetration into melt textured superconductors”

Supercond. Sci. Technol. 18 (2005) S164-S167

5

S. Haindl, M. Eisterer, H. W. Weber, N. Hari Babu, D. A. Cardwell

“Grain boundaries in Multi-Seeded Melt-Grown Superconductors”

IEEE Transactions on Applied Superconductivity (in press)

6

S. Haindl, M. Eisterer, R. Müller, R. Prokopec, H. W. Weber, M. Müller, H. Kirchmayr, T. Takeuchi, L. Bargioni

„Neutron irradiation effects on A15 multifilamentary wires”

IEEE Transactions on Applied Superconductivity (in press)

7

S. Haindl, M. Eisterer, N. Hörhager, H. W. Weber, L. Shlyk, G. Krabbes, H. Walter, N. Hari Babu, D. A. Cardwell

“Novel Methods to Characterize Bulk RE-BCO Superconductors”

Physica C (in press)

8

N. Hari Babu, Y.-H. Shi, K. Iida, D. A. Cardwell, S. Haindl, M. Eisterer and H. W. Weber

“Processing of large, single grain $YBa_2Cu_3O_{7-\delta}/Y_2BaCuO_5/YBa_2Cu,MO_y$ bulk composites”

Physica C (in press)

Conference Contributions, Meetings and Seminars:

9

Poster contribution M. Eisterer, at ISS 2003

M. Eisterer, S. Haindl, H. W. Weber, M. Foitl, K. Hense, H.R. Kirchmayr, T. Takeuchi

“Suitability of Nb_3Al and Nb_3Sn Wires for Fusion Reactors”

10

S. Haindl, M. Eisterer, H.W. Weber

“Magnetic flux penetration into melt textured superconductors”

Poster at PASREG, Jena 2003

11

Seminar Talk, Cambridge 2003

“Radial and axial homogeneity of bulk melt-processed YBCO superconductors”

12

Hot Topic, EFFORT Meeting, Cambridge 2003

“Homogeneity of Li-Doped YBCO single domain bulk superconductors”

13

Seminar Talk, ATI, Vienna 2003

“Radial and axial homogeneity of bulk melt-processed YBCO superconductors”

14

Seminar Talk, ATI, Vienna 2004

“Characterization of multi-seeded bulk superconductors”

15

Hot Topic, EFFORT Meeting, High Tatras 2004

“Vertical Analysis of a melt-textured Li-doped YBCO”

16

Poster at ASC, Jacksonville 2004

S. Haindl, M. Eisterer, H. W. Weber, N. Hari Babu, D. A. Cardwell*“Grain boundaries in Multi-Seeded Melt-Grown Superconductors”*

17

Poster at ASC, Jacksonville 2004

**S. Haindl, M. Eisterer, R. Müller, R. Prokopec, H. W. Weber, M. Müller, H. Kirchmayr,
T. Takeuchi, L. Bargioni***„Neutron irradiation effects on Al5 multifilamentary wires”*

15

Seminar Talk, ATI, Vienna 2005

“Investigation of the homogeneity of melt-textured bulk superconductors”

CURRICULUM VITAE

Persönliche Daten

Name: Silvia Haindl
Geburtsdatum: 15.1.1977
Geburtsort: Wien
Staatsbürgerschaft: Österreich
Adresse: 1030 Wien, Hofmannsthalgasse 10/5/3

Studienlaufbahn und Ausbildung

September 1983 – Juni 1986: Volksschule in Wien 3, Kleistgasse
September 1987 – Juni 1995: Gymnasium in Wien 3, GRG III, Hagenmüllergasse
Juni 1995: Matura mit ausgezeichnetem Erfolg
Oktober 1995: Beginn des Studiums der Technischen Physik an der TU Wien
Oktober 1997: Beginn des Studiums Philosophie / Geschichte an der Universität Wien
Juli 2000: Teilnahme an der ASA – Summerschool in Alpbach
Oktober 2001: Beginn des Studiums der Technischen Mathematik (Stzw. Mathematik in den Naturwissenschaften) an der TU Wien
Oktober 2002: Diplomprüfung und Abschluß des Studiums der Technischen Physik an der TU Wien

Diplomarbeit: „*Kritische Ströme in Nb₃Sn und Nb₃Al Supraleitern*“ ausgeführt am Atominstitut der Österreichischen Universitäten unter Anleitung von Herrn Univ. Prof. Dr. Dr. h.c. H. W. Weber
Beginn des Doktoratsstudiums der Technischen Wissenschaften (Dissertationsgebiet Technische Physik) an der TU Wien

Oktober 2002 - Juni 2003:

Studienassistentin am Institut für Theoretische Physik an der TU Wien

Oktober 2002 - Februar 2005:

Anstellung am Atominstitut der Österreichischen Universitäten / TU Wien als Forschungsassistent, Doktoratsstudium der Technischen Wissenschaften (Dissertationsgebiet Technische Physik) an der TU Wien

Sprachkenntnisse:

Deutsch, Englisch, Französisch (Maturaniveau), Spanisch